Strut Fuel Injector Penetration and Mixing Enhancement for a Dual-mode Scramjet

---

A Dissertation

Presented to
the faculty of the School of Engineering and Applied Science
University of Virginia

---

in partial fulfillment
of the requirements for the degree

Doctor of Philosophy

by

Maxwell J. DePiro

December

2015

APPROVAL SHEET

The dissertation
is submitted in partial fulfillment of the requirements
for the degree of
Doctor of Philosophy
in
Mechanical and Aerospace Engineering

Maxwell J. DePiro, Author

The dissertation has been read and approved by the examining committee:

Christopher Goyne, Dissertation Advisor

James McDaniel, Committee Chair

Harsha Chelliah, Committee Member

Mool Gupta, Committee Member

Richard Gaffney, Committee Member

David Witte, Committee Member

Accepted for the school of Engineering and Applied Science:

Dean, School of Engineering and Applied Science

December
2015

UNIVERSITY OF VIRGINIA

Abstract

Department of Mechanical and Aerospace Engineering

Doctor of Philosophy

Strut Fuel Injector Penetration and Mixing Enhancement for a Dual-mode Scramjet

by Maxwell J. DePiro

To meet the needs of future high-speed, air-breathing aerospace applications, large-scale dual-mode scramjet engines are being developed. These engines tend to have large combustor cross sections where flush wall injectors are not adequate for delivering the fuel to the core flow. In these applications, struts are typically used to span the gap, however, these intrusive devices add drag to the internal flow, and have high thermal loads to manage. In this study a tip injector was designed to penetrate fuel above the strut into the core flow of the combustor in order to limit the exposure of mechanical surfaces to the flow. Since the flowfield surrounding the tip injector is vastly different from that of a flush wall injector, this study provides a detailed investigation into those physics with both computational and experimental results. Background Oriented Schlieren (BOS) and in-stream gas sampling was used to visualize and measure the flowfield and mixing. Both time-averaged and instantaneous images were reported, and the gas sampling data was correlated to the BOS image data showing that a calibration of the BOS was possible in order to extract quantifiable information about the mixing. Comparing the results

of the strut tip injector to a flush wall injector showed that the strut has a reduction in mixing, and a benefit in the jet penetration.

The flowfield of a dual-mode scramjet fuel injector is affected by the combustion process, which increases the static pressure. The experiments conducted for this study, simulated the combustor pressure by backpressuring the flowpath. The mixing results show differences in the behavior between the strut and flush wall injector due to boundary layer differences. The jet penetration from the strut is entirely dependent on the jet-to-air dynamic pressure ratio, Q because it is far from the wall relative to the wall boundary layer thickness.

The specific case of a backpressure induced shock interacting with the injector bow shock is also considered. Instantaneous BOS images of the flush wall injector under these conditions show an increase in turbulence in the mixing jet, implying that the shock enhances the mixing rate. The results also show that the shock has no impact on the jet penetration for the strut injector.

This study provides the first detailed investigation into a strut tip injector, and the first examination of a strut injector in a backpressured flowpath. The results indicate that for a strut injector the jet penetration can be accurately predicted over the range of dual-mode scramjet flight conditions.

Acknowledgements

There are many individuals who deserve recognition for the making of this dissertation. I want to thank Professor Christopher Goyne for his academic and technical advisement throughout my graduate career. He and I have worked together for nearly eight years and I am thankful to be able to call him my colleague and friend. I want to thank Mr. David Witte for his technical guidance and sustained encouragement. His involvement with this project was one of the most positive influences I could have had. I would like to thank Shelly Ferlemann for sanctioning my project, and Dr. Richard Gaffney, who continued the branch support of my project after taking over as branch head. I would also like to thank him for helping me re-evaluate my research approach when I felt like things were falling apart. I have to thank Dr. Brett Bathel who is the owner and expert of the BOS system. It was his idea to apply the BOS system to these experiments. His companionship and work ethic was inspiring and drove me to work harder. I want to thank the technician support, without whom no air would ever flow. The expertise of Stephen (Fred) Mason and Barry Lawhorne in designing, constructing, coordinating, and operating the facility and the experimental systems was invaluable. I want to thank Mr. Ken Rock as well, he is responsible for giving me the opportunity to pursue my PhD at NASA. I would like to thank all of my colleagues at the Hypersonic Airbreathing Propulsion Branch at NASA LaRC, and specifically Diego Capriotti, Dr. Tomasz Drozda, and Dr. Aaron Auslender. The opportunity to work with you all has been an honor.

I want to thank my best friend and life companion, Louise Knudson, without whom this dissertation could never have been written. She has supported me in ways I could not have imagined possible, she is simply the best partner anyone could ask for. Her

fearless grasp on life and the pursuit of happiness inspires me to see past the immediate obstacles and focus on what I want or need to fulfill. Louise, I look forward to a beautiful life together. I want to thank my parents, Donald and Beth, and my family for their support over the years. The values they instilled in me and the personality they cultivated early in my life has made me who I am. Lastly, I also want to thank my friends and colleagues, specifically Jesse Quinlan, for always giving me an ear to talk to and advice when I needed it.

Contents

List of Figures

List of Tables

Symbols

P	pressure	psi
T	temperature	Kelvin
γ	ratio of specific heats	
ρ	density	$\frac{kg}{m^3}$
χ	mole fraction	
α	mass fraction	
Da	BOS signal	pixel displacement
U	velocity	m/s
M	Mach number	
M_{ave}	mass averaged Mach number	
M_c	convective Mach number	
Q	jet-to-freestream dynamic pressure ratio	
ϕ	equivalence ratio	
f	fuel-air ratio by mass	
$\dot{m}$	mass flow	kg/s
f^o	fuel-air ratio by mole	
η_m	mixing efficiency	
η_o	overall mixing efficiency	
MW	molecular weight	$\frac{kg}{mole}$
h_{Md}	height of the jet Mach disk	inches
D	injector port diameter	inches
Y_p	helium penetration to upper boundary of jet	inches
X	axial distance	inches
Y	distance normal to the injector wall	inches
Z	distance normal to X and Y	inches
Re	Reynolds number	
s	shock-train length	
P_c/P_i	ratio of combustor pressure to inlet pressure	
W	work	Joules
gap	distance between injectors	length
L	length of interest in the combustor	length
μ	uncertainty	
e	error	
R	gas constant	$\frac{kJ}{kgK}$
δ	boundary layer thickness	inches
Δr	displacement vector	
t	time	seconds
C	normalization correction factor	
$S\#$	run number for strut injector	

$R\#$	run number for flush wall injector	
D_c	combustor diameter	
h	heat transfer coefficient	$\frac{J}{m^2K}$
h_{strut}	height of the strut	length
E	voltage signal	
A_w	hotwire surface area	
R_w	electrical resistance of the hotwire	
Nu	Nussult number	
mf	helium mole fraction of the calibration	
$\dot{q}$	volumetric flow	m^3/s
S	sensitivity matrix	
E	uncertainty vector	
t_{stat}	sample distribution statistic	
FWI	flush wall injector	

Subscripts:

st	stoichiometric condition
c	convective property within mixing layer
ref	atmospheric (reference) pressure
he	helium
air	air
t	total condition
1	near measurement plane
i	flow condition around injector
∞	flow condition at the nozzle exit
ω	boundary layer momentum thickness
pit	Pitot pressure
j	helium jet
nom	nominal condition
max	maximum value
h_2	hydrogen gas
CTA	constant temperature anemometer
m	mass
$corr$	corrected value
mix	gas mixture value
cal	calibration

Superscripts:

1	near measurement plane
2	far measurement plane

This dissertation is dedicated to the idea that as people of science we must give credence to maintaining mental health.

Chapter 1

Introduction and Historical Background

To expand the utility of aerospace vehicles into the hypersonic regime, propulsion systems with greater efficiency must be developed. One such engine that shows particular promise is the scramjet. This air-breathing engine allows for significant gains in performance at Mach numbers from 5 to 20. Scramjets are being developed with the potential for applications to a) carry payloads to orbit at lower cost and with greater reliability, b) carry people and goods around the planet more quickly, and c) carry military payloads on tactical long-range cruise missiles. Current aerospace propulsion engines each have their limitations; turbojets and turbofans are restricted to low supersonic speeds, and rockets are inefficient. Therefore, in order to explore new aerospace frontiers, research and development of scramjet engines capable of air-breathing hypersonic flight is essential. As part of the Hyper-X project, the X-43 flight vehicle, shown in fig. 1.1, demonstrated the world's first scramjet-powered flight, and still holds the speed record for an air-breathing

FIGURE 1.1: *An artist's rendering of the X-43 hypersonic flight vehicle. [23]*

engine at Mach 9.68. The Hyper-X project proved that scramjet-powered vehicles can meet the challenges of next generation aerospace systems. [73]

Air-breathing jet engines use the ambient air as the major component of the propellant, and consume the oxygen present in the air with fuel to heat the air. There are three basic operating processes in an air-breathing engine: compression, heat addition, and expansion. When flying at hypersonic speeds the inlet air has tremendous kinetic energy; Ramjets (subsonic combustion) and scramjets (supersonic combustion) are both air-breathing engine concepts which take advantage of this kinetic energy to compress the air aerodynamically by the design of the inlet geometry. Though both ramjets and scramjets operate similarly, each is most efficient in the respective ranges: $3 < M_{ramjet} < 7$ and $5 < M_{scramjet} < 20$. Unfortunately, solely using the vehicle kinetic energy and geometry to compress the engine airflow means that startup while the vehicle is stationary is not possible, as opposed to gas turbine engines which have spinning compressor fan blades to pull air into the inlet and compress the air without the vehicle moving. Figure 1.2 shows the relationship between engine performance, quantified by

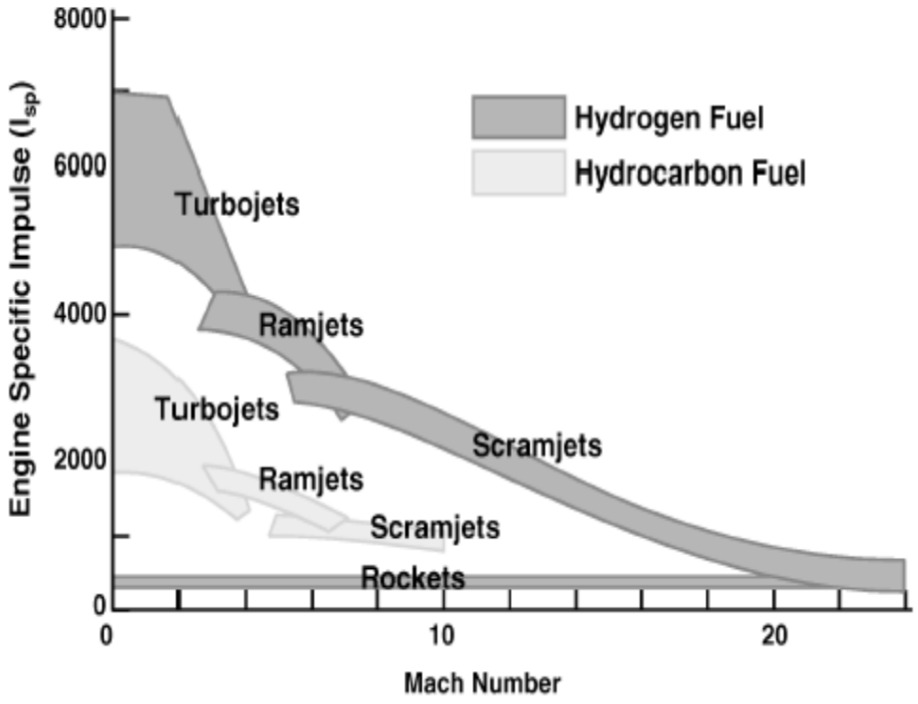

FIGURE 1.2: *Flight windows for various aerospace propulsion engines. [54]*

specific impulse, and Mach number. The overlapping ramjet and scramjet region does not cover a wide range of Mach numbers, only from about 5 to 7.

A Dual-Mode ScramJet (DMSJ) allows a single engine geometry to extend its region of operation from the ramjet range of Mach numbers through the scramjet range. In theory, a DMSJ could accelerate from Mach 3 to 20, which makes the engine a particularly attractive technology. This large range in flight speed means that the airflow entering the combustor will have a resultant change in flow from subsonic to supersonic. Consequently the flow physics of the fuel injection, mixing, and combustion will change greatly. These engines must be able to reliably accelerate and maneuver, causing these inflow conditions to change throughout the vehicle mission. Understanding the physics of DMSJ combustion is the key to achieving this capability.

The components of a DMSJ engine are; the forebody, inlet, isolator, combustor, and nozzle. See fig. 1.3 for a layout of these components. The dynamic pressure of the

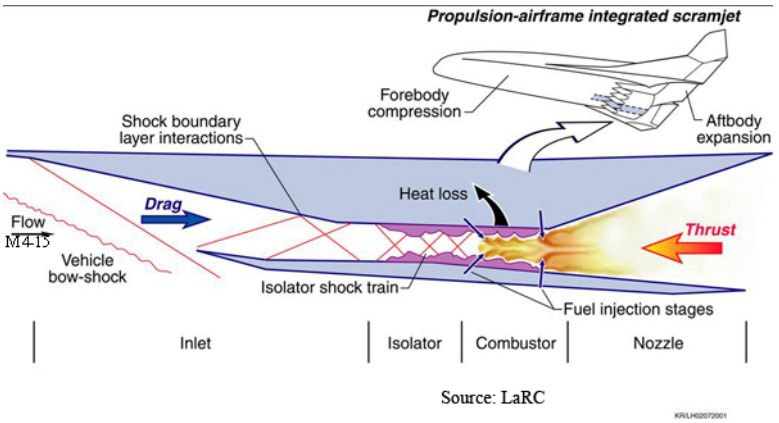

FIGURE 1.3: *The centerline cutview of a generalized scramjet engine. [24]*

free-stream air flow, incident on the vehicle, is converted to static pressure through the compression process along the forebody and inlet. The inlet captures the engine flow and leads to the isolator, which is a section of duct that acts to buffer the inlet from the combustor pressure rise; this completes the compression process. The entrance to the combustor, which is also the exit of the isolator, is where the fuel is injected and the mixing process is initiated. The fuel then mixes and burns through the combustor section increasing the total temperature and static pressure of the flow. For a dual-mode scramjet, the air flow upstream in the isolator is slow enough that it is affected by the combustor pressure rise. Consequently, a shock train forms in the isolator. If these shocks pass upstream of the inlet, the mass flow of air captured by the inlet drops. This occurrence is called unstart, and, depending on the severity, can adversely affect the engine operation.

This dissertation will focus on the fuel injection and mixing process from a strut injector. This injector has been designed to deliver fuel into the center of the combustor from the tip to minimize the impact of the strut on the engine airflow. Strut fuel injectors will be discussed in section 1.5.4. This prospect presents new design challenges as well as the unknown behavior of the injected fuel from the strut tip. In order to understand

this type of injector, an investigation of the physics of the problem was performed. The next sections will discuss the problems that will be explored by this research; the objectives and the contributions of this research that solve these problems will be presented. Lastly, a fundamental background for fuel injection and mixing experimentation will be discussed to set up the discussion in the following chapters.

1.1 Problem Statement

Question 1: Can the performance of a strut be improved by injecting fuel from the tip of the strut?

To meet the challenges for hypersonic vehicle applications, larger scale scramjet engines are being developed. The problem is that as the engine scale increases, so does the distance that the fuel injectors must span to deliver fuel to the center, or core flow, of the combustor. This must be done with minimal drag on the engine airflow and minimal thermal loads to the mechanical parts. It has been suggested that injection from the tip of the strut could reduce the necessary height of the strut, thereby reducing drag and thermal loads. The background research on strut injectors for scramjet engines are discussed in section 1.5.4. The overall conclusions from the open literature on tip injection is that it did not appreciably penetrate above the strut. Therefore, an investigation into the physics of how a tip injector interacts with the flowfield is needed.

Question 2: How do the mixing characteristics for the strut tip injector compare to the flush wall injector?

Injecting fuel directly into the core flow from the strut is very different than injecting from the wall. There are fundamental flow physics that have been proven to affect

jet penetration, such as boundary layer thickness and bow shock interaction with the jet. These physics will be vastly different between these two injectors. In addition, the three-dimensionality of the flow is much different for a strut tip injector than for a wall injector. These physics have been well characterized for a wall injector by Schetz and Billig and other investigators. [13, 48, 76, 93] However, an investigation into these physics for a strut injector with tip injection is needed to meet future challenges.

Question 3: How does the change in crossflow conditions from subsonic to supersonic affect the mixing characteristics for a strut injector?

Combustion physics in a DMSJ causes the flow properties entering the combustor to critically change over the range of the defined flight conditions. The physics of the pre-combustion flow will be explained further in section 2.1. Of the affected flow properties, the Mach number, Reynolds number, and static pressure are significant to injection and mixing. Flow structures change as well, such as shock waves, boundary layer thickness, and turbulent eddies. Therefore, examining the injection and mixing in unperturbed supersonic flow does not completely describe the behavior of a fuel injector for a flight application. Furthermore, the impact on the mixing due to changes in these flow conditions and structures is dependent on the type of injector and its design.

1.2 Objectives

The goal of this dissertation is to understand the fundamental physics associated with the fuel-air mixing of a strut with fuel injection from the tip, in a simulated dual-mode scramjet environment. Within the framework established by the above research questions, a set of objectives was developed:

1. Examine the flow physics of strut fuel injection
2. Identify flow mechanisms that impact the fuel-air mixing
3. Quantify the enhancement to the fuel penetration from the strut injector
4. Evaluate the mixing when the 1-D averaged combustor flow transitions between supersonic and subsonic flow

1.3 Contributions

The physics of fuel-air mixing for a strut with tip injection are analyzed using the mixing characteristics; jet penetration, mixing efficiency, and total pressure recovery. These metrics of the mixing are characterized for the mass averaged Mach number, dynamic pressure ratio, boundary layer thickness, and shock wave interactions. A new efficiency metric was introduced called the Fuel Specific Mixing Efficiency (FSME), which gives a measure of the mixing versus drag for the amount of fuel injected. This study establishes the first detailed data set into the flowfield surrounding a strut tip injector, using a computational and experimental investigation. The interactions of the flow with the tip jet, due to the presence of the strut and lack of wall effects, has major implications on the behavior of the tip jet when compared to a jet issuing from the wall.

These results show a significant enhancement of the fuel penetration for a strut tip injector. This is important because it shows that a strut with tip injection can achieve much improved fuel delivery to the center of the combustor. These results are unique because the strut delivers fuel to the tip injector port with a high total pressure, and it is thin in comparison to the injector port diameter. A key enabler of the strut design was 3-D printing technology, which made it practical to manufacture.

This is the first data set exploring the mixing of a strut injector, under simulated dual-mode scramjet conditions, and reported in the open literature. These experiments cover a combustor flow range from subsonic to Mach 2, representing the range in conditions that a combustor would encounter from ignition through acceleration to scramjet mode operation. The results showed that the jet penetration from a strut injector is only dependent on the jet to air dynamic pressure ratio, Q, regardless of the other flow conditions. This is not the case for the flush wall injector because the wall boundary layer is susceptible to shock waves, which is known to affect the injector behavior. The unique case where a backpressure induced shock wave coincides with the injector bow shock is also presented. It was shown, for the flush wall injector, that the presence of the shock increased the disorder of the mixing layer structures, implying that the mixing rate is enhanced by the presence of this shock.

Finally, Background Oriented Schlieren (BOS), to be discussed in section 3.4, is a flow imaging technique. The application of BOS to a scramjet fuel-air mixing environment has not been reported in the literature before this work. The BOS signal was proven to be directly correlated to the line-integrated helium mixture fraction by correlating the image data with gas sampling data. This proof was non-trivial because the BOS technique measures density gradients across the line-of-sight and is not on its own a measure of helium. The correlation is significant because it can be used to calculate the mixing efficiency from the BOS image data continuously across the combustor flow axis.

1.4 Fuel Injection and Mixing Basics

Fuel injection and mixing is critical for controlling the operation of a scramjet because this process is directly related to the heat addition process which impacts the thrust and behavior of the pre-combustion shock train in the isolator. As the fuel becomes mixed it is burned using oxygen from the air to release the fuel's stored chemical energy into the airflow. [43, 69] To do this, fuel must be adequately injected and spatially distributed. This is a challenging task to accomplish because the air and fuel have a combustor residence time on the order of 5 to 10 milliseconds. [54] A designer could increase the length of the combustor to increase residence time; however, this option must be balanced with the weight and drag penalties that diminish the benefit of completely burning all of the fuel. Ideally the fuel is evenly distributed, at a stoichiometric mixture, throughout the combustor entrance cross section. The fuel is then burned in the shortest possible distance. For the case of inlet injection schemes this has been proven experimentally in direct connect subscale combustion experiments. [90] This is an example of a reaction rate limited system, because the only limit to the combustor length is how fast the reaction can take place. In most scramjet concepts the combustor is mixing limited meaning that the reaction rate time is much faster than the mixing rate. The Damkohler number, Da, is defined as the ratio of chemical to fluid dynamic time scales. It gives an indication of the reaction rates to mixing rates. Determining this ratio is a useful tool for CFD to model scramjet combustion. [17]

The process of fuel injection and mixing can be broken down into three components: placement (macro), swirling (meso), and diffusing (micro). Fuel placement is achieved by distributing injector ports on the flowpath wall and on struts in the flowpath cross section. Swirling of the fuel and air is achieved by introducing streamwise vorticity or

increasing the turbulence intensity near the fuel injectors. This occurs due to the flow structure around an injector port or can be induced by a mechanical surface such as compression, or expansion ramps. The swirling of the fuel and air increases the contact area between the two fluids. This is important because the molecular diffusion (micro mixing) occurs along the boundary between fuel and air.

1.5 History of Fuel Injection Research

Research in the area of scramjet propulsion systems across the broad scope of the field has historically been limited to fundamental component and sub-component experimentation, regardless of being a physical or computational experiment. The reason for this is that experimentation of complete scramjet engines or full-scale components are expensive. Hence the problem is broken down by engine components and physical phenomena. Research simulating and measuring the mixing in a DMSJ combustor has decades of precedence. There have been combustion tests and passive scaler tests, both of computational and experimental nature: each testing all different kinds of injection, mixing, and flameholding schemes. This section will give a historical perspective on the foundational knowledge that has been acquired.

1.5.1 Passive Scalar Mixing Tests

Passive scalar mixing refers to tracking the mixture fraction of an injected fluid, where the value of that mixture fraction has negligible impact on the fluid dynamics of the flow. Mixture fraction is defined as the ratio of injected fluid to total fluid by mass or mole. The passive scalar mixing assumption differs in contrast to a reacting flow where the mixture fraction has a direct impact on the chemical reaction, and will therefore affect

the fluid mechanics of the flow in that region. Endothermic chemical reactions increase turbulent kinetic energy, which promotes small scale mixing. [29] The heat addition to the fluid also causes a Rayleigh flow effect where the pressure increases and drives the Mach number toward unity.

Often for a passive scalar experiment a surrogate fluid for the fuel is used for purposes of the measurement technique or facility safety. For the fuel surrogate, a gas should be chosen with similar molecular weight and ratio of specific heats, γ. Simultaneously matching these conditions exactly is not typically possible. Studies have shown that molecular weight has an impact on penetration height of a jet in cross flow, however that impact is minor because ultimately the Q is what affects penetration. [21, 101] Therefore, if the molecular weight of the injected gas differs from the simulated gas, then in order to match the Q, the mass flow will be different from that of the fuel. Matching γ can be difficult as well. This flow property governs the jet expansion and velocity. It is important for interpreting results from a mixing experiment to be aware of these factors and to explain how they relate to an in-flight system. For these experiments helium has been chosen as the surrogate gas to simulate hydrogen fuel. This will be discussed further and throughout the subsequent chapters.

The stoichiometry is the proportion of molecules which balance the chemical reaction between the fuel and air. The fuel to air mass flow ratio, f, is normalized by the stoichiometric fuel to air mass ratio to give the equivalence ratio, ϕ, given by eq. 1.1. The equivalence ratio is an important parameter as globally it defines how much chemical energy is being delivered to the engine. Locally, the quantity gives information on the reactions in that area.

$$\phi = \frac{f}{f_{st}}, f = \frac{\dot{m_{fuel}}}{\dot{m_{air}}} \tag{1.1}$$

In a passive scalar experiment there are no reactions, however, it is necessary to define an equivalent stoichiometric mixture for the fuel surrogate in order to be able to compare the mixing results to a combustion experiment. If the molar stoichiometric mixture for the fuel is equated to molar mixture for the surrogate, then the difference in fuel to air mass ratio between the surrogate and fuel is due to molecular weight, see eq. 1.2.

$$\left.\begin{aligned} f^o_{surrogate} &= f^o_{fuel} \\ f_{st,surrogate} &= f_{st,fuel}\frac{MW_{surrogate}}{MW_{fuel}} \end{aligned}\right\} \tag{1.2}$$

The degree of comparison between passive scalar mixing in sub-flight-enthalpy tests to a reacting test was evaluated by McClinton. An experiment was set up where hydrogen combustion and helium passive scalar mixing were each tested in the same flowpath. For the non-reacting experiment, the mixing efficiency was calculated by integrating cross-sectional planes downstream of the injector. This was compared to results of a 1-D analysis, which takes the reacting experimental pressure and flowrate data as the input and calculates the combustion efficiency. The results of these tests concluded that sub enthalpy passive scalar mixing experiments can be used to infer the performance of scramjet combustion. The study showed that the flow is more symmetrical for the non-reacting tests, and that the magnitude of the turbulence was lower than in the combustion experiments. [72]

1.5.2 Simulating Dual-Mode Flow Environment

Ground test facilities are incapable of perfectly duplicating in-flight hypersonic flows. When designing a hypersonic ground experiment an understanding of the phenomena that must be simulated needs to be established, such that the proper facility can be chosen. Testing aerodynamics in hypersonic flows requires that the Mach number, Reynolds

number, and ratio of specific heats γ, be duplicated as nearly as possible. Combustion experiments however cannot relax temperature or velocity as they are critical for the chemical reactions and time scales to occur. [22, 79] This said, it has been shown by Mungal et al. that Reynolds number effects on mixing are weak due to the large-scale turbulence generated in the flow which dominates the near field mixing. This indicates that the Reynolds number can be a relaxed parameter as well. [81] Therefore, for a passive scalar test the Mach number is the most critical flow parameter that will affect the physics.

One of the objectives of this dissertation is to quantify the change in the mixing characteristics of an injector in a DMSJ as the combustor flow transitions from subsonic to supersonic. This requires simulating the pre-combustion shock train by exerting a backpressure on the flowpath. Scramjet inlets have been tested this way for decades using a mechanical throttling device. However it is a relatively more recent and uncommon experimental procedure for passive scalar mixing. The following are some examples of experimentation using these methods. Experiments by Gruber et al. and Donohue examined cavity flameholding and operability with a fuel surrogate and flow imaging to track the difference between scram and dual-mode operation of the combustor. It was found that the precombustion shock structure disrupted the cavity shear layer, reducing entrainment of upstream molecules into the cavity; however, it improved penetration of cavity products into the core flow. [38, 51] Backpressured passive scaler mixing tests have been done as well, though each experiment has been limited in scope. Tomioka et al. experimentally tested three flush wall injector concepts under backpressured and non-backpressured conditions. They recorded gas sampling and found that injection penetration was reduced in the backpressured case, but that the jet plume spreading was enhanced. [100]

1.5.3 Gas Concentration Measurements

For measuring the passive scalar mixing experimentally, this section will discuss many of the measurement diagnostics that have been used, both non-intrusive and intrusive. The methods for measuring and visualizing the mixing for the experiments of this dissertation are discussed in sections 3.3 and 3.4. The non-intrusive measurements are optically based with a light source and camera and the intrusive techniques require an aspirated probe and rake placed in the flowfield. Some of the non-intrusive techniques include Rayleigh scattering and Planer Laser Induced Fluorescence (PLIF). Rayleigh scattering is a laser based, non-intrusive technique where a laser sheet illuminates the gas, and the reflection of light off of molecules of a specific gas species is measured by an intensified CCD camera. [94] PLIF is a similar technique in that a laser sheet is used to illuminate a known section of the flow. However, instead of imaging the reflecting light, a seeded or naturally occurring species is fluoresced by the laser light and the fluorescence is then imaged by a CCD camera. Some examples include nitric oxide, iodine, and hydroxide, among many other species. [31, 76] Schlieren and shadowgraph imaging are other forms of optical measurements which rely on density gradients to diffract the light rays to create an image. These measurements are adequate for getting visual images of the flow structure, however for spatially resolved mixture fraction data these techniques have a high degree of uncertainty.

To quantify spatially resolved mixture fraction points in the flow, in-stream sampling systems have historically been the approach. A sample of gas is extracted from the flow via an aspirated probe such that the species constituency of gas stream is unbiased by differences in molecular weight. [101] From there the gas stream can either be channeled into finite sample tubes or through a free flowing analysis system. In order to

measure the constituent species, gas chromatography has been done for both reacting and non-reacting experiments. [67, 91] Another method for sensing mixture fraction, for free flowing analysis systems, is based on a hotwire or hotfilm sensor with a Constant Temperature Anemometer (CTA). Hotwire gas analysis measurements can detect changes in the mole fraction of a binary gas mixture through static calibration of known mixture fractions. For an in-depth description of the physics of hotwire gas sampling measurements, see appendix A.

Hotwire gas analysis measurements have been proven to be economic and reliable for measuring binary gas mixtures. In 1962, Blackshear and Fingerson were the first to apply a hotwire to measure either the temperature or concentration of a binary gas mixture. The design consisted of an aspirated probe with the hotwire mounted within the probe and upstream of a choked orifice. [14] In 1970, Way and Libby used two hotwire sensors to simultaneously measure composition and velocity. [104] In 1972, Brown and Rebollo took the concept and adapted it for measuring shear layers at constant temperature. [19] In the same year, Adler compared calibration measurements with a theoretical analysis and presents the sensitivity potential of the technique. [1] Jones and Wilson added a temperature-sensitive filament into the probe so that a temperature correction could be made achieving a resolution of 0.01 mole fraction. [63] Ahmed and So applied the Blackshear design to a subsonic combustor with swirling flow. [3]

The first application of this technique to supersonic flow was in 1973 by Devillers and Diep. However, the measurements were crude and required a known pressure and thermal environment. [34] In 1989, Ng and Ninneman took Blackshear's concept designing the probe tip for supersonic mass capture and by installing a pressure tap in the aspirated probe itself were able to make mixing measurements in a cold flow scramjet combustor. Prior to this innovation, measurements could not be taken within a varying

pressure field. [82] Doerner and Cutler took the original approach and improved on it for supersonic mixing experiments by anchoring the temperature and pressure of the gas flowing over the hotwire with an ice-bath and the laboratory room as a thermal and pressure reservoir respectively. [37]

1.5.4 Strut Fuel Injector Concepts

Strut fuel injectors are aerodynamic slender body devices which channel the fuel, protected, to injection locations away from the combustor wall. As combustor sizes scale larger, strut injectors are increasingly necessary to span the gap between injector ports. [36, 77, 78] An experimental and computational parametric study was performed by Hsu et al. where leading and trailing edge sweep angle, and injection locations were varied. Performance was evaluated based on local fuel equivalence ratio, total pressure recovery, and mixing efficiency. [30, 57, 58, 99] The researchers took a very holistic approach to this project, starting with CFD of a large number of concepts varying certain geometric parameters, then pairing down the number of concepts and performing passive scaler mixing tests, and finally combining the best strut design with a cavity flameholder, tested it under real combusting conditions. This is an ideal approach to injection and mixing research. The results and conclusions from these publications contributed to the design of the leading and trailing edge angles and placement height of the sidewall injectors for the strut in this study. In the referenced work it was reported that penetration from the tip injector was poor due to low pressure in the base region behind the strut. If the tip injector could be augmented by another injector then the performance of the strut to inject fuel into the core flow would be improved, because a shorter strut would be able to achieve the same fuel penetration. Hence this would reduce the internal drag

of the engine, and the thermal load on the strut. Quantifying the improvement of the fuel penetration is an objective of this research.

Aguilera and Yu took a different approach to using a strut. Their approach was to use the strut to block the cross flow in order to lift or "guide" the fuel jet from a wall injector into the core flow. [2] This study presents an interesting method for increasing pressure in the base of a strut. If a wall injector is coupled with injection from the tip of a strut then penetration above the strut could be much improved. This would also reduce the fuel flow requirement through the strut, which allows for a thinner strut because the tip injector port and the internal passage through the strut can be smaller.

Struts achieve mixing by placing the fuel where it needs to be, and allowing the fluid mechanics to move and distribute the fuel. They are generally coupled with separate devices or geometry features specifically for flameholding and further mixing purposes. For DMSJ combustors, cavity flameholders have shown excellent results. The union of a strut with a cavity has been shown to enhance the fluid interaction between the cavity shear layer and fuel-air mixture in the core flow. A major contributor to this is the reduced pressure of the wake region downstream of the strut which lifts reaction products into the core. [46, 52] Struts have also been designed with geometric mixer attributes.

For increasing the mixing from a strut, ramps and wedges are attached to the trailing edge of the strut. These features are added in differing ways in order to increase the contact area of the fuel-air boundaries by generating vorticity in the wake of the strut. This improves the mixing but consequently has increased total pressure losses due to increased entropy. These results have been computationally and experimentally verified in non-reacting cases. [39, 40] Combustion cases of an alternating wedge design on the

trailing edge were performed by Sunami et al. These tests show that the supersonic mixing is enhanced by the wedges and, in later tests, claim that the design increases operability and combustion control. [96, 97]

1.6 Summary of Chapters

Chapter 2 will give an overview of the physics of the experiment, including the basic principles of compressible viscous flow, fuel injection and mixing, and DMSJ operation. In chapter 3, the design of the experiment is presented. Described are the facility capabilities, the equipment and experimental systems, and the Design of Experiments (DOE) methodology. The methods for processing and extracting the mixing characteristics from the BOS and gas sampling data are discussed as well. Lastly, the design of a swept strut fuel injector with tip injection is outlined, and a parametric analysis of the injector hole configuration was performed with a computational analysis. In chapter 4, the flowfield surrounding the strut tip injector is analyzed. The mixing characteristics of the strut tip injector is presented for the Mach 2 case along with a flush wall injector to give a baseline for the results. In chapter 5, the results of mixing in a backpressured flowfield is examined. First, the inviscid flow structures are analyzed for their impact on the mixing jet. Then, instantaneous BOS images of the flush wall injector are analyzed to examine the effects of backpressure-induced shocks on the helium jet. The results of the mixing efficiency as the flow regime transitions from subsonic to supersonic is evaluated. Lastly, the jet penetration is analyzed for the strut and flush wall injectors and a unique case is presented where the backpressure-induced shock coincides with the injector bow shock for both injectors. Chapter 6, gives a summary of the results, and discusses the significance, implications, and future work as a result of this research.

Chapter 2

Dual-mode Scramjet Fuel Injection

The dual-mode scramjet flight regime is defined as having a combustor entrance with large portions of mixed supersonic and subsonic air flow. There are shocks and large regions of separated boundary layer. In general the flow environment is very complex, making this flight regime an interesting propulsion and combustion problem. This chapter will explain the flow physics which affect the fuel injection and mixing in order to give context on why the injection and mixing process is a critical element of the DMSJ engine. This foundation will be important for the discussions in the latter chapters. Then this chapter will discuss the impact that the fuel injection and mixing has on the operation of a scramjet engine, the implications of increased engine scale, and definitions of the characteristics of mixing.

2.1 Background Physics

2.1.1 Compressible Mixing Layer

The previous chapter discussed that reactions between the fuel and air occur where the molecules are able to interact, such that the mixing of these fluids is an indicator of the combustion. The mixing layer is where the fuel-air molecular diffusion occurs, which is called micro-mixing. This increases with increased contact area of the two fluids. The structure of the mixing layer has a direct impact on the contact area, and so these regions have a direct impact on the mixing rate. This section will discuss what a mixing layer is and how the mixing layer structures influence the mixing.

A mixing layer is a specific case of a viscous shear layer. In a simplified example case used to study the mixing layer, two streams of fluid traveling tangentially at differing velocities meet along a plane. [26] See fig. 2.1 for a diagram of the mixing layer flow field. The mixing layer develops between these two streams. The mixing layer is composed of vortex eddies, which grow in diameter and spacing as they convect downstream, at times amalgamating into larger structures. The growth and spacing of these structures is linear with downstream distance, and the velocity of the structures are constant. These characteristics of the mixing layer are a function of the density and velocity difference between the two streams of fluid. [20] The vortex eddies of the mixing layer are unstable for all Reynolds numbers as well. [65] In a scramjet combustor, mixing layers form at the boundaries between the fuel jets and air flow. In a scramjet combustor, there are numerous points of fuel injection, therefore mixing layers are present throughout a scramjet combustor.

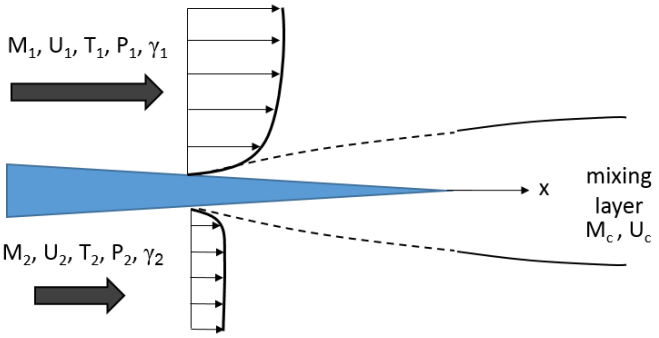

FIGURE 2.1: *Diagram of the mixing layer flow field.*

The convective Mach number, M_c, was created as an indicator for compressibility of a mixing layer. Equation 2.1 shows the convective Mach number relative to the fluid streams on either side of the mixing layer. The idea is that the convecting structures within the mixing layer are traveling at a velocity relative to each stream of fluid on either side of the mixing layer. The relative convective velocity is non-dimensionalized by the speed of sound of the respective fluid stream, in order to determine a close estimate of the fluid's compressibility. One can imagine that if the convective Mach number were to exceed 1, shocklets would form in the mixing layer boundary. When the static pressure and temperature are constant through the mixing layer, and for each fluid stream on either side of the mixing layer, then the relative convective Mach numbers of eq. 2.1 can be related by eq. 2.2. When the γ of the two fluid streams on either side of the mixing layer are the same then eq. 2.1 becomes; $M_{c_1} = M_{c_2} = M_c$. [16, 85]

$$\left.\begin{aligned} M_{c_1} &= \tfrac{U_1 - U_c}{a_1} \\ M_{c_2} &= \tfrac{U_c - U_2}{a_2} \end{aligned}\right\} \tag{2.1}$$

$$\left(1 + \frac{\gamma_1 - 1}{2} M_{c_1}^2\right)^{\frac{\gamma_1}{\gamma_1 - 1}} = \left(1 + \frac{\gamma_2 - 1}{2} M_{c_2}^2\right)^{\frac{\gamma_2}{\gamma_2 - 1}} \tag{2.2}$$

Clemens and Paul redefined the convective Mach number, given by eq. 2.3, so that it could be more readily applied to mixing layers where the two fluids have differing specific heat ratios. They found that the effect of compressibility on a mixing layer structure is to increase the three-dimensionality and increase the large-scale stirring structures [28]. This is an interesting contrast to how compressibility has a stabilizing effect on the entire mixing layer, by reducing the growth rate of the layer thickness [16, 61]. It has also been observed that compressibility reduces the turbulent eddy length scales [18], and reduces the Reynolds stresses [42, 61].

$$M_c = \frac{U_1 - U_2}{a_1 + a_2} \tag{2.3}$$

This means that in a DMSJ combustor, as the inflow conditions slow due to the pre-combustion shock-train, velocity decreases and with it mixing layer compressibility. Therefore, the mixing layer growth rate can be expected to increase and the three-dimensionality of the layer will decrease.

2.1.2 Gaseous Jet in Supersonic Crossflow

A transverse gaseous jet in a supersonic crossflow is the most common flow scenario applied for supersonic fuel injection. This flow scenario can be applied as a jet issued from the combustor wall, off of a strut, or in a cavity, etc. For this reason, the transverse jet has been well studied in the literature. The jet is characterized by the penetration and plume spreading, with a pair of counter-rotating vortices within the jet. A bow shock is generated upstream of the jet injector orifice, there is an upstream and downstream separation of the boundary layer, which reattaches some distance downstream. The jet is almost always underexpanded at the fuel injector orifice exit, and oscillates between

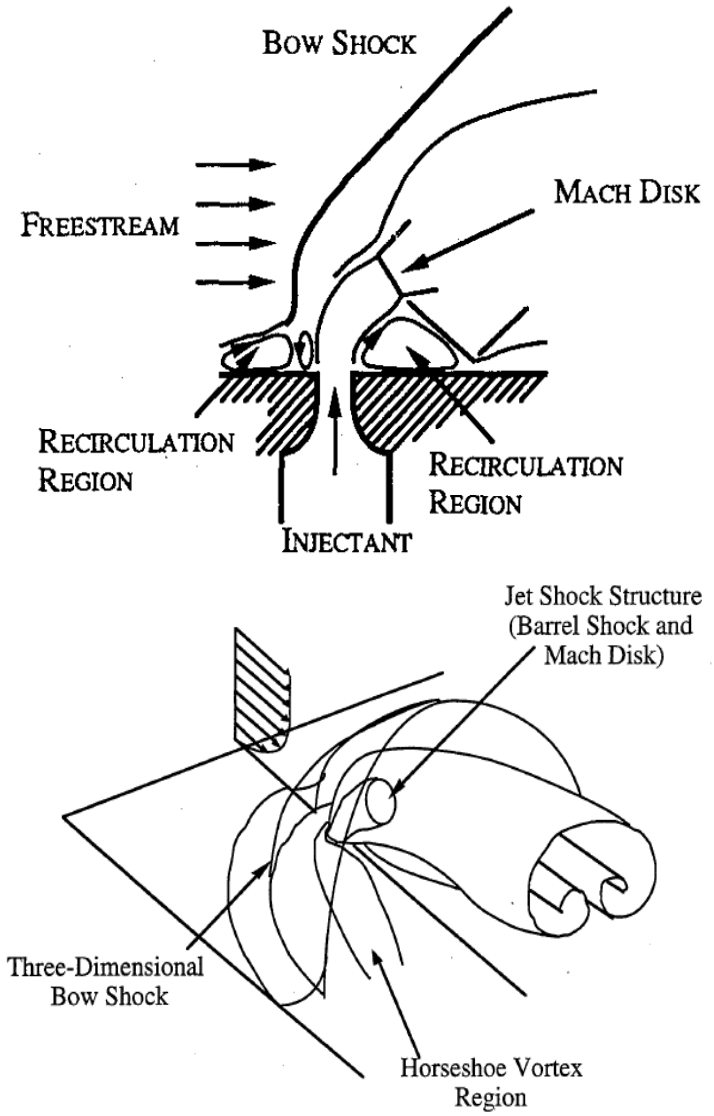

FIGURE 2.2: *Transverse jet injected into supersonic flow. (top) spanwise view, (bottom) showing counter-rotating vorticies [25, 48]*

expansion and compression as the jet pressure equalizes to the surrounding pressure. A Mach disk forms in the jet when the jet flow approaches a sonic condition. [48] A sketch of this flow is shown in fig. 2.2.

Papamoschou and Hubbard found that the primary parameter effecting the jet penetration is the jet-to-freestream momentum ratio, Q, (also known as the dynamic pressure ratio). The jet and freestream Mach number did not matter much and the static pressure ratio of the jet exit to local freestream did not have a significant effect

on penetration. [84] This means that there is not much that can affect penetration after the gas leaves the injector orifice. Hollo and McDaniel observed that once the fuel is injected the jet plume spreading is strongly dependent on the strength and size of the streamwise vorticity structures in the near field. This is the stirring effect which takes the mixing layer between the jet and freestream and turns and twists it increasing the mixing layer surface area. As the jet plume travels downstream, in the far field the small scale turbulent eddies dominate the flow and act to smooth out the jet plume spreading so that the rate of jet plume growth is consistent regardless of how the fluid was injected. It was observed that the distance at which the large-scale vortex structures break down is approximately 10 to 20 jet diameters. [56] Therefore, this distance will be used to loosely estimate the transition from near field to far field mixing.

Numerous analytical correlations have been generated from experimental data to track jet penetration. There are varying definitions of penetration; some analyses use the jet centerline, while others use the highest jet boundary detected. The distinction is important because the difference between these two calculations can be substantial. The JETPEN code is a jet penetration analysis code based on an analysis by Billig et al. where the height of the Mach disk is calculated based on momentum ratio and an effective jet backpressure. Then mass, momentum, and energy is used to calculate the jet plume trajectory downstream from the center of the Mach disk. [12, 13] The JETPEN analysis calculates the jet centerline.

Gruber et al. applied a power law developed for a subsonic cross flow, and found that for momentum ratios between 2 and 3, eq. 2.4 accurately calculates the jet boundary in supersonic flow, where Y is the penetration distance measured from the injector orifice, and D is the diameter of the injector orifice. [48] Other power laws have been generated from experimental data to fit the upper boundary of jet penetration as well. [84, 91, 93]

McDaniel and Graves performed experiments at low momentum ratios from 1 to 0.3, which falls into the range of some of the previously formulated power law fits. However, the available relations did not fit the data. They instead used a logarithmic relation, shown in eq. 2.5. Similar to the power law fits, it follows the upper jet boundary. [76]

$$\frac{Y}{D \cdot Q} = 1.23 \left(\frac{X}{D \cdot Q} \right)^{0.344} \tag{2.4}$$

$$\frac{Y}{D} = Q \cdot 0.344 \cdot ln \left[2.077 \left(\frac{X}{D} + 2.059 \right) \right] \tag{2.5}$$

2.1.3 Pre-Combustion Shock-Train

When a strong enough adverse pressure gradient is introduced to a supersonic internal flow it causes a series of normal and/or oblique shock waves to form in the duct. These waves interact with the boundary layer causing regions of separation and reattachment. The shock-boundary layer interactions are highly dependent on the incoming Mach number, boundary layer thickness, pressure gradient, and geometry of the duct. In a DMSJ the isolator duct is designed to contain these shock waves formed by the combustor pressurization. The shocks form to balance the static pressure so the pre-combustion shock-train is a phenomena that adjusts to the downstream conditions in the combustor.

In a simplified system, with no boundary layer, a single normal shock will form in the duct to raise the static pressure. As the boundary layer thickens, the planar shock forms a bifurcated lambda shock. The shock structure is governed by the resistance of the boundary layer to separate. If the isolator pressure ratio, P_c/P_i, required to separate the boundary layer is weak enough then oblique shocks form. P_c is the peak combustor pressure and P_i is the isolator entrance pressure. The oblique shocks can reflect until the core flow can no longer support a reflected shock system. Notice that in fig. 2.3a

the boundary layer is sketched as a thin layer relative to the duct diameter such that the core can support the reflections. As the boundary layer thickens relative to the duct diameter a normal bifurcated shock system forms until the static pressure meets the combustor pressure. This is sketched in fig. 2.3b, where it can be seen that the boundary layer is purposely depicted as thicker (i.e, the schematic is not to scale). [102]

Waltrup and Billig found that the length of the pressure rise, s, is inversely proportional to Mach number and Reynolds number according to eq. 2.6, and directly proportional to the duct height, H, and boundary layer momentum thickness, θ, according to eq. 2.7. A quadratic formula, given by eq. 2.8, was fitted to the data. With a known P_c/P_i, M_i, and θ the formula yields a prediction of the incipient separation point of the boundary layer. [102] The distance from the incipient separation point to the flowpath exit pressure is, s, defined as the length of the pressure rise or shock train length. A demonstration of using eq. 2.8 to design DMSJ isolators has been shown by Le et al. [66]

$$s^{-1} \propto \left(M^2 - 1\right) Re_\theta^{1/4} \tag{2.6}$$

$$s \propto H^{1/2}\theta^{1/2} \tag{2.7}$$

$$\frac{s\left(M^2 - 1\right) Re_\theta^{1/4}}{H^{1/2}\theta^{1/2}} = 50\left(\frac{P_c}{P_i} - 1\right) + 170\left(\frac{P_c}{P_i} - 1\right)^2 \tag{2.8}$$

The experimentation by Waltup and Billig simulated the combustor pressurization with a backpressuring device. This means that the physics occurring within the combustor were not simulated, and therefore any interaction between these physics and the shock-train could not be identified. Fotia and Driscoll examined the shock-train in a simplified combustion environment. They observed that the combustor flow blockage,

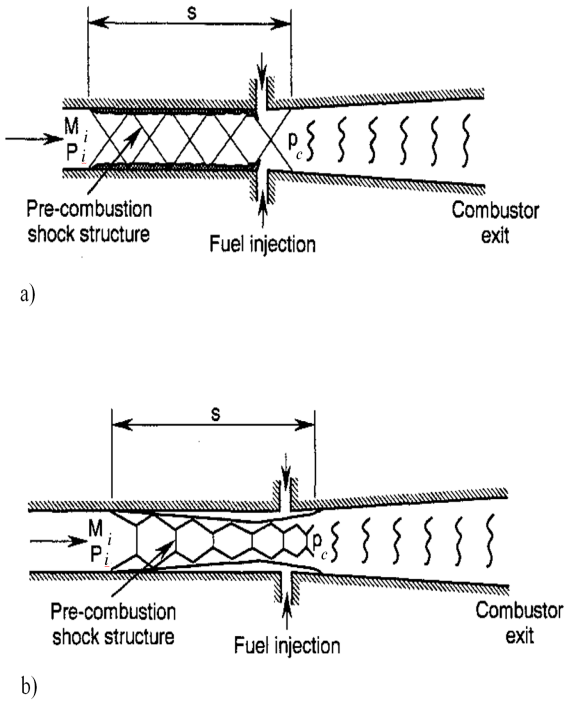

FIGURE 2.3: *Pre-combustion shock-train structure in a DMSJ isolator. [95] (a) oblique shock structure, (b) normal bifurcated shock structure*

caused by both fuel injection and combustion, has an influence on the shock-train. A methodology was developed to map the isolator/injector interaction due to these factors. The injector that was tested was a flush wall normal injector with a cavity flameholder. This is important because it shows that the performance of the injector has an impact on the isolator flow. [45]

Sullins peformed a simulated acceleration of a DMSJ from Mach 5.85 to 6.2. During the transient experiment, the process of establishment and extinction of the pre-combustion shock-train happened abruptly and was found to be very sensitive to fuel flow rates. [95]

This all means that designing a flowpath for the pre-combustion shock-train is critical for accelerating a vehicle from Mach 4 to 8. The stability, strength, and length of the shock-train is closely dependent on the pressure, fuel injection, and mixing that

occurs in the combustor. In addition, due to the cross-coupling of the shock-train and combustor, when the combustor conditions change, the isolator flow in turn changes, which then feeds upstream to the combustor. This can potentially exacerbate the unsteadiness of the system as seen in references [95] and [44]. In practice the geometry of the flowpath can and should be designed to avoid this unbalanced process.

2.2 Impact of Fuel Injection and Mixing on Engine Operation

Operability for a DMSJ refers to a limit of engine operation due to either inlet contraction ratio, isolator backpressure, or combustor flameout. There are two general flow events which can occur in a DMSJ isolator; one is unstart, and the other is ram-scram transition. These events are based on three points which define the engine mode operation: the incipient separation point, the peak pressure magnitude and location, and the thermal choke point. [7] See fig. 2.4 for an example of the layout of these points in a DMSJ in both ramjet (ram) and scramjet (scram) modes of operation. Where the ram mode of operation is indicated by a pressure disturbance upstream of the combustor and a thermal choke downstream of the combustor peak pressure point. Scram mode is characterized as having supersonic flow throughout the engine such that there are no combustion induced shock waves upstream of the combustor, and no thermal choke. Ram-scram transition, for a properly designed engine flowpath, is not an unstable process, nor does it result in a sudden loss of thrust. It will however have an impact on the engine cycle efficiency and as such it is an import design consideration. [54] The transition is very sensitive to changes in the flow Mach number and enthalpy, boundary layer thickness, and combustor blockage, and the transient action to one mode or the

other can happen rapidly. [44] This section shall discuss the effect fuel injection and mixing has on unstart and mode transition.

Unstart is a term used to describe a scenario where the incipient separation point moves out of the isolator entrance causing the air mass capture of the inlet to decrease. In section 2.1.3 it was discussed that the fuel injection and combustion processes affects the pre-combustion shock train, and therefore control of these processes is necessary for the engine operation.

A quasi-one-dimensional analysis has been developed by Auslender as a prediction methodology for determining the susceptibility of an inlet to unstart due to the combustor blockage. The analysis uses Re_θ at the incipient separation point to determine the maximum attainable combustor pressure for a given flowpath geometry. [6] The analysis does not investigate the specifics of the interaction but gives a high level algorithm for predicting the instability and was well correlated to experimental data.

While prediction algorithms are key for engine design, development of a detection

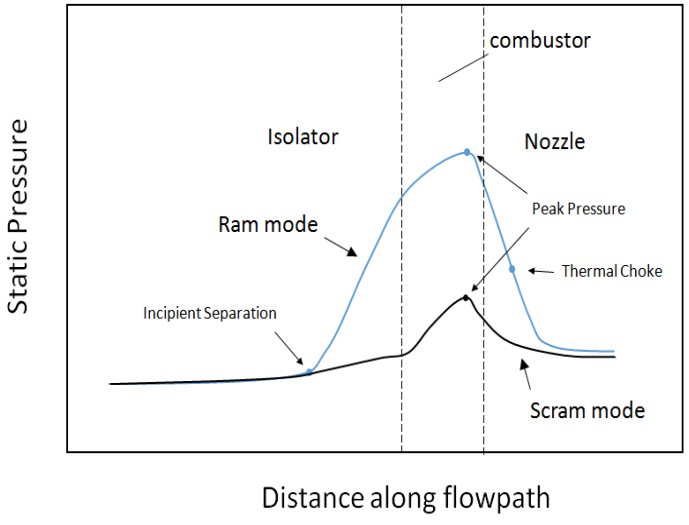

FIGURE 2.4: *Sketch of the static pressure trace in a ram vs. scram mode operation of a dual-mode scramjet.*

methodology would be useful for unforeseen events that could trigger unstart during a flight. Experimental data was collected with high frequency pressure transducers in order to locate rapidly moving shock waves in the isolator. These data were used to generate dynamic models to predict the pressure profiles. [59] In subsequent experiments a control scheme was developed to control the position of the shocks. [5] These models represent the physical relationships between the three defining points of the engine: incipient separation, peak pressure, and thermal choke. They combine the physics of injection, mixing, and combustion into an effective area blockage and use it as the exit boundary condition for the isolator.

In each of these referenced works the experimentation was performed with a mechanical backpressuring device to simulate the combustor blockage. It has been shown experimentally that for a well designed flowpath the pre-combustion shock-train position is not effected by combustion driven pressure fluctuations. These experiments proved that flow blockage is the only combustor parameter that effects the shock-train. [7] As was reported in the previous section, Fotia and Driscoll found that the fuel injector blockage has a major influence on the shock-train length in the isolator. [45]

Aguilera and Sunami each reported that the jet penetration and heat release profile was shown to strongly effect mode transition from ram to scram mode. This means that as penetration increases more fuel can be injected and burned before transition from scram to ram occurs. [2, 97] By burning fuel in the core the combustion zone is stretched out causing the peak pressure location to be further downstream in the combustor, thereby pulling the incipient separation point toward the combustor. The mode transition occurs when the incipient separation point moves into the combustor. Stretching the combustion zone downstream has an adverse affect on the combustion

efficiency for a constant length combustor. Therefore, when designing the engine system the injector type and combustor length must be sized appropriately.

For a DMSJ system, a low drag injection device with maximal penetration is ideal. With a fixed geometry, flow blockage is a function of the fuel injection locations and combustion, which is related to the mixing. These two parameters also happen to define the heat release profile, and hence peak pressure location. It has already been discussed in section 1.5.2 that mixing, heat release, and pressure are all closely tied together in a scramjet combustor. [72] In a flight engine scenario the only control knob is the fuel flowrate and/or injection locations. Therefore, understanding how the injection and mixing effects these three critical points of engine operation is important.

2.3 Complications of Fuel Injection and Mixing for Increased Scale Engines

As stated in the opening paragraph of chapter 1, the three applications of scramjet engines are for; delivery of orbital payloads, point-to-point travel, and military strike weapons. Each application has a specific set of mission requirements and in turn requires different performance attributes from the engine. One of the requirements is thrust. Thrust is produced in a jet engine by changing the momentum of the air moving through it, thereby using the air to push the vehicle forward. Thrust will scale directly with the mass flow of air through the engine. Therefore, the engine capture area must be made larger to produce more thrust. The scale of the engine increases with increased mass flow of air through the engine. The common vernacular for discussing engine scale is based on a 1x scale engine having 10 lb/s of airflow, and any multiple of that from there.

For example a 10x engine has 100 lb/s of airflow, a 0.5x engine has 5 lb/s of airflow, and so forth.

The combustor flow conditions; Mach number and enthalpy are independent of engine scale. Therefore, flow structures such as shock and expansion angles, boundary layer growth, and flame propagation are independent of scale as well. As the engine scale changes, the relative size and interaction of these flow structures with the engine geometry changes. This affects the strategy of how to provide adequate heat release in the combustor. [15, 57] For example when increasing the engine scale, the boundary layer thickness relative to the combustor duct height will be much smaller, drastically changing the impact of shock-boundary layer interactions. The location of shock and expansion wave interactions will also change with respect to the reaction zones, and could cause areas of high or low static temperature effecting the heat release. Diskin and Northam found that the combustion efficiency was highly dependent on geometry, and as scale increases the combustor length and divergence cannot be proportioned from a smaller scale design. [36] Since most of the DMSJ knowledge base is centered on 1x scale engines, much research is necessary going forward to learn how to build larger scale engines.

Struts have been identified as having excellent potential to meet the challenges of fueling large-scale engines. The reason is that the low aspect ratio of a strut limits the flow blockage and hence the internal drag due to these devices, and the fuel penetration from a flush wall injector is limited by the fuel pressure. With minimal impact to the flow, struts can place fuel in the combustor core flow in order to reduce the fuel gap between injector holes. To achieve the same penetration from a flush wall injector, an impractically high pressure would be necessary. [77, 89, 98]

2.4 One-dimensionalized Mixing Characteristics

Mixing alone is not an adequate quantification of the performance of one injector versus another because mixing tends to have comparable trade-offs in drag. The requirements for fuel penetration in the combustor must be considered as well. To quantify the performance of an injector, the mixing, drag, and fuel penetration, are represented by one-dimensional mixing characteristics; mixing efficiency, total pressure recovery, and jet penetration. In this section the one-dimensionalized characteristics: mixing efficiency and total pressure recovery will be defined. The jet penetration is a more straightforward metric defined as the upper boundary of the fuel, measured from either the wall surface or the height of the injector port, depending on how it is specified. Since the mixing efficiency and total pressure recovery are associated, an overall efficiency is defined which integrates these two metrics along an axial length of interest. The relationship between the mixing efficiency and total pressure recovery is not explicitly known, therefore, an equal weighting is assumed for each when it is multiplied to create the overall efficiency term. The one-dimensionalized Mach number will also be defined because it is a useful way to describe the overall flow regime. Lastly, this section will discuss some of the historical research and general properties of the mixing efficiency reported in the literature.

The mixing efficiency, η_m, is a one-dimensionalized value created as a convenient means for tracking the mixing performance of an injector. Furthermore, it is a quantifiable means of comparing injectors which have different qualitative mixing plumes. The mixing efficiency, given by eq. 2.9, is defined as the amount of fuel or its simulant that has reached the stoichiometric mixture for the proposed fuel, divided by the total flux of fuel or its simulant through the area of integration. This is only valid for a globally

lean mixture of fuel and air. In eq. 2.10, χ_r is the mixture of fuel that would react if no more mixing were to occur. [10, 68]

$$\eta_m = \frac{\int \chi_r \ \rho U dA}{\int \chi \ \rho U dA} \tag{2.9}$$

$$\chi_r = \begin{cases} \chi & \chi \leq \chi_{st} \\ \chi_{st} \left(\frac{1-\chi}{1-\chi_{st}} \right) & \chi > \chi_{st} \end{cases} \tag{2.10}$$

The total pressure recovery, Π, is a one-dimensionalized value for tracking the flow potential for doing work. It is defined by eq. 2.11, where the total pressure, P_t, is weighted by the mass flux and integrated over the cross section, and normalized by the free-stream flow defined at the entrance condition, or some other consistent initial state. [10]

$$\Pi = \frac{\int P_t \rho U dA}{\int (P_t \rho U)_\infty dA} \tag{2.11}$$

Since the flow can have large portions of supersonic and subsonic velocity, it is convenient to use a one-dimensionalized Mach number to describe the overall flow regime. For these tests the mass flux weighted Mach number is used to give an approximation of the Mach number to the bulk movement of flow. It is defined, at each axial station, by eq. 2.12. [9]

$$M_{ave} = \frac{\int M \rho U dA}{\int \rho U dA} \tag{2.12}$$

Northam and Anderson created mixing efficiency correlations for perpendicular and parallel injection in order to bound the problem of mixing as a shortest and longest case, respectively. The first observation was that for parallel injection and an equivalence ratio of 1, the length to achieve a mixing efficiency of 1 is given by eq. 2.13, where S is the distance between injection orifices also referred to as the gap. This means that

for parallel injection the mixing follows the linear growth rate, as shown by eq. 2.14. In the case of perpendicular injection the growth rate is logarithmic, as shown in eq. 2.15. They report that, for an injection angle between 0 and 90 degrees to the flow, the mixing efficiency can be interpolated between the eqs. 2.14 and 2.15. [83]

$$x_l = 60S \tag{2.13}$$

$$\eta_m = \frac{x}{x_l} \qquad parallel\ injection \tag{2.14}$$

$$\eta_m = 1.01 + 0.176\, ln \left| \frac{x}{x_l} \right| \qquad perpendicular\ injection \tag{2.15}$$

Taking the derivative of these two mixing efficiency equations yields the mixing rate for each limiting case, where eq. 2.17 will converge to eq. 2.16 as x gets sufficiently large, meaning that as the fuel travels far enough downstream from a normal injector, the fuel plume spreading rate will converge to that of a parallel injector. Setting eqs. 2.16 and 2.17 equal in eq. 2.18 and substituting x_l for $60S$ yields the distance at which this occurs, $x = 10.56S$, for a fuel equivalence ratio of 1. This location represents the point at which the change in fuel/air mixing with downstream distance, x, is independent of how it is injected. This downstream length from the injector is called the near field, and is the distance that a designer has control over to increase or decrease the level of mixing achieved. Downstream of the near field is the far field, where the mixing increases linearly with distance. The cutoff point of $10.56S$ for the near to far field agrees well with the reported work by McDaniel. [76] Note that these results are all relative to S, meaning that an appropriate gap must be chosen such that this analysis is valid for the injectors in question.

$$\frac{\partial \eta_m}{\partial x} = \frac{1}{x_l} \tag{2.16}$$

$$\frac{\partial \eta_m}{\partial x} = 0.176\frac{1}{x} \tag{2.17}$$

$$x = x_l(0.176) \tag{2.18}$$

McClinton et al. propose an analytic fit for data of a thrust optimized injector design. They found that a mixing length of $16S$ and 80% efficiency produced maximum thrust for this configuration. This work highlights the importance of designing components for the overall system benefit instead of optimizing individual components. [74]

Chapter 3

Experimental Setup

3.1 Mixing Study Facility

The experiments for this dissertation were performed in the Mixing Studies Facility (MSF), shown in fig. 3.1, at the NASA Langley Research Center (LaRC). This facility is a non-heated supersonic flow test facility useful for aerodynamic investigation of the physics of mixing and testing flow diagnostic techniques and equipment. High-pressure air is supplied to the MSF from a 600 psi bottle field through a 6 inch pipe. The air supply for the MSF is delivered via a pneumatic shut-off valve and throttle valve to a plenum connected to a supersonic nozzle. The flow exhaust is open to the laboratory and ducted through a pipe in the ceiling. The facility controls are located in an adjacent room. In the plenum there is a flow conditioner, which straightens and unifies the flow before entering the supersonic nozzle, the plenum chamber is 15.75 inches in diameter by 43.3 inches tall. The total temperature is measured upstream of the flow conditioner, and the total pressure is measured between the flow conditioner and supersonic nozzle. The nozzle for this experiment is a rectangular convergent-divergent Mach 2 nozzle,

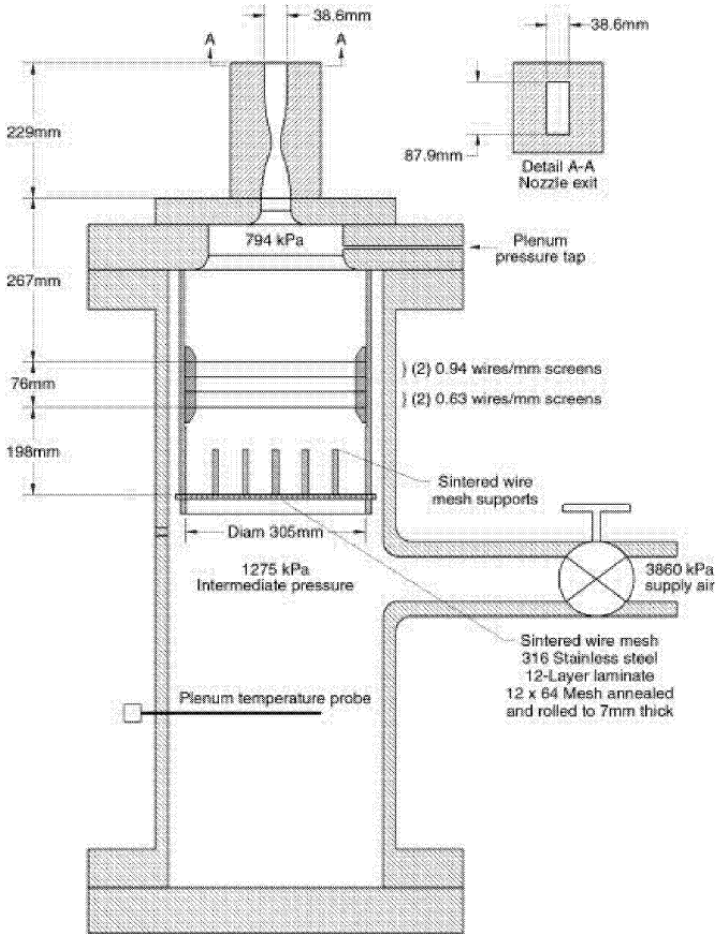

FIGURE 3.1: *Schematic of the MSF at NASA LaRC. [37]*

with an exit cross section that is 1.52 inches by 3.48 inches. The experiment flowpath is mounted to the nozzle and has the same cross section along its entire length. The nozzle and flowpath are oriented vertically and the flow direction is upward. The duct exit is open to the laboratory room, and the exhausting airflow is ducted out through a roof vent. The plenum air pressure is the only facility control, which is operated by a manual dial. The dial pneumatically positions a throttling valve which reduces the 600 psi supply air to the operating pressure for the plenum.

Labview 11 is the software package used for the Data Acquisition System (DAS), with four data acquisition cards: NI-6210, NI-6215, and two USB-6200. In total 20

instrumentation channels were sampled from these cards. A Pressure Systems Inc. Initium mainframe with two scanner modules was used to scan 32 static wall pressures plus two in-stream pressure probes, for a Pitot and static pressure measurement. The Initium system was controlled by a Labview utility and incorporated into the experiment program sequence.

Helium is supplied to the fuel injectors from a bank of 32 K-bottles located outdoors. The flow of helium is metered by an unchoked ASME orifice 0.25 inches in diameter with a known curve for the discharge coefficient vs. Reynolds number. The differential pressure, absolute upstream pressure, and downstream static pressure are measured across the orifice to calculate the mass flow. When full, the helium bank pressure is 2300 psi and the set pressure for the fuel injector is 180 psi, therefore, a large pressure reduction is required initially and will change as the helium tanks are emptied. To handle these requirements, the system was designed with two pneumatically loaded regulators so that neither regulator would have a differential pressure over 2000 psi across it, and so that a constant upstream pressure would exist for the second regulator. This design provided a very steady and consistent helium injection pressure from experiment to experiment. An explanation and schematics of the design of the system are given in appendix B.

3.2 Flowpath Hardware

The flowpath is a straight wall segmented duct so that the flowpath length can be incrementally varied. A solid model of the flowpath is shown in fig. 3.2. This was necessary because the in-stream probe measurements could only be made at the flowpath exit. Therefore, in order to take measurements at multiple cross-sectional planes downstream

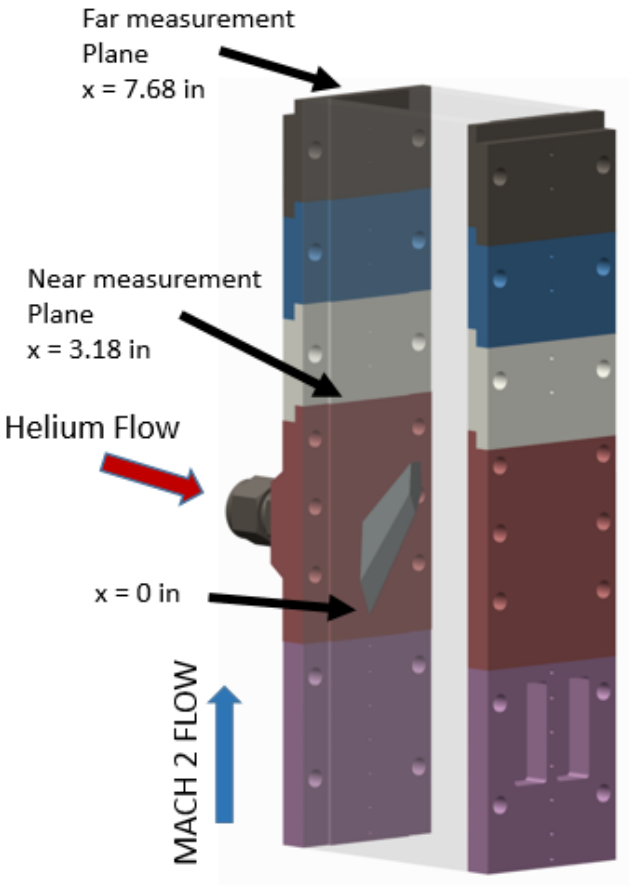

FIGURE 3.2: *Front isometric view of the experimental flowpath with the strut injector installed. The bottom of the flowpath is mounted to the top of the facility nozzle, and flow direction is upward.*

of the fuel injector, a different length was needed for each measurement plane. The flowpath sections are as follows. There is a 3.5 inch isolator section between the nozzle and injector section. There are two 2.5 inch long injector sections. One is a 90 degree, circular, flush wall injector, with an orifice diameter of 0.16 inches. This injector was used as a baseline for the strut injector and for proof of technique measurements. The second injector is an original strut design which will be the center piece for this dissertation. The development, design, and pre-experiment analysis of this injector is discussed in chapter 4. There are two sets of acrylic windows, one is 6 inches and the other is 11 inches. The windows are for the schlieren and shadowgraph visualizations.

3.3 Gas Sampling and Analysis System

For these experiments, hydrogen fuel is to be simulated by helium. Helium was chosen as the surrogate gas because of the similar molecular weight to hydrogen. The sensitivity of a hotwire signal to changes in the concentration of helium with air has excellent signal range mostly due to the contrasting conduction coefficient. [88] Finally, helium is inert, making it a safe and non-corrosive material to work with. A hotwire (or hotfilm) can be used to measure the concentration of two gases based on the hotwire sensitivity to convective heat transfer. [87] The Constant Temperature Anemometer (CTA) is essentially a Wheatstone bridge with a feedback servo amplifier which keeps the wire resistance, and hence temperature, constant with a response of up to 1000 times faster than the hotwire's natural response to the thermal conditions. [64] Heat transfer from the wire is a function of the gas properties: temperature, pressure, velocity, and composition. In order to control these properties so that the composition can be measured, a thermal reservoir is designed to maintain the sample gas stream at a constant temperature using the laboratory room as a thermal reservoir and constant pressure by venting the sample stream to the room. Lastly, a portion of the sample gas stream is siphoned off near the vent, and channeled to the hotwire sensor. A sonic orifice is placed just downstream of the hotwire so that the velocity is a function of only the composition. Now a direct relationship can be made between the CTA voltage signal and the gas composition. [19, 37, 82] The relationship between the CTA signal and the gas composition is determined via a calibration, where the mixture fraction is stepped from the pure species of one gas to the other. Therefore, a consequence of using this method is that the experiments are limited to using a binary gas mixture with differing heat transfer coefficients. The coefficient of thermal conductivity is the primary gas property that

effects sensitivity of the system. Air is the free-stream gas, therefore, a fuel surrogate gas with a coefficient of thermal conductivity different from that of air should be chosen.

The device developed for this experiment to measure the time-averaged concentration of helium in air is called the Gas Sampling and Analysis System (GSAS). The physics of how the system operates and makes a measurement is further discussed in appendix A. At the heart of the GSAS is a Dantec hotfilm sensor, mounted inside a cylinder with 3/16 inch ID, called the hotwire block. A Dantec Mini-CTA outputs a 0-5 volt signal. The measurement flow is sampled by an aspirated probe, a small portion of the sample stream is siphoned off into the hotwire block; it flows around the hotfilm, and then downstream of that is a choked orifice. The rest of the sample stream is emitted to the laboratory so that a constant pressure of 1 ATM is maintained at the hotwire.

The calibration consisted of seven steps in helium to air mole fraction, mf, from 0 to 1. To control the flowrate of Helium and Air supply, a flow controller was constructed by attaching a Velmex rotation stage to a needle valve. A Cole-Parmer 0-5 SLPM digital flowmeter measured the flowrate for each stream. A labview algorithm was written to cycle the needle valve open and closed to step the Helium/Air mixture from a mole fraction of 0 to 1. 500 samples per step are collected at a sample rate of 100 sample/s; see appendix A for figures of the calibration data and a description of how the data is reduced to get the calibration curve, and uncertainties. The maximum error from the calibration is applied to the data from each experiment; table C.1 shows the mean and maximum calibration errors for each run day. The mean error of the calibrations from every run day was $2.2\%FS$, where FS is the full scale of the measured range from 0 to 1 mf. Repeating experimental conditions over multiple run days helped to smooth out variations in the error, this will be discussed further in section 3.7.

3.4 Flow Visualization Technique

The GSAS provides time-averaged point measurements of helium concentration in the flow. The measurements are limited, however, to the two measurement planes of the experiment. Background Oriented Schlieren (BOS) was selected to resolve the helium jet spreading and penetration, and, if possible, visualization of instantaneous flow structures throughout the experimental flowpath. Schlieren is an optical measurement and flow visualization technique that images density gradients. Physically this can be done because the index of refraction of a gas is relational to the density per the Gladstone-Dale relation. When a light ray passes through a medium with changing index of refraction, it bends and distorts according to Snell's law. Helium is less dense than the main airflow, and, therefore, the boundaries of the helium jet and airflow are visible. Figure 3.3 shows a schematic of a BOS setup. The advantage of BOS over other Schlieren techniques is that the diffraction of the light rays are measured at every pixel of the CCD camera. The BOS technique operates by a set of flashed LED's which light up a randomized background pattern. The light reflects off of the background and travels through the experiment flow and is then imaged by the CCD camera. This appears as a waviness of the background pattern in the captured images. A cross-correlation algorithm tracks the deviation of the pattern from its original state captured in a clean image with no flow. The resultant is a vector for each pixel of the image displacement. The magnitude of the vectors are directly related to the integrated density along the path of light rays contacting that pixel. [47] Thereby quantitative density information can be measured along the line-of-sight for each pixel. [8] The camera used is a LaVision high frame rate camera designed for Particle Image Velocimetry (PIV) which allows for a double pulsed image 0.04 seconds apart. The semi-instantaneous images can be used to measure the bulk velocity of the helium jet by tracking coherent structures of the mixing.

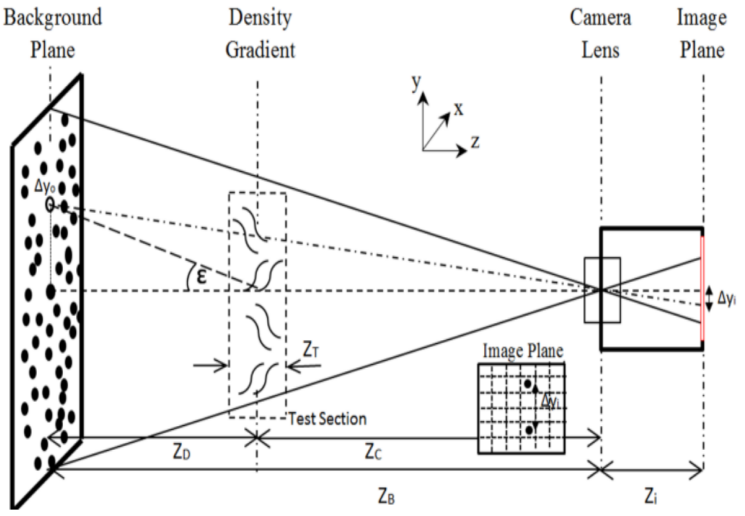

FIGURE 3.3: *Schemaic of a BOS setup. [47]*

BOS was ultimately chosen for these experiments over standard Schlieren or another imaging technique because for standard Schlieren high-quality glass windows are necessary and would have had to be fabricated, standard Schlieren also would require space around the flowpath that was not readily available in this facility. The ability to analyze the displacement vectors for density gradients was considered a bonus and not an objective of the study, so in the planning process it was not considered a driver of the visualization technique. As testing began, a noticeable relationship between the BOS and gas sampling data was observed and analyzed, this will be discussed in section 3.9. Shadowgraph imaging, which is similar to Schlieren in that it images the second derivative of density, was also set up, but only as an operational tool for visualizing shock wave location during the experiment. A laser-based measurement was considered, however, safety requirements for the MSF were not in place, and the window quality limited the possible uses of the laser. BOS presented an excellent option. Reflections from the window are not an issue for direct perpendicular viewing because the light rays through the test section are not collimated. The field of view can be much larger because it is not limited to the size of focusing mirrors.

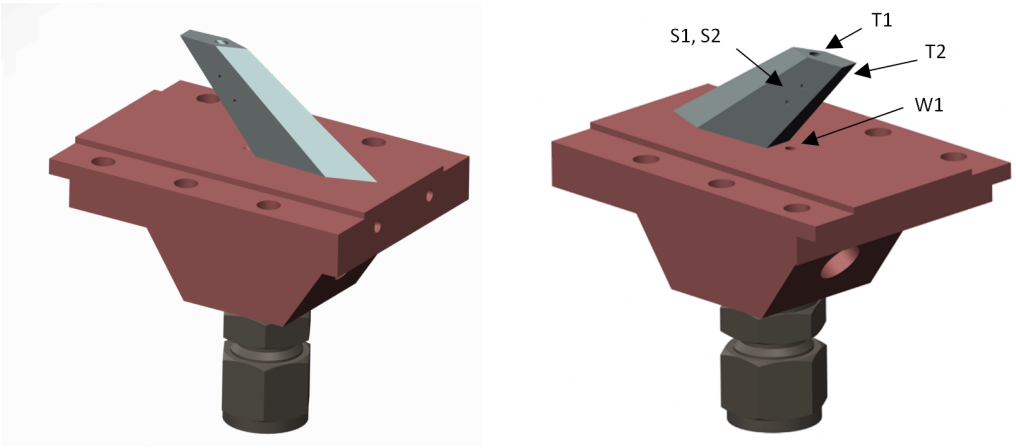

FIGURE 3.4: *Solid model of the Strut injector; (Left) Front isometric view, and (Right) Rear isometric view.*

3.5 Design of the Strut

The strut for these experiments is pictured in fig. 3.4. The height of the strut, h_{strut}, is 1 inch, and the sweep angles of the leading and trailing edges are 42 and 36 degrees, respectively. There are injector ports located on the strut tip, labeled T1, at the wall, labeled W1, and on the sidewall, labeled S1 and S2. The sweep angles and sidewall injector port placements were adapted from the conclusions of Tam et al. [99], in which a numerical study of 14 struts, each having a variant of these features, was done. This study found that the sweep angles and sidewall injector placement had the highest mixing efficiency for the lowest total pressure loss. In a continuation of this research Hsu et. al. [57] used these results to experimentally test the best design from Tam et al. One of the variants of these struts had a tip injector, however, the results showed that the penetration of fuel from this injector was insignificant compared to the other cases. The design of the strut injector for this dissertation will address this problem.

For this study, the dimensions for the width of the strut injector was an iterative process. The width of the strut at the tip was sized to be wide enough to fit the tip injector, and the width of the strut at the base was sized to limit the pressure drop

of the helium as it flowed up the inside of the strut. An initial width, tip injector size, and supply pressure were chosen from estimates of the target helium flowrate and penetration. These targets were based on a theoretical fueling area of half of the nozzle exit area. To estimate the penetration, the correlation of eq. 2.4 was used. It was assumed that this correlation would overpredict penetration for the Mach 2 cases due to essentially no boundary layer at the strut tip compared to the wall. The process was iterated manually until the penetration predicted was roughly 1.6 inches, and the predicted pressure drop through the strut was roughly 0.25 psi. The finalized width of the strut tapers from 0.375 inches at the wall to 0.12 inches at the tip.

Initial designs of the strut included an injector port on the trailing surface of the strut near the tip, angled 15 degrees to the wall. This injector port was later removed, which will be discussed in section 3.6. Each of these injector holes are straight drill holes and have sonic underexpanded jets issuing from them. The hole diameters and angles of the holes with respect to the flow direction are given in table 3.1. There is a cavity section that protrudes from the outside wall of the strut injector, pictured in fig. 3.4. The cavity provides the room for a stagnation chamber for the helium, and provides room to support plumbing fittings for the helium flow, pressure transducer, and thermocouple. The interior of the strut is hollow with a wall thickness of 0.03 inches. To manufacture this part, it was 3-D printed using a process called Selective Laser Sintering (SLS) where powder metal, in this case stainless steel, is laid down in layers and sintered by a laser to build up the part. Without this manufacturing technique, fabrication of a strut like this would be impractical.

TABLE 3.1: *Strut injector holes for CFD geometry and Experimental geometry.*

Injector	CFD D [in]	Exp. D [in]	Angle [degree]
T1	0.1	0.1	54
T2	0.1	0	15
W1	0.085	0.125	46
S1	0	0.04	87
S2	0	0.04	87

3.6 Pre-Test CFD Analysis

A CFD analysis was performed by DePiro and Quinlan to assess the flowfield around the strut, and to investigate various injector port configurations prior to the experiment. The Viscous Upwind aLgorithm for Complex flow ANalysis (VULCAN) CFD package was used to numerically simulate the experimental flowfield. VULCAN solves the complete three-dimensional viscous Navier-Stokes equations, augmented with species continuity equations. A grid convergence study was done on a fine, medium, and coarse grid. There was an issue with the grid due to the S1 and S2 injectors, so they were removed to get the solution to converge. [33] At the time of running these cases it was not expected that removing these injectors would affect helium jet penetration, and the experimental results will show that is the case. To give perspective each pair of side injectors will supply the same mass flow as one of the tip injectors. The injectors were also modeled as rectangle holes instead of circular holes as was done experimentally. This was done to simplify grid generation around the injectors. The cross-sectional area was matched for each injector port so that the mass flows would be as close as possible to that of a circular injector port. In total, four cases were run for two injection pressures. Each case varies the three centerline injector locations (T1, T2, and W1). See table 3.2 for each tested configuration and the parameters. The flow conditions tested were for the non-backpressured experimental case having $P_\infty/P_e = 1$, Mach 2, $P_t = 115$ psia, and

TABLE 3.2: *Test Matrix for the CFD cases.*

Config.	Injector [psia]	Press [g/s]	$\dot{m}_{he}$	Q	$Y_p/D\ \vert_{max}$
C1P1	T1,T2,W1	242	21.0	1.44	
C1P2	T1,T2,W1	300	26.0	1.79	4.90
C2P1	T1	242	8.0	1.44	
C2P2	T1	300	10.0	1.79	3.80
C3P1	T1,W1	242	13.0	1.44	
C3P2	T1,W1	300	17.0	1.79	5.75
C4P2	W1	300	7.0	1.79	3.78

$T_t = 300$ K.

Figure 3.5, shows contours of the helium mole fraction for each case at $Q = 1.44$. The helium mole fraction contours highlight the importance of the shape of the strut. The leading and trailing edge sweep angles and the tapered width help to promote upward movement of fluid away from the wall. The mechanism driving this is a high to low pressure gradient from the wall to the flow centerline in the wake region of the strut. This is significant for alleviating wall heating, it also should be considered if this strut is coupled with a flameholder as reported by Hsu et al. [58] The right side of fig. 3.5 shows cross plane slices of mole fraction. The shape of the mole fraction contour on these slices shows the progression of the jet plume and how the counter-rotating vortices curl the top of the jet outward and down. These vortices are small relative to the fueled area, which is the full width of the duct and half of the duct height.

The mixing efficiency, η_m, and total pressure recovery, Π, are calculated using eqs. 2.9 and 2.11, respectively. These performance characteristics are plotted for each test configuration in fig. 3.6. From this figure it can be seen that the total pressure recovery is relatively consistent across each test configuration. This is because the total pressure loss of the system is mostly due to the geometry of the strut and not the fluid interaction of any of the injectors. The maximum penetration of helium into the core flow seems to

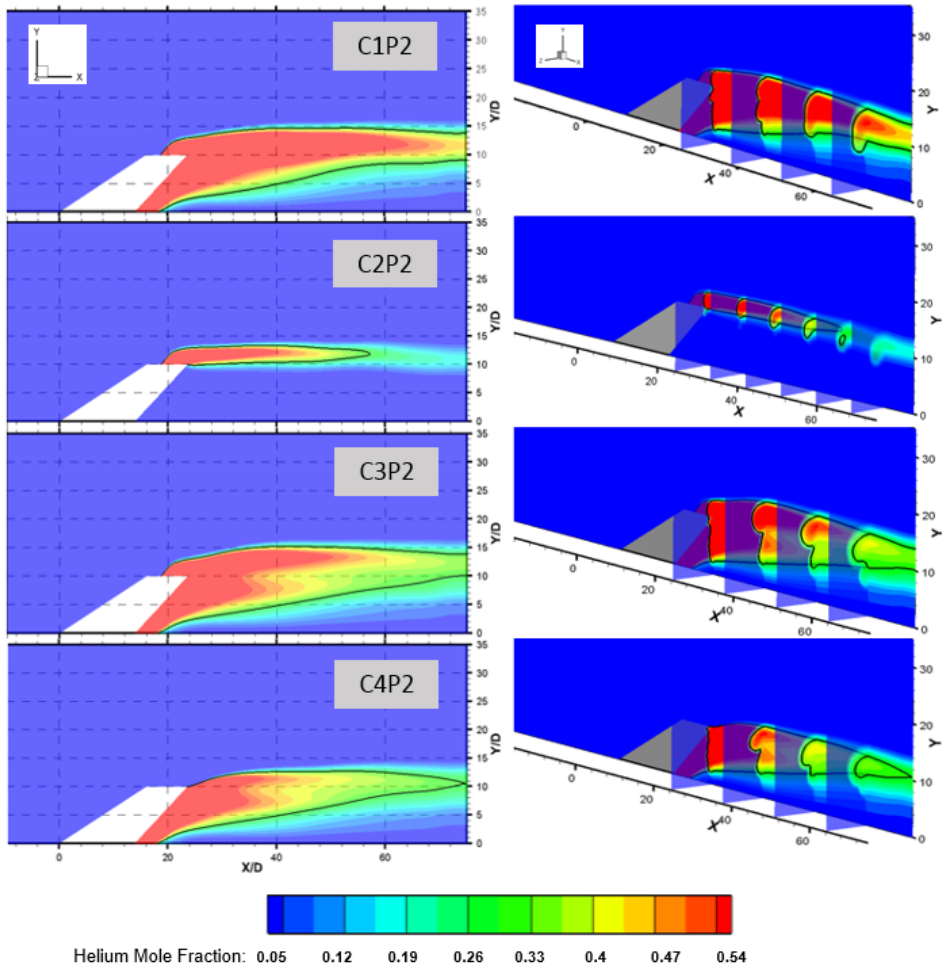

FIGURE 3.5: *Helium mole fraction contour plots for P1, flow is left to right. The black contour line is stoichiometric molar mixture fraction, 0.296. (Left) Spanwise view of centerline slices for each test configuration. (Right) Isometric view of cross plane slices showing the progression of the Helium jet.*

be the principle driver of the spread in total pressure recovery among test configurations. Both Case 2 and Case 4 have nearly identical maximum penetrations, but Case 2 uses the T1 injector while Case 4 uses the W1 injector, and both exhibit the exact same total pressure recovery trace.

The purpose of this analysis was to gain insight into the aerodynamics of the strut geometry, placement of the injector ports, and the total pressure of the helium. From these results, it was decided to test the Case 3 configuration. The reason for choosing this configuration over Case 1 was because Case 3 had a higher penetration and from

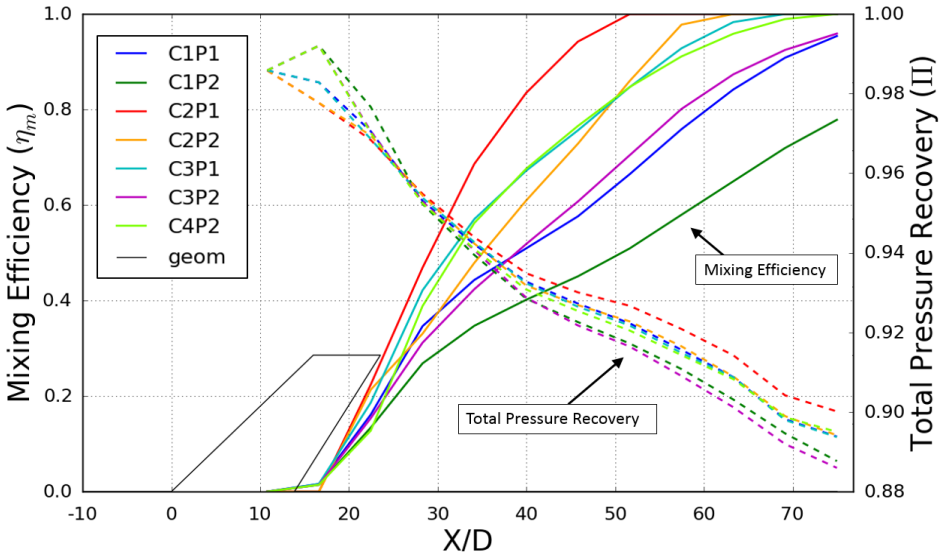

FIGURE 3.6: *Mixing efficiency and Total pressure recovery of the tested strut configurations.*

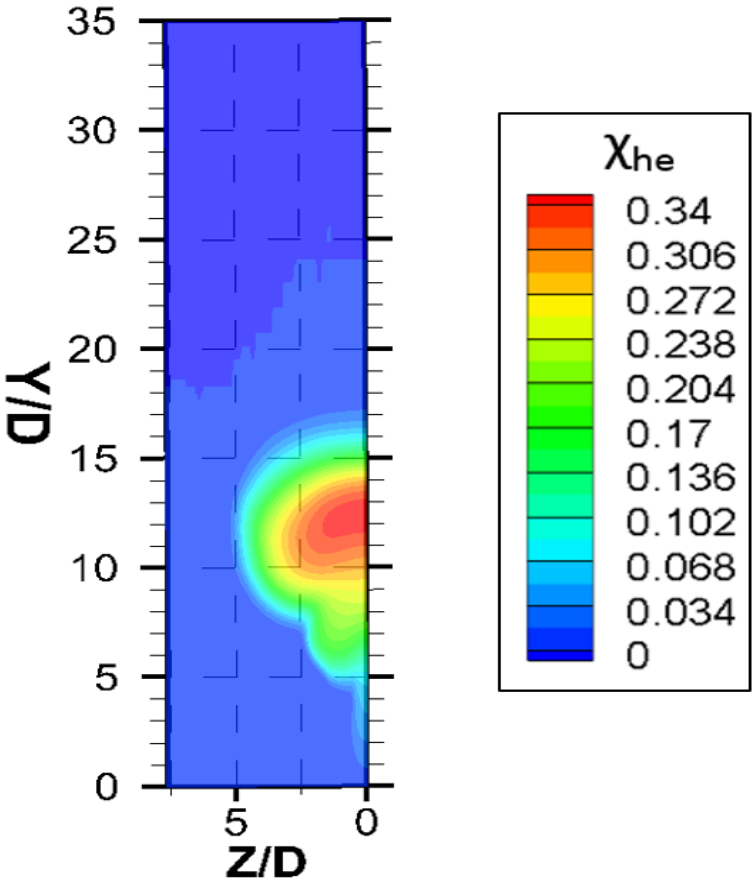

FIGURE 3.7: *CFD configuration C3P2; helium mole fraction contour at* $X/D = 75$.

examining fig. 3.5; Case 3 appears to have a greater potential for penetration because it has the greatest contribution of y-momentum per mass injected. For Case 1 it appears that the T2 injector blocks some of this energy from impacting the T1 jet. From the CFD it is also evident that while increasing the injection total pressure, from P1 to P2, it did not greatly improve penetration. Therefore, for the experiment, a lower injection pressure will be used and the injector hole diameters will be increased, as listed in table 3.1. These adjustments were made to meet a target total helium mass flow of 19.5 g/s, which was determined to have a wide distribution of mole fractions at the far measurement plane, $X/D = 76.8$ for configuration C3P2. The helium mole fraction contour plot at this plane is given in fig. 3.7.

3.7 Design of Experiment

3.7.1 Matching Conditions for Multiple Flowpath Lengths

An experimental challenge is simulating the conditions around the injector for different flowpath lengths, which is necessary for making in-stream measurements at multiple axial locations. The process will be to run an experiment with one flowpath, disassemble and reassemble the flowpath with a shorter duct, and re-run the same nominal conditions. However, if the same facility plenum pressure is used and the flowpath exit is open to the atmosphere so that the exit pressure is always 1 atm, the conditions around the injector will be different for the different flowpath lengths. When the flowpath length is changed the pre-combustion shock train adjusts based on the nozzle exit Mach number, pressure ratio over the flowpath, and the flowpath length. Equations 3.1 are reduced from eq. 2.8 to show the proportionality of the facility plenum pressure to the length of the shock train. The change in pressure is inversely proportional to the square of the change in

length. The overall change in Reynolds number due to the static pressure inconsistency will be relatively small and therefore can be neglected, according to reference [81].

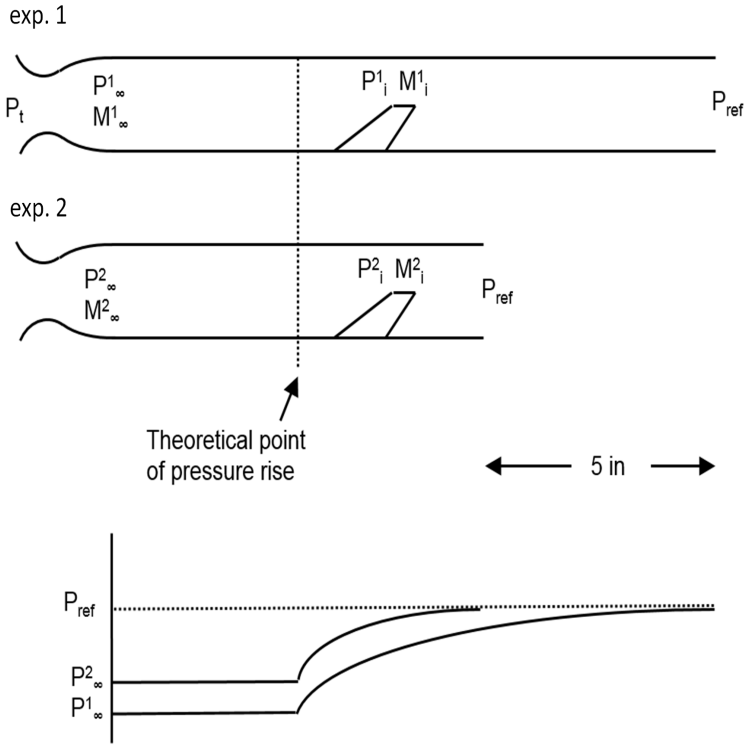

FIGURE 3.8: *Representation of how the pressure has to change for an equivalent experiment between case configurations of the flowpath.*

$$\begin{aligned} &\frac{P_{ref}}{P_\infty} \propto \sqrt{C_1 + C_2 s} \\ &since, P_{t,air} \propto P_\infty \\ &\therefore \frac{1}{\Delta P_t} \propto \sqrt{1 + \Delta s} \end{aligned} \tag{3.1}$$

To keep the fuel equivalence ratio, ϕ, constant between experiments, the fuel pressure must be adjusted to maintain a constant ratio of fuel to air total pressure. Given that the geometry of the facility nozzle and fuel injector does not change, the mass flow of air is proportional to $P_{t,air}$, and the mass flow of helium is proportional to $P_{t,he}$. This is assuming that the nominal temperature does not change between experiments as well. Therefore $\phi^1 \cong \phi^2$, where the superscripts refer to either exp. 1 or exp. 2 in fig. 3.8.

3.7.2 DOE Methodology

Modern Design of Experiments (MDOE) is an approach to experimentation where the experimental knowledge and capabilities are leveraged to maximize the effectiveness of an experiment. This is in contrast to One Factor At a Time (OFAT) methods where a large volume of data is required, and relies on accuracy of the individual data points and consistency of experimental factors. With the MDOE method a researcher seeks to achieve high quality by tactically choosing the test points through identification and incorporation of all known sources of errors and real-world imperfections such as random variations, and systematic errors. Systematic errors can consist of temperature or pressure variations over time, which are slow compared to the time required to collect a set of data points. These uncontrollable variables which can affect the system response are called covariates. With a priori knowledge of the experiment through either operator experience or pre-test operation of the facility the researcher can identify the covariates of the system. [32]

Sometimes it is not possible to identify all of the covariates of a system, or if they are known, to alleviate their impact. Therefore, in order to protect the quality of the data, the tactic used is randomization and repeating, which will smooth out the errors from the covariate effects. Randomization means that the data collection process is done in a non-uniform pattern either in space or over some control variable domain. During an experiment systematic errors, due to covariates, can cause the data to skew with a time dependence because systematic errors are not necessarily constant. If the error is plotted over time in the order the measurements were collected there would be a visible trend to the plot. However, if the data set was completely randomized, when the error is plotted over the control variable domain, then the error should be evenly distributed

around a constant error. [32] Repeating test points is used as a tool for identifying the presence of, and alleviation of systematic errors. However, there is a trade-off between sample time and total number of data points. Employing randomization and repetition into a data collection strategy can greatly reduce the amount of data needed to limit or explain errors in the data due to real world effects. [86]

The coordinate locations for the gas concentration measurements were chosen such that the data collection was randomized and repeat locations were intermittently collected; the procedure is discussed in the following section. The repeat test points were used to determine sensitivities of the output variables to the inputs, and to determine the uncertainties in the measurements. Part of the MDOE process aided in choosing the input conditions such that a response in the measured outputs will meet the objectives of this study. Due to resource limitations, a trade-off was evaluated to limit the number of test conditions, but still have enough data to determine a response of the output variables to the input variables. As a result, three flow conditions were tested for, supersonic, subsonic, and sonic, where the flow regime is defined by the mass-averaged Mach number. This gave three points to map the response of the flow condition to the mixing characteristics, for the two injectors that were tested. Lastly, only two measurement planes were scanned with the rake, and the BOS measurement was used to complete the gap of information about the mixing between the near measurement plane and the far measurement plane. Using the BOS in this way minimizes the amount of runs needed to measure the mixing along the entire flowpath. The trade-off is that information about the mixing is lost between the two measurement planes because the BOS gives an integrated measure of the helium across the light ray line of sight.

3.7.3 Experiment Procedure

Initial testing was focused on measuring the centerline helium jet penetration. The CFD was used to estimate the location of the large gradients in the mole fraction distribution so that the measurement points could be placed strategically. As testing progressed more information became available such as penetration vs. X from the BOS images and maximum jet spreading from contour plots generated from the far plane gas sampling. This information was used to generate the coordinate locations, and limit the number of experiment runs needed to gather data for each measurement plane. The path that the rake traversed through the measurement coordinates was created manually. The path was semi-randomized, meaning that the rake had a logical path but moved in a fashion that would still be random in relation to the mole fraction distribution (see fig. 3.9a). The randomization is important for smoothing out errors when the data is combined from multiple experiments into a single plane of data. Repeat test points were added in where convenient for the rake path, points were repeated within each experimental run and between each repeated experiment.

There is a time delay for the gas sampling measurement due to the distance that the sample must travel through tubing from the aspirated probe to the hotwire sensor. The timing delay was measured for the strut and for the flush wall injector at both measurement planes. The method to measure this time was to turn the fuel on while collecting data. The absolute time stamp for when the helium injection pressure jumped versus the absolute time when the CTA signal jumped was then calculated. For the downstream measurement plane, referred to as the far plane, the time delay was fairly constant everywhere, however, between the supersonic cases and subsonic cases there was a need to adjust the delay in the Labview programming. For both injectors at the

near plane, the variation in time delay was significant across the plane. The time delay was therefore set as an input based on location so that a unique time delay could be set on a point-by-point basis. To simplify, three time delays were selected and given ranges of Z and Y where they were valid. The coordinates were then given the appropriate time delay and listed in the input deck which also contained the coordinate data to send to the motor controls. In the end, the programming would move the rake to the next coordinate location, pause for the time delay, take data 100 samples in 0.3 seconds, then move on. During each run, a real-time shadowgraph camera was used to visualize the flow and control the shock position.

3.7.4 Test Matrix

Two planes were scanned with the in-stream rake at X/D of 31.8 and 76.8. The reference diameter, D, is 0.1 inches, which is the T1 injector diameter. For each plane, three different air flow conditions were tested. The test matrix in table 3.3 lists the run numbers 'S' for the strut experiments and 'R' for the flush wall injector experiments. The Mach condition refers to the mass-averaged Mach number at the exit plane. The rough estimate prior to testing was to have a supersonic, sonic, and subsonic flow in the mixing region such that a relationship could be determined between the flow physics and mixing characteristics. Each cell in the table represents a set of data that will be combined to calculate, contour plots of helium mole fraction, mixing efficiency, total pressure recovery, and 1-D mass-averaged Mach number.

TABLE 3.3: *Experimental Test Matrix.*

	Strut		FWI	
$X/D =$	31.8	76.8	31.8	76.8
Supersonic	S21,S24	S7,S14,S17	R10	R14
Low Supersonic	S22,S25	S8,S15,S18	R11	R15
Subsonic	S23,S26	S10,S16,S20	R12	R16

3.8 Using the Experimental Data

The experiment has four input variables: total pressure and total temperature of the air and helium, which have some response on the measured variables, χ_{he}, P_{pit}, P_s, and Y_p/D. These variables are defined as such: χ_{he} is the helium mole fraction, P_{pit} is the Pitot pressure, P_s is the static pressure, and Y_p/D is the upper boundary of the helium jet, i.e, the jet penetration. These measured variables are used to calculate the output variables; χ_{he}, P_t, Mach number, velocity, and density, which are subsequently used to determine the mixing characteristics; η_m, Π, and Y_p/D, as well as the dynamic pressure ratio, Q, and mass-averaged Mach number, M_{ave}. Once the data was collected, methods were constructed to build the output variables from the raw measurements. See appendix C for details about these methods.

The repeatability and accuracy of the facility operation to hit the nominal experimental conditions, shown in table 3.4, from run to run, was not exact. In order to compare data from different experiments the input variables were corrected using the factors defined by the equations of C.3. These corrections are applied to the air total pressure, air total temperature, equivalence ratio, and momentum ratio, respectively from top to bottom. Each correction factor is determined from the governing equations relating the input variable to the output, for instance in the case of the measured quantity, P_{pit}, which is dependent on Mach number, total pressure, and gas composition. An iterative routine is used to simultaneously calculate each of these properties from P_{pit} and χ_{he}, where Mach number is guessed within a range until the error is minimized. Appendix C discusses the methodology and equations for these calculations.

For each experiment that was run, the temporal distribution of input variables was plotted immediately in order to asses how steady the experiment behaved. At

TABLE 3.4: *Nominal Experimental Conditions*

Ave. Mach #	Supersonic	Sonic	Subsonic
Q	3.774	3.774	3.774
$P_{t,air}$ [psia]	115	55	35
$P_{t,he}$ [psia]	180	180	180
$T_{t,air,he}$ [K]	300	300	300

98% confidence, none of the experimental conditions varied more than 1% from the mean value. The run-to-run repeatability of the experiments was not as consistent with variations up to 5% in total temperature and up to 7% in total pressure of air. The mean variation of the χ_{he} and P_{pit} for the intra-run repeated measurement points was found to be $+/-0.041$ and $+/-2.86psi$ respectively. Considering the mean uncertainty in both of these measurements was $+/-0.043$ and $+/-5.04psi$ respectively, this indicates that the sample time was long enough to get an accurate distribution of the sample condition at each point, and that variations over the time of the experiment were within the experimental uncertainty of the measurements. Correction factors were calculated based on mean values of the input variables for each experiment and applied to each measurement variable. Then, the corrected values were accumulated and plotted into contours or integrated for calculating mixing efficiency and the 1-D mass-averaged Mach number.

Contour mappings of the helium jet were produced from the GSAS mole fraction measurements. The measurement points were interpolated onto a 100 x 50 point grid, using an 8-point interpolation in Tecplot. Figure 3.9b is an example of the contour map for the far field measurements of the supersonic test case; note that the scale for the color mapping is linear with χ_{he}. The black markers on the plot represent the measurement points, where the gas sampling probe collected the χ_{he} samples. Figure 3.9a shows the path that the gas sampling probe took as it scanned the measurement plane. Some of the jet plume features in the contour are a product of interpolation error. There

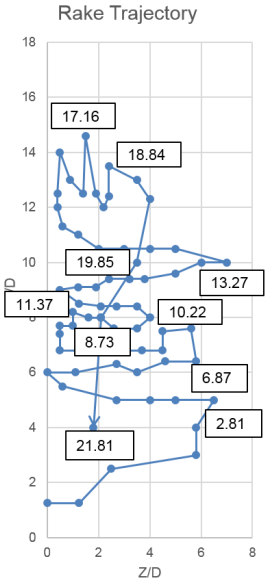

(A) *Path of the gas sampling probe took for run S17.*

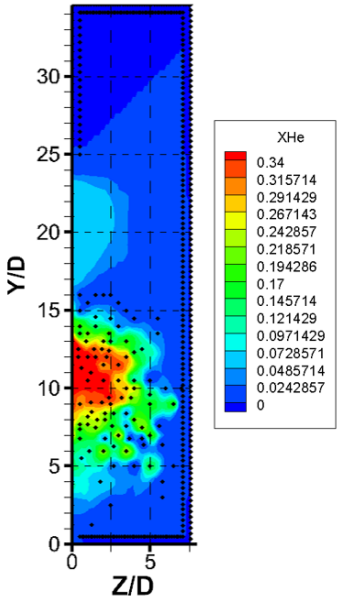

(B) *Helium mole fraction contour map for the supersonic case of the strut injector, for the measurement plane at* $X/D = 76.8$.

FIGURE 3.9: *Experiments S7, S14, and S17 are used to produce the contour above. The timing and locations of the measurement points are shown to the left for run S17.*

is a region of helium that is present in the contour, above the main jet, centered at $Y/D = 20$. There is not really helium here; it is a product of the interpolation between the measurement points at the top edge of the jet and the boundary conditions. The outer boundaries of the helium jet have very low χ_{he} of approximately 0.17, so small changes in the flowfield can have a distinct, qualitative impact on the outer boundary of the jet. The percent error also starts getting high for this area making the outer boundaries of the jet more difficult to resolve. Finally, in some of the locations, when the flow Mach number approaches unity, a normal shock will be unavoidable at the probe tip, this will cause a biasing towards the air because it has a higher molecular weight, i.e, greater inertia. The data reduction routine has a detection method for this (see appendix C). In the core of the helium jet, where most of the helium mass flux is, the average helium mole fraction is 0.30. The relative uncertainty is greater than in the outer boundaries, and consequently, the shape and size of the jet core is well resolved.

3.9 Interpreting the BOS Measurement

The BOS signal represents light ray displacement, which provides a measure of the line-integrated density gradient. To interpret what this means for an image of a helium jet in air, figure 3.10 shows a theoretical situation where there is a circular jet of helium in a rectangular stream of air. The jet boundary is perfectly separated between the two streams of gas such that no mixing has occurred. The light rays will follow a path such that the signal would be be zero at the center of the jet, and would go to a maximum value at the top and bottom of the jet. This phenomena was shown for a simple jet in supersonic co-flow using rainbow schlieren. [4, 80] If air is added to the jet such that its mole fraction is still uniform, but still not mixing with the surrounding air flow, then the overall magnitude of the signal would decrease, but the shape of the distribution would still be the same. This means that the BOS signal is dependent on both the magnitude of the change in density across the Line-Of-Sight (LOS), i.e., magnitude of helium mole fraction, and also the line width of the disturbance that the light ray travels through, i.e., the cross-sectional shape of the disturbance. This theory is validated by comparing a time-averaged BOS image with the time-averaged gas sampling measurements. A line of data, along the Y-axis at X/D of 76.8, was extracted from the BOS image and plotted against the normalized duct height, Y/D. A helium mole fraction contour plot is generated in Tecplot from the gas sampling measurements and set alongside the extracted BOS signal data, da. In fig. 3.11, the local maxima of the BOS signal correspond to the local maxima of the gradient of helium mole fraction with respect to Y. These local maxima in the BOS signal distribution indicate the boundaries of the shape of the helium jet.

The BOS signal will also have a dependency on the magnitude of the mole fraction.

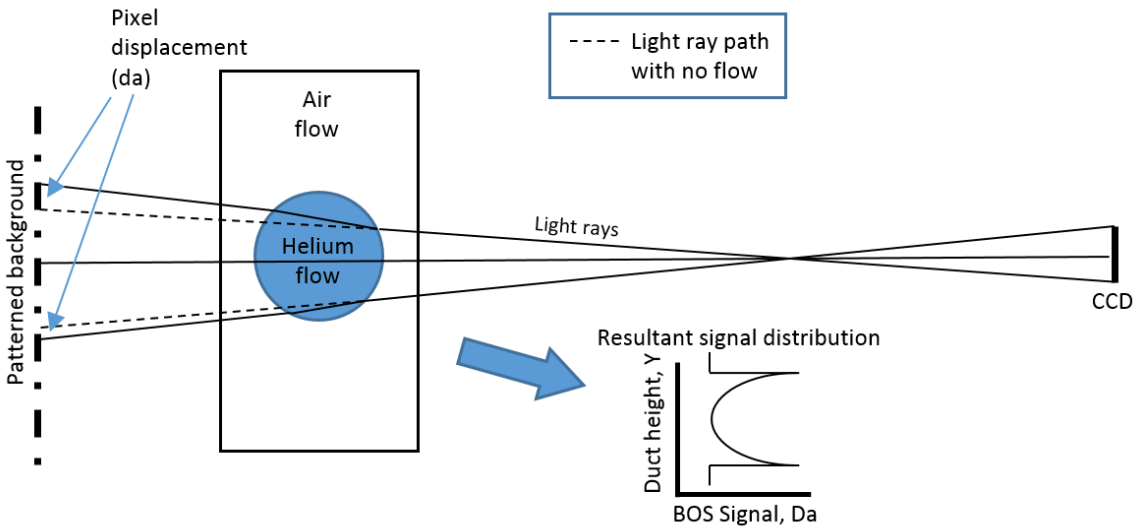

FIGURE 3.10: *Basic theory of BOS principles applied to measuring a light gas jet in surrounding co-flow.*

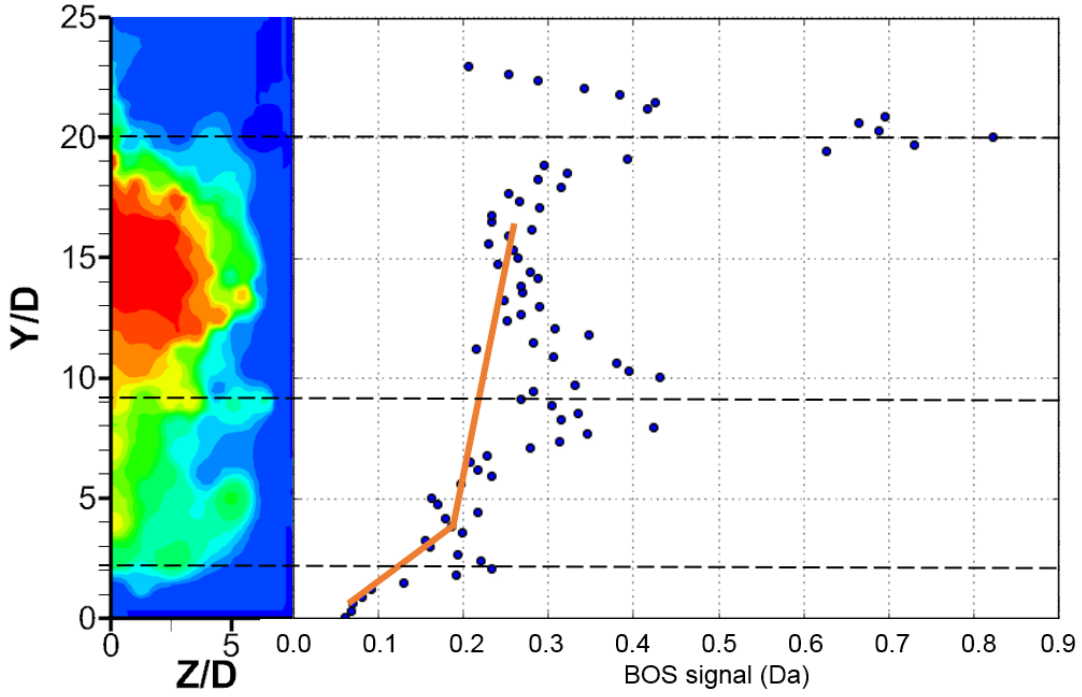

FIGURE 3.11: *Helium mole fraction contour compared to the BOS signal, Da, along the height of the duct. $X/D = 76.8$ The black dashed lines indicate where the local maxima match up to the contour plot. The orange line indicates the three regions where figures 3.12 and 3.13 are calculated from.*

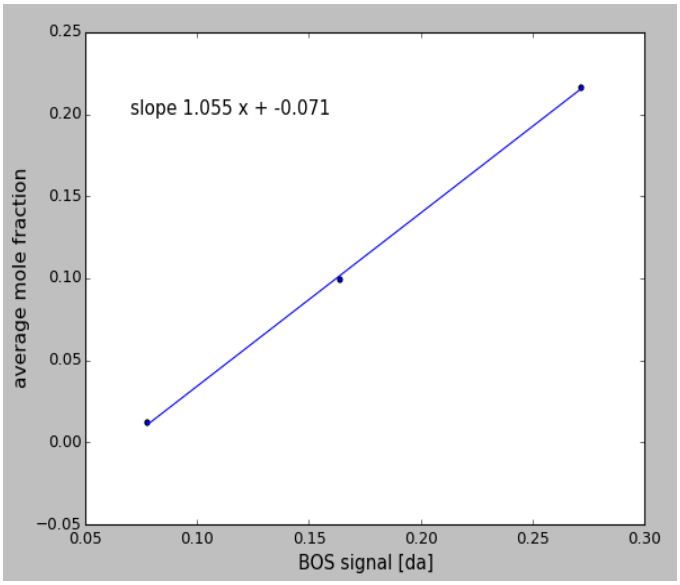

FIGURE 3.12: *Functional relationship exists between the helium mole fraction and BOS signal*

To determine this dependency, the shape of the helium jet must be constant in the y-direction, such that there is no diffraction due to curvature of the helium jet cross-section. From fig. 3.11, it can be seen that there are ranges where $d\left(da\right)/dy \approx 0$ corresponds to regions of the helium jet where the gradient of the helium mole fraction with respect to Y, is approximately zero. There are three of these regions from Y/D = (0-1.18), (3.24-4.71), (12.35-17.06). The average helium mole fraction within these ranges is extracted and plotted against the average BOS signal within these ranges in fig. 3.12. The correlation has only three points to build the relationship, however, it shows excellent linearity. The theory behind Schlieren states that the relationship between the BOS signal and the gradient of density along the light ray path is a constant, C (see eq. 3.2). The gradient of helium mole fraction can be related to the density gradient for constant pressure and temperature by eq. 3.3. Therefore, a linear relationship should exist between the BOS signal and gradient of helium mole fraction along the BOS LOS. The data for this relationship is plotted in fig. 3.13.

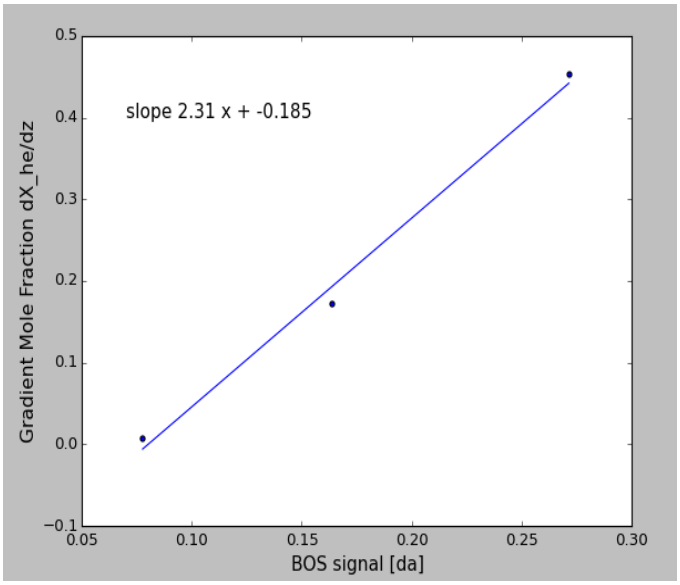

FIGURE 3.13: *Physical relationship between the helium mole fraction gradient along the BOS LOS and the BOS signal, da.*

$$Da = \frac{\partial \rho}{\partial z} C \tag{3.2}$$

$$\begin{aligned} \rho &= \frac{P}{RT}\left[\frac{MW_{he}}{MW_{air}} - 1\right]\chi_{he} + \frac{P}{RT}\frac{MW_{he}}{MW_{air}} \\ \frac{\partial \rho}{\partial z} &= \frac{P}{RT}\left[\frac{MW_{he}}{MW_{air}} - 1\right]\frac{\partial \chi_{he}}{\partial z} \end{aligned} \tag{3.3}$$

Figure 3.14 is an example of the time-averaged BOS results for the strut injector. In this image, shock waves and the helium jet are visible as highlighted by the labels in the figure. The shadowed boxes along the wall are screw holes in the acrylic windows. For the flush wall injector, they unfortunately are blocking the injector port. This was unavoidable due to the design of the flowpath.

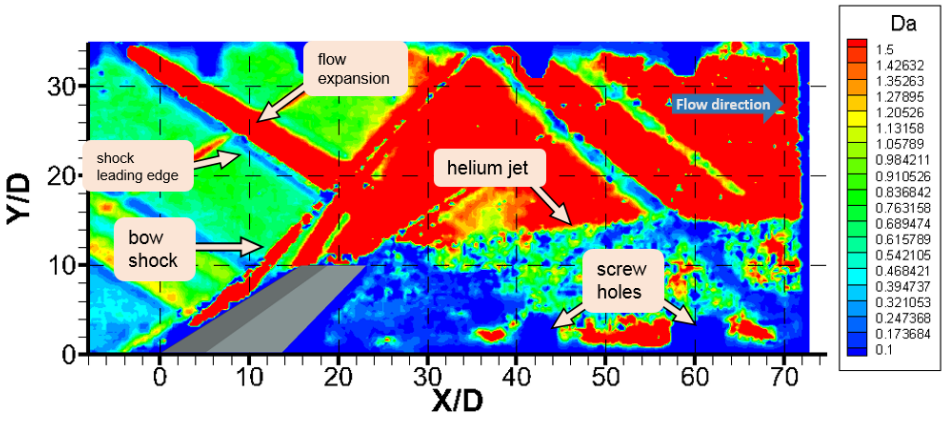

FIGURE 3.14: *Time-averaged BOS image of the strut injector with annotations of the features of the BOS image.*

Chapter 4

Strut Tip Injection and Mixing into a Supersonic Crossflow

The experiments outlined in chapter 3 are used to evaluate the mixing characteristics of a gaseous jet injected into a supersonic cross-flow from the tip of a strut. Where applicable the results are compared against the baseline case of a normal flush wall injector; in some cases outside literature is used to contrast the physics observed of the strut tip injector. This chapter will first examine the flow physics around the strut tip injector port using the CFD solution for configuration C3P1. Next, the helium jet penetration results are shown for both the strut injector and the flush wall injector. Helium mole fraction contours are compared between the strut and flush wall injectors, and finally the mixing efficiency and total pressure recovery are compared for the two injectors.

4.1 The localized flow around a Strut Tip Injector

In section 2.1.2, the case of a flush wall injector was discussed. Figure 2.2 shows a separation region upstream of the injector caused by the bow shock interacting with the boundary layer. This separation is highly three-dimensional as the bow shock wraps around the circular jet in a horseshoe-like pattern. Downstream of the injector is a region of separated low pressure, referred to as a wake region. The driving action of this pressure gradient generates vorticity oriented in the direction of the jet, which propagates downstream. [11, 92]

Figure 4.1 shows a contour of the normalized static pressure, P/P_∞, along a surface slice taken at the height of the strut from the CFD case, C3P1. This case was chosen as a representative case for the physics of this discussion because, with respect to the experimental strut injector, it has the closest dynamic pressure ratio and the same injector hole locations. The entire flow length is not shown so that the detail around the injector can be seen. The image suggests that the bow shock formed due to the injector jet is thin and narrow, and that any separation due to this bow shock is negligible relative to the injector port diameter. This is because there is no distinguishable increase in pressure along the wall upstream of the injector port. Figure 4.2 shows the pressure distribution extracted from fig. 4.1 at $Z/D = 0$ and $Y/D = 10$, which is the centerline of the flowpath at the height of the strut tip. The pressure rise from the bow shock off of the strut leading edge is evident, then the flow re-expands on the top surface of the strut. This can be seen in the Mach number contour in fig. 4.3, where there is a triangular shaped region between the bow shocks. In fig. 4.2, the pressure rise upstream of the injector is shown to be less than 1 diameter, meaning that the bow shock and the separation region are small with respect to the injector. This is in contrast to data of a

flush wall injector from Gruber et al., where the measured pressure rise along the wall for each dynamic pressure ratio was over $2.4D$. [50]

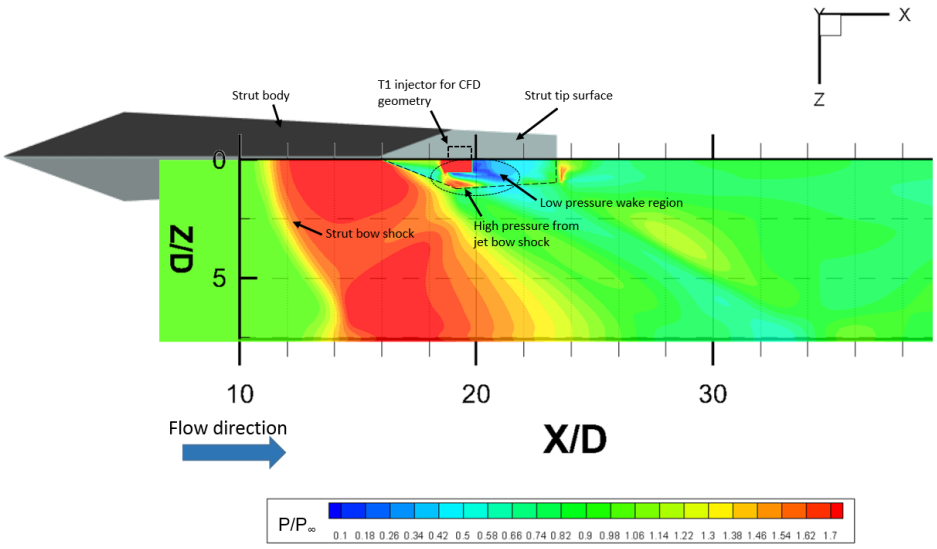

FIGURE 4.1: *Normalized static pressure contour for a spanwise plane at the height of the strut tip, $Y/D = 10.0$. The pressure distribution caused by the transverse jet is circled in the oval.*

Figure 4.4 is a time-averaged BOS image of the strut injector in supersonic cross-flow. The image shows the bow shock from the strut leading edge and the bow shock from the T1 injector jet. This BOS image also shows the wake region downstream of the injector. The helium jet is obscured in the wake region due to the low static pressure. When the pressure gradients smooth out, the helium jet becomes distinguishable.

Boundary layer separation is a function of the thickness of the boundary layer and strength of the adverse pressure gradient. The lack of a separation zone upstream of the injector port at the tip surface is due to two factors. First, the bow shock from the strut leading edge slows and turns the flow away from the helium jet so that the flow is more oblique with respect to the jet flow causing a weaker bow shock in front of the T1 helium jet, and hence a reduced pressure gradient where the shock interacts with the boundary layer. Second, the boundary layer along the top surface of the strut is relatively thin

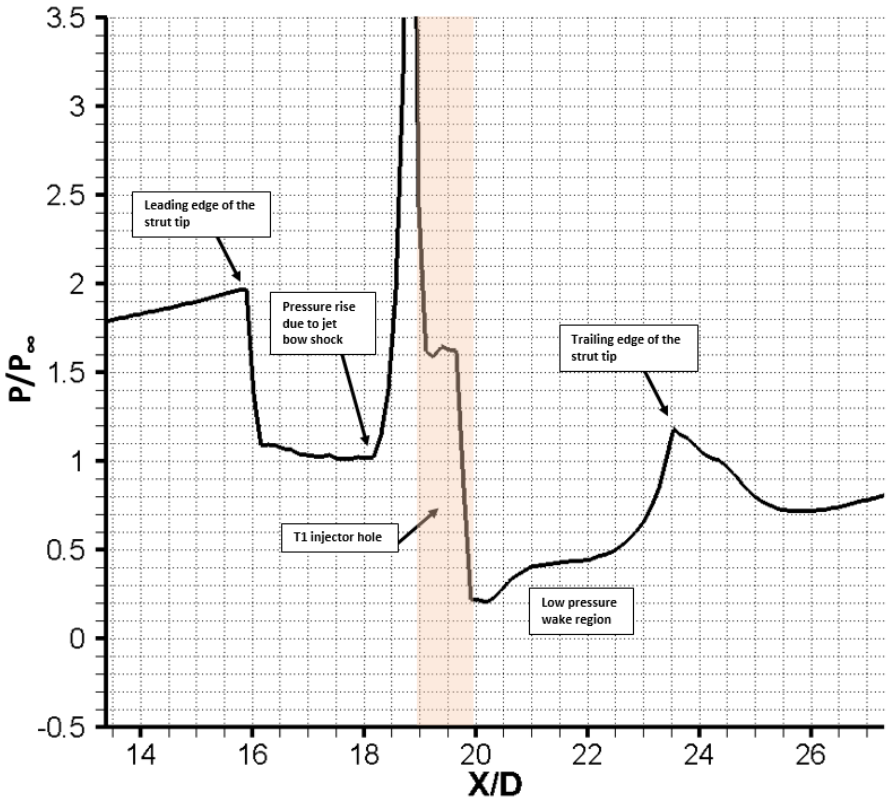

FIGURE 4.2: *P/P_o vs. X/D at $Z/D = 0$, $Y/D = 10$. This plot shows the expansion over the strut tip and the pressure rise upstream of the injector is less than $1D$.*

compared to the injector diameter, $\delta/D = 0.005$, because the development length along the strut tip wall is short.

The width of the strut tip relative to the T1 injector port diameter is $1.2D$. This is a small amount of surface area in comparison to a flush wall injector which has an essentially infinite surface to the sides of the injector port. The horseshoe bow shock which generates a region of high static pressure to the sides of the injector is significantly limited by the narrow tip width. The region of increased static pressure to the side of the injector port is consequently small and will have implications on the jet penetration and mixing, to be discussed further in subsequent sections within this chapter.

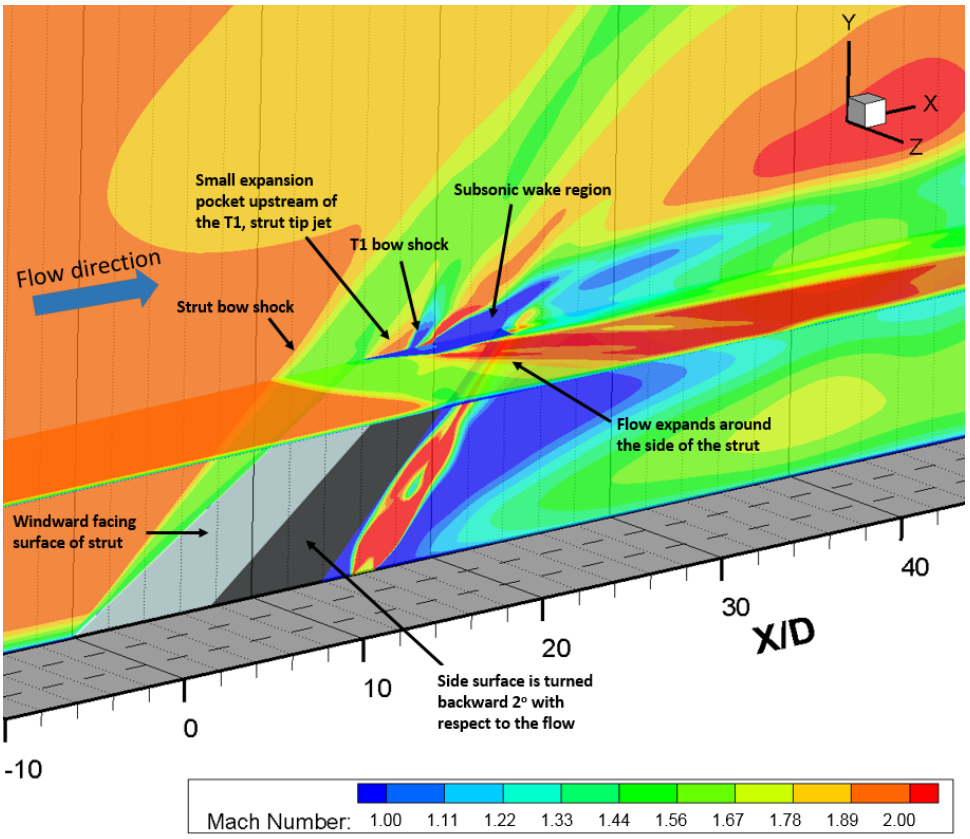

FIGURE 4.3: *Stream-wise contours of Mach number which intersect at the centerline of the strut tip. The shock and expansion waves due to the strut and the tip injector can be seen.*

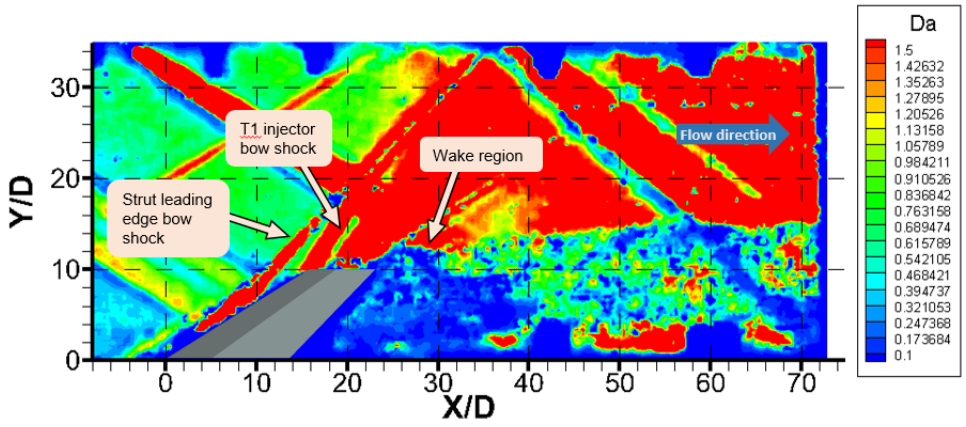

FIGURE 4.4: *Time-averaged BOS image of run S7.*

4.2 Jet Penetration from the Strut Tip Injector

The penetration results from the CFD and experiment both agree with the theory of Billig and Schetz, that the tip jet momentum is significantly dampened as compared to

a flush wall injector under the same conditions due to the thin boundary layer at the point of injection. The jet is immediately impacted by the high-energy flow increasing the angle of the jet Mach disk with respect to the freestream flow, so that the jet flow velocity is parallelized with the crossflow. [13] Evidence of this will be shown in this section, by estimating the distance from the injector exit to the center of the Mach disk, h_{Md}, from both CFD and experimental results. The jet penetration is further dampened compared to a wall injector due to the reduced strength of the counter-rotating vortices in the jet which promotes upward movement of the injected jet. [11, 92]

The jet penetration was extracted from the helium mole fraction contour plots of the CFD cases, shown in fig. 3.5. All data extraction was done using the Plot Digitizer software package. [60] The jet penetration, Y_p/D, which is measured from the upper boundary of the jet, is plotted in fig. 4.5 for these CFD cases C2P2, C3P2, and C4P2. In cases C2P2 and C4P2, the jet penetration is 138% of the strut height, despite the helium being injected from different locations. For reference, the active injector for configuration C2P2 is T1, and the active injector for configuration C4P2 is W1. The T1 and W1 injectors are combined in Case C3P2 where they have an improved penetration to 158% of the strut height. The jet penetration in case C3P2 shows that the tip injector acts to increase the effective height of the strut by an additive term of $2h_{Md}$, where h_{Md} is the distance from the injector exit to the center of the Mach disk. This is shown in fig. 4.5 by adding $2h_{Md}$ from the T1 injector to the helium penetration of C4P2, the penetration of C3P2 can be estimated, and is plotted as $C4P2 + h_{md}$ in the figure.

To determine if this principle can apply to other injector configurations, a study by Hollo et al. having two in line flush wall injectors, of the same diameter and Q, was examined. Figure 4.6a is a sketch of the experiment. [55] The penetration for a single injector, given the jet and free-stream conditions reported in the reference, was

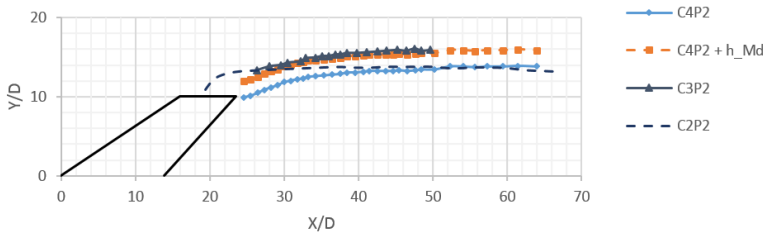

FIGURE 4.5: *Y_p/D extracted from the CFD.*

calculated using eq. 2.4. Then the height of the Mach disk for the forward injector was extracted from fig. 5a of the reference, which is a PLIF-derived mole fraction contour plot. The measured penetration was then also extracted from this figure. The results of this effort shows that the calculated penetration, and extracted measured penetration match well, and the comparison is shown in fig. 4.6b. Broadly this can be applied as the superposition of injectors by taking two times the Mach disk height of the upstream injector. This relation is most likely only valid if the injectors are close enough that they interact with one another; this cannot be properly verified by this study, however. Further studies would have to be done to determine the range of applicability of this relation. The ratio of effective jet backpressure to jet total pressure, P_{eb}/P_t, could be used to make the same prediction since the height of the Mach disk is proportional to this ratio. [13]

Moving on to the experimental results of this dissertation, fig. 4.7 shows the jet penetration, Y_p/D, measured from the time-averaged BOS images using the Plot Digitizer software; this is the same process that was used for the CFD. The top of the jet is considered as the penetration height of the jet which corresponds to the local maximum of d(Da)/dy. The source BOS images for the jet penetration results of fig. 4.7, are those shown in figures 4.8a and 4.8b. The overall jet penetration at the far measurement plane is 145% of the strut height. This is a significant gain in jet penetration over similar strut injectors in the literature. [57, 98, 99]

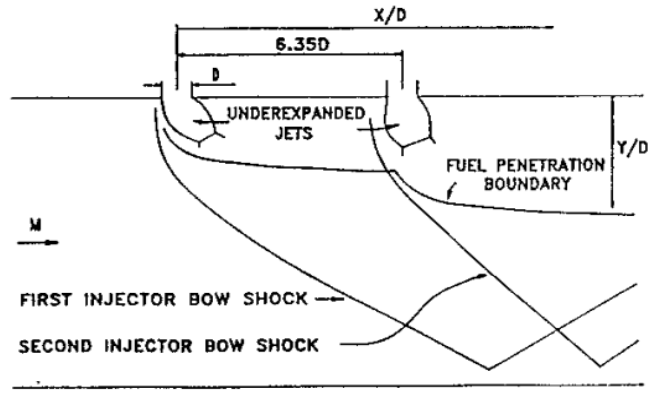

(A)

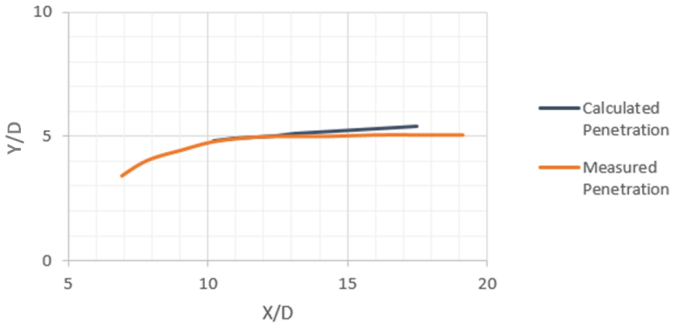

(B)

FIGURE 4.6: *A) Injector configuration schematic for study by Hollo et al. [55] ; and B) Y_p/D extracted from ref [55]. Adding $2H_{Md}$ to the penetration of the leading injector gives the penetration of the combination of injectors.*

Comparing the jet penetration of the strut with the flush wall injector reveals that the jet penetration from the strut is lower than the penetration from the flush wall injector when referencing the penetration to the point of origin, h_o. The jet penetration referenced to the point of origin, at the far measurement plane, is 32% greater for the flush wall injector than the strut, and at the near measurement plane the h_0^1 is 150% greater for the flush wall injector. These results show that the flush wall injector initially penetrates much further because the boundary layer is thicker. Both injectors are in the same flow conditions and as the helium moves downstream, the penetration rate become the same. These results are listed in table 4.1.

Correlations to model the jet penetration data are plotted by the solid curves in fig. 4.7. The basis for the correlation used to model the penetration for both the strut

and flush wall injector is eq. 2.4 from section 2.1.2, where this model is specific to a Mach 2 cross flow and a boundary layer thickness to injector diameter ratio,δ/D, of 1. This model is then weighted for effects due to the boundary layer and injection angle by eqs 4.1 and 4.2 from references [71] and [70], respectively. The height of the Mach disk is estimated from fig. 4.8a to be approximately $0.4D$ and the $2h_{Md}$ term is added. The adjusted correlation equation is given by eq. 4.3. This adjusted correlation fits well for the experimental results, especially in the far field, $20D$ from the point of injection.

$$\frac{y}{D} \propto \frac{\delta}{D}^{0.0574} \tag{4.1}$$

$$\frac{y}{D} \propto sin\,(\theta)^{0.0574} \tag{4.2}$$

$$\frac{y}{D \cdot Q} = 1.23 \left(\frac{x}{D \cdot Q}\right)^{0.344} \left(\frac{\delta}{D}\right)^{0.0574} sin\,(\theta)^{0.844} + 2 * h_{Md} \tag{4.3}$$

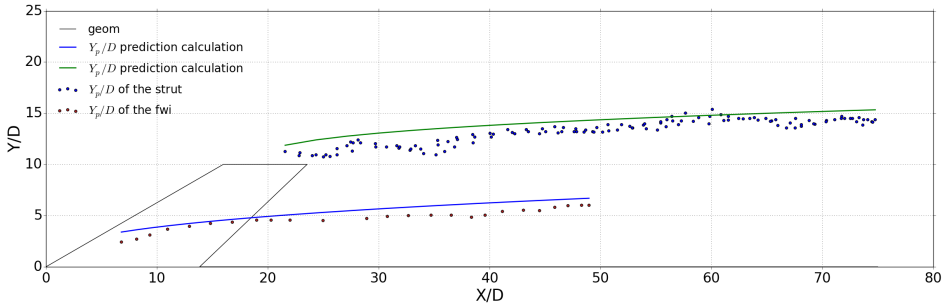

FIGURE 4.7: *Experimental Y_p/D for the strut and flush wall injectors. The reference injector diameters are 0.1 and 0.155, respectively.*

The lack of boundary layer at the strut tip causes the tip jet to immediately be turned over by the high-momentum airflow. This causes the overall helium penetration from the strut tip, h_o, to be much less than for the flush wall injector. The combination of the strut injector port and wall injector port at the base of the strut act as though

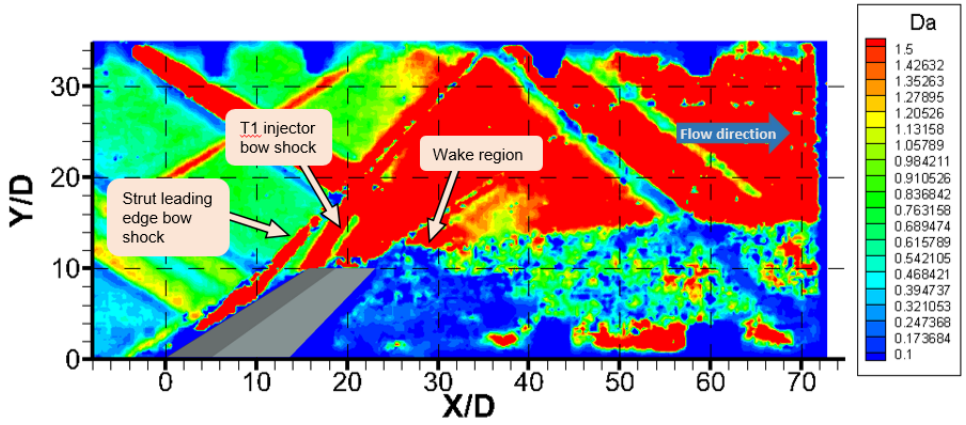

(A) Time-averaged BOS image

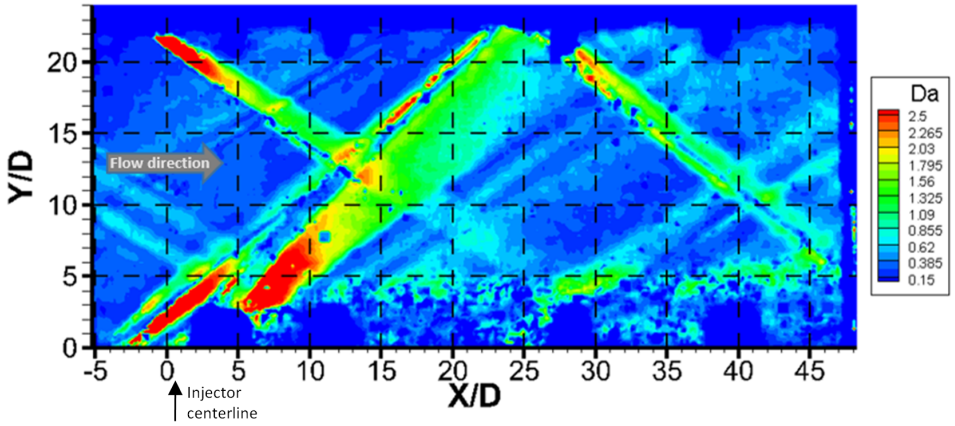

(B) Time-averaged BOS image

FIGURE 4.8: *A) Strut injector; B) Flush wall injector (FWI).*

TABLE 4.1: *Strut injector and FWI jet penetration results*

Injector	Strut	FWI
Q_{nom}	1.76	1.76
δ/D	0.005	0.77
θ	54	90
h_o^1	$1.71D$	$4.57D$
h_o^2	$4.22D$	$6.03D$
h_{max}	$4.86D$	$6.03D$

they are in-line injectors. An additive relationship for the overall jet penetration of $2h_{Md}$ is used to match an empirical formula to the experimental results. This is corroborated by the CFD results, and by the results of Hollo et al.

4.3 Cross Section contours of Helium Mole Fraction

The cross section contours of helium mole fraction are produced from the GSAS mole fraction measurements, which are detailed in appendix A. Figure 4.9 shows the near and far measurement planes of the strut injector in supersonic crossflow. A cross-sectional projection of the strut is shown for reference as well as the location of each fuel injector. The change in shape of the contours from the near to far planes shows that there is a large movement of helium upward. As the jet mixes traveling downstream, the distribution of helium coalesces into a central circular jet. The sweep angles of the strut are designed to promote this upward movement. In addition the flow in the region affected by the strut and helium injection is accelerating as the jet mixes downstream. This is shown by the measured mass-averaged Mach number for this region of the flow, which increases from 1.6 to 1.8 between the measurement planes. As this occurs, the helium jet cross section must contract to satisfy conservation of mass. This causes the helium jet to be stretched axially as it mixes.

Figure 4.10 shows two helium mole fraction contour maps for the flush wall injector in supersonic crossflow. The left side contour is at the near measurement plane and the right side contour is the far measurement plane. The jet cross-sectional area stays relatively constant over the axial range. However, the jet mixes well because the mole fraction contour in the center of the jet goes from 0.48 at the near measurement plane to 0.275 at the far measurement plane. At X/D = 49.5 the maximum mole fraction is

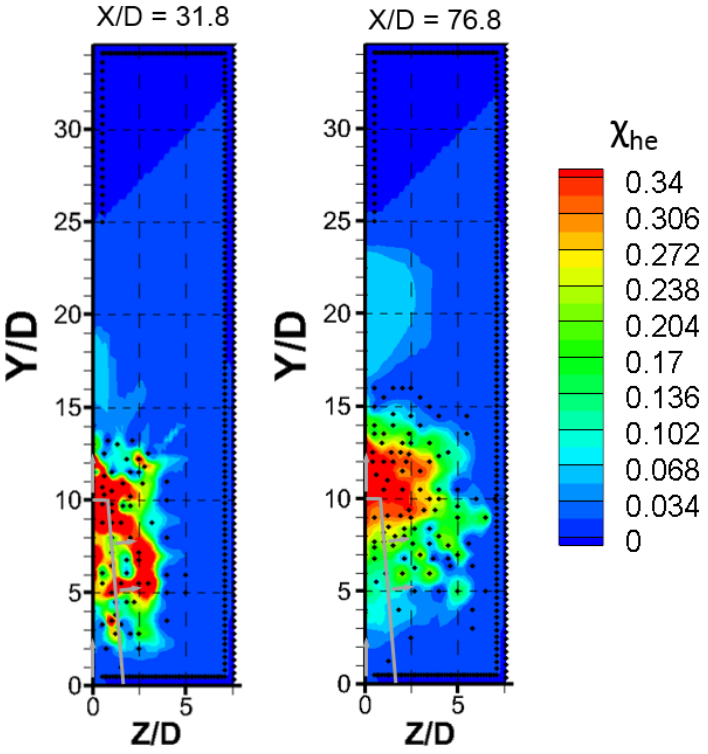

FIGURE 4.9: *Contour maps of the cross-sectional helium mole fraction distribution for the strut injector in supersonic cross-flow. The black dots are locations of each measurment point.*

less than the stoichiometric mixture, $\chi_{st} = 0.28$, indicating that the mixing efficiency is 100%. This will be corroborated by the mixing efficiency calculations from the gas sampling data in the following section.

From these contour plots it is evident that the flush wall injector achieves a higher level of mixing than the strut injector. In the next section, the rate of mixing for each injector will be discussed. The strut injector translates the fuel plume upward from the wall and out of the boundary layer, whereas the plume from the flush wall injector stays along the wall. There is a trade-off between the two injectors, increased mixing or increased penetration.

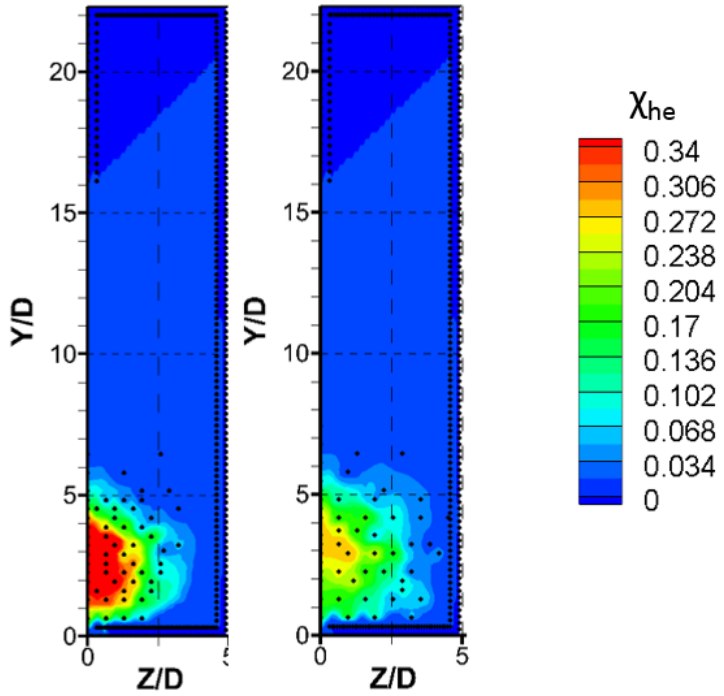

FIGURE 4.10: *Contour maps of the cross-sectional helium mole fraction distribution for the flush wall injector in supersonic crossflow. (Left) X/D = 20.5 and (Right) X/D = 49.5*

4.4 Mixing Efficiency

The data given by table 4.2 shows the mixing results for the strut injector and flush wall injector. The FWI achieves a higher mixing efficiency in a shorter relative distance, however the FWI also has a lower equivalence ratio, where the equivalence ratio is calculated for the same airflow for each injector. The rate of change of the mixing efficiency, referred to as the mixing rate, $\frac{\partial \eta_m}{\partial X}$, is consistent between the two injectors. The reason that the FWI has a slightly lower mixing rate than the strut injector, is because the FWI reaches a fully mixed state before the far measurement plane at $X = 49.5D$. Therefore, the principle factors affecting the difference in mixing between these two injectors must be occurring at the point of injection, due to (1) the lower equivalence ratio of the FWI and (2) the strut injector entrains less air into the helium jet at the initial point of injection.

For the first point, there is less helium being introduced by the FWI, and therefore the mixing efficiency will be greater. A competing factor is that the strut injector has a distributed injection of helium along the strut body which increases the contact area between helium and air, whereas the FWI injects all of the fuel through a single injection orifice. For the second point, the FWI has a greater transverse pressure gradient between the injector bow shock and the wake region than the strut injector has at any of its injector orifices. Therefore, for the FWI, more air is initially pulled into the jet as the air is forced around the injector hole. That air and helium is then trapped together in the jet and mixes as it travels downstream. A study by Gruber et al. of Mie scattering around two different flush wall injector shapes showed that the stronger bow shock entrained more air into the helium jet. [48]

TABLE 4.2: *Mixing efficiency for the strut and flush wall injectors in supersonic cross-flow*

	Strut		FWI	
$X/D =$	31.8	76.8	20.5	49.5
η_m	0.735	0.908	0.857	1.000
ϕ	0.172	0.178	0.133	0.156
$\frac{\partial \eta_m}{\partial X}$	0.038		0.032	

Future experiments will be necessary to determine which injector has the better mixing. This is due to the complexity of the strut injector, and the difference in fuel equivalence ratios between the strut injector and FWI. The mixing efficiency at the two measurement planes show that in the far field, the mixing rate is the same for both injectors.

4.5 Summary

Injecting fuel from the tip of a strut has been shown through these results to have potential for reducing the height of a strut fuel injector. The jet penetration from the strut injector was 145% of the strut height measured from the wall. This result represents a substantial increase in fuel penetration from a strut into a supersonic cross stream. The implication of this for future combustor designs is that the height of the strut from the combustor wall can be reduced, thereby limiting the internal engine drag and thermal load. Future experimentation of a complete combustor design would be needed to see how the struts behave when integrated into a complete engine configuration.

Chapter 5

Simulation of Dual-mode Scramjet Mixing in a Backpressured Flowpath

A dual-mode scramjet combustor experiences a wide range of flow conditions due to the combustion driven pressure rise. This pressure rise generates shocks and varying portions of supersonic and subsonic flow where the fuel is injected and mixed. Results from an experimental investigation of the mixing characteristics of a strut tip injector in crossflow conditions simulating a dual-mode scramjet are analyzed here. A more detailed discussion of the motivation for these experiments was discussed in section 1.5.2. The flowpath exit is open to the atmosphere, resulting in a constant exit pressure, that is used to backpressure the flowpath by reducing the nozzle plenum pressure to generate a shock train in the flowpath. This methodology was explained in section 3.7. In this chapter, the results are shown in comparison to the common flush wall injector, as was done in chapter 4.

5.1 Inviscid Flow Structures in the Helium Mixing Jet

Inviscid flow phenomena, such as shock waves and vorticies, are implicitly present in a supersonic mixing environment and often interact. These features, in part, affect the mixing characteristics that shall be discussed in the subsequent sections, and so the processes that these features impose on the mixing must be understood. Observing these features visually and matching them with quantified mixing information will provide a holistic understanding of the injector operation.

Baroclinic vorticity is generated when a density gradient is crossed by a pressure gradient, $\nabla P \times \nabla \rho$, and the resultant vorticity is orthogonal to the two gradients. [65] In a supersonic combustor, if the fuel has a differing density than air, baroclinic vorticity will occur when shock waves intersect boundaries of fuel and air. The vorticity that is generated aids in increasing the contact area between the fuel and air and hence aiding in the mixing.

For each of the experimental flow cases, supersonic, sonic, and subsonic, fig. 5.1 shows a three-dimensional view of the flowfield constructed from the spanwise BOS images and the crossflow helium mole fraction contours. Note that the spanwise plane is in the X-Y axes, and the crossflow planes are in the Z-Y axes. From these plots the flow structures such as shock waves and vorticies can be identified, and the effects on the helium jet shape and mixing can be analyzed. The BOS contour represents the integrated density gradient across the Z-axis, and the crossflow contours show the shape and gradients of the helium jet cross section.

The shocks relevant for this discussion are labeled A, B, and C in fig. 5.1. Shock A is a weak wave emanating from a step in the wall, shock B is the bow shock from the strut, and shock C is the reflected bow shock from the top wall. In each of the cases,

shock B is prominent and shock C crosses through the helium plume roughly halfway between the two measurement planes. Black lines are drawn through the shock waves to highlight them. For reference, the wave angle of shocks A and B are listed in table 5.1.

TABLE 5.1: *Shock angles*

Run	S17 Supersonic	R14 Supersonic	S18 Supersonic	R15 Supersonic
Shock A	35.9	33.6	32.8	34.2
Shock B	47.2	38.2	47.6	49.6

Locally, these shocks have differing effects depending on the location with respect to the helium jet, the strength of the shock, and the flow speed. In each of the experimental cases the spanwise view of the upper boundary of jet penetration seems to be smooth through the interaction with shock A, implying that the flow direction does not turn appreciably through this shock. Further downstream, where reflected shock C intersects the jet, the flow turning makes a noticeable impact on the jet penetration, which will be discussed further in section 5.4. When shock A, intersects the helium jet, there is a sharp density gradient in the z- and y-directions because boundaries between air and helium have not had time to diffuse into one another. This can be seen in the BOS images of fig. 5.2 as a strong band in the BOS signal intensity, Da. Indicated by an arrow, the high Da band forms off of the trailing edge of the strut and corresponds to an indent in the helium jet cross section. This shape represents air being stirred into the helium jet by counter-rotating vorticies from the strut injector, thereby increasing the surface area of helium and air. Since helium-air gradients are related to Da, it shows in the BOS image as a band. This structure is difficult to identify in the supersonic case because the amount of air pulled into the jet at this X/D is small, i.e., the impact of the vorticity is stretched downstream due to the higher flow velocity; it is more distinct in

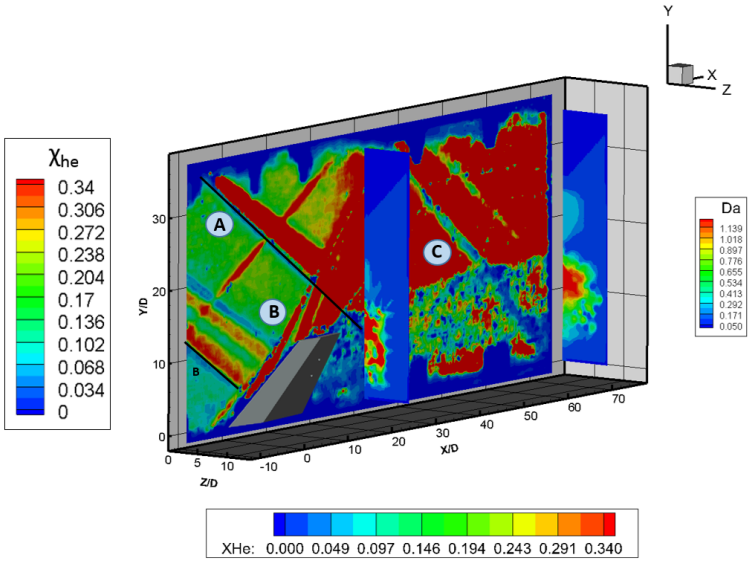

(A) Supersonic

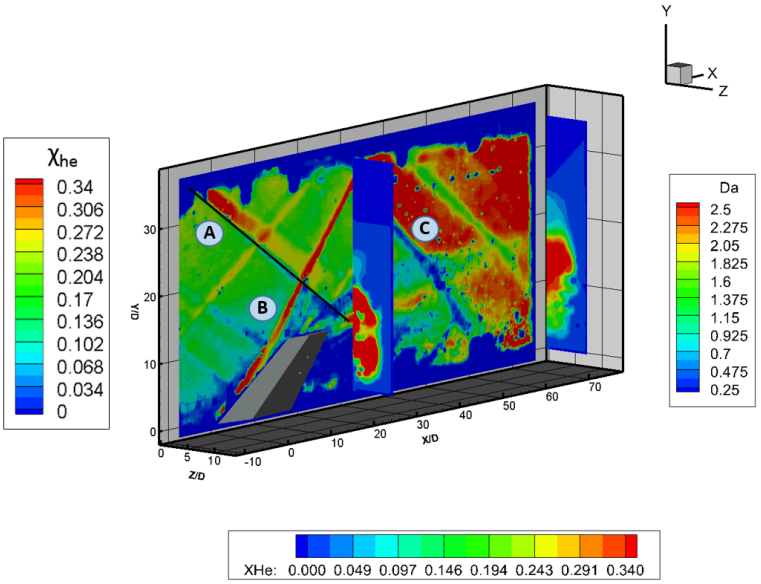

(B) Sonic

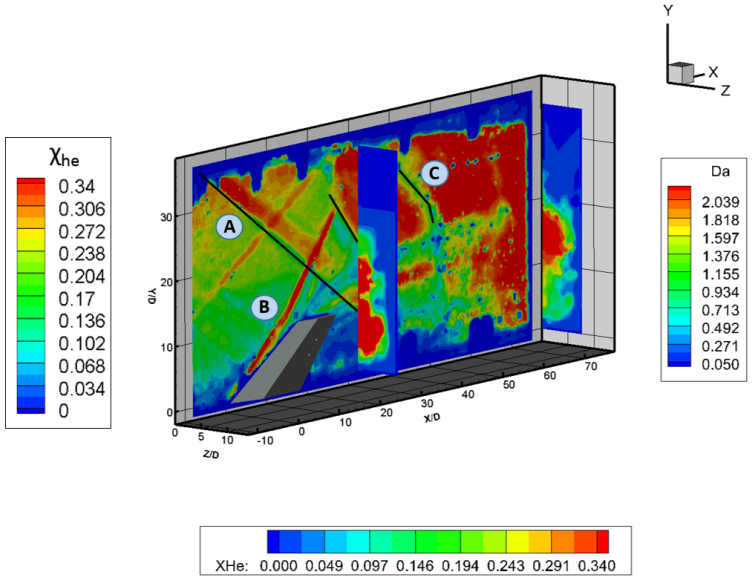

(C) Subsonic

FIGURE 5.1: *Three-dimensional constructed views of BOS and helium concentration data for the strut injector in each flow condition.*

the sonic and subsonic cases.

When shock A strikes the helium-air boundary the observed Da signal intensity increases, and the band thickens rapidly, then continues to spread as the jet travels downstream. The thickening of this band where the shock crosses is due to baroclinic vorticity generated by the interaction between the shock wave and the density gradient. The baroclinic vortices act to increase the amount of air pulled into the jet, increasing the surface area of helium and air, thereby causing a representative increase in the thickness of the band. Further downstream where shock D intersects the jet, it is more difficult to distinguish the affect of baroclinic vorticity on the jet mixing due to poor signal differentiation with the surrounding flow.

The shock and vorticy interactions with the mixing jet will be used subsequently through the chapter to explain characteristics in the mixing and jet penetration. To get a complete story of the flowfield, the viscous mixing layer structures will be visualized as well. The compressibility of the flow affects the mixing shear layer, and the characteristic structures that form in the mixing layer.

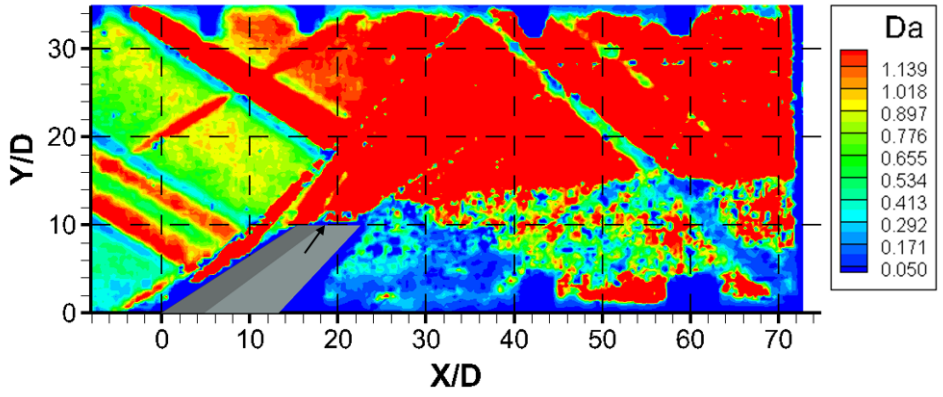

(A) *Supersonic*

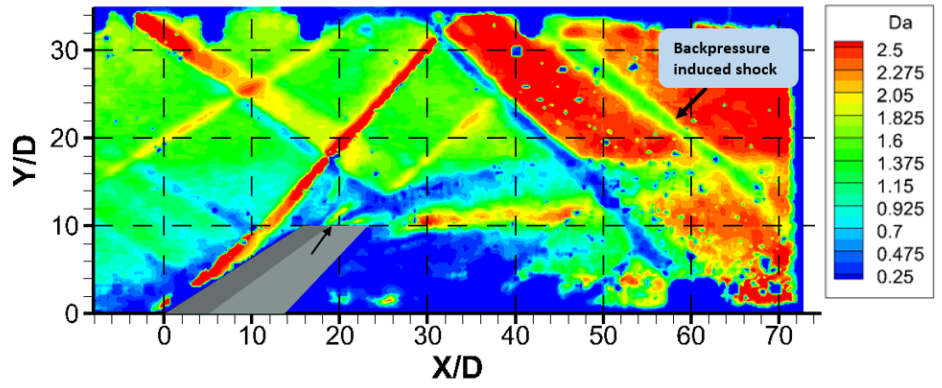

(B) *Sonic*

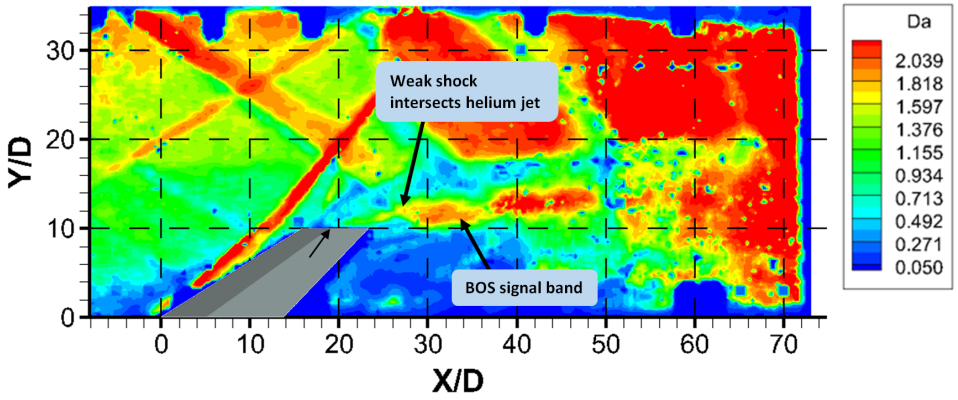

(C) *Subsonic*

FIGURE 5.2: *Time-averaged BOS images for each experimental case of the strut injector. The injector port is indicated by the arrow.*

5.2 Large-Scale Coherent Structures

The large-scale coherent structures, characteristic of a mixing layer, are rolling spanwise vortices, which are generated by shear along the interface surface of the two fluid streams. Refer to section 2.1.1 for background on the physics and historical research of coherent structures in mixing layers. The large-scale coherent structures, within the mixing layer, affect the fuel-air mixing because these structures govern the contact area for fuel and air molecules to diffuse and react. The size and organization of the coherent structures are affected by the compressibility of the mixing layer, which is indicated by the convective Mach number, and defined by eq. 2.3.

To resolve the large-scale structures, the instantaneous image pairs which comprise the time-averaged BOS images are analyzed for the flush wall injector only. The non-backpressured flows and all of the strut injector runs had poor resolution of the mixing layer structures. This is due to the increased pressure gradients caused by shock and expansion waves from the wall and strut which mask the helium-air boundaries. The figures of 5.3 show the mixing layer structures for the flush wall injector into supersonic flow and subsonic flow. In these figures the top is image A and the bottom is image B, flow is left to right, and the front edge of the injector port is at $X/D = 0$. The conditions for each of these runs is given in table 5.2. The instantaneous snapshot pairs, labeled A and B, have a $25\mu s$ time delay, Δt, between them, each has an exposure time of $2.5\mu s$, and the frame rate, or number of image pairs per second, is 25 hz. The camera was set up to take images in 1-second intervals and was triggered by the control system at 0.2 hz.

Figure 5.3b shows an image pair for run R5a, where the normal shock train due to the backpressure is upstream of the injector and out of the field of view, such that the

TABLE 5.2: *Experimental conditions for the instantaneous BOS image pairs*

Run	R4 Supersonic	R5a Subsonic w/o shock	R5b Subsonic w/ shock
$P_{t,he}$	125.5	126.3	121.6
$P_{t,air}$	46.7	31.6	31.9
$T_{t,he}$	307	307	308
$T_{t,air}$	283	283	282
Q	3.31	4.63	4.43
M_c	0.590	0.283	0.287

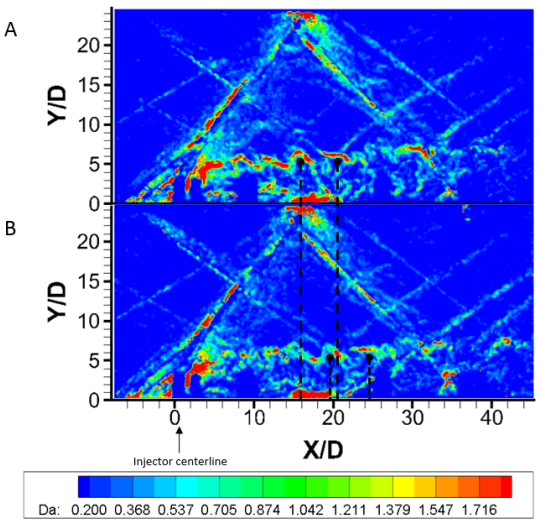

(A) *Run R4*

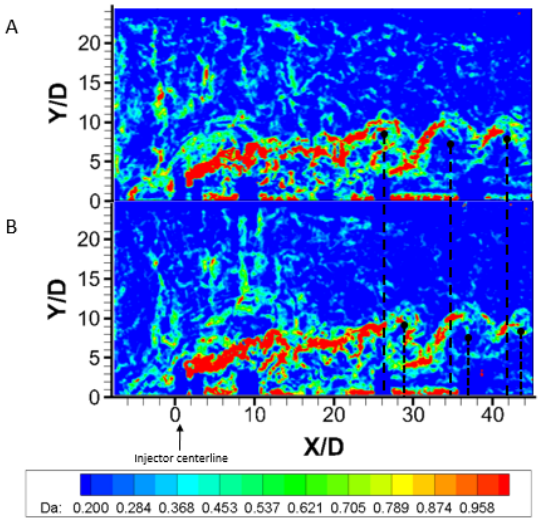

(B) *Run R5a*

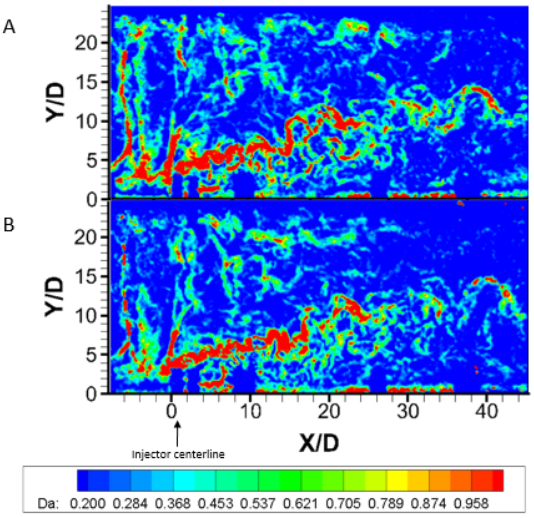

(C) *Run R5b*

FIGURE 5.3: *Instantaneous BOS image pairs showing the mixing layer structure of sonic transverse helium injection with a standing normal shock at the point of injection.*

flow at $X/D = 0$ is fully subsonic. In figs. 5.3a and 5.3b, the centers of the rollers are marked with the filled circle. The dashed lines illustrate the downstream movement of these structures from image A to B over Δt. The convective velocity of these structures was calculated with eqs. 5.1 and 5.2. This methodology was used by Gruber and Nejad to calculate the convection velocity of coherent structures in the near field of sonic wall injection into a Mach 2 cross-stream. [49]

In fig. 5.3 run R4 has a much thinner mixing layer with smaller and less distinct structures, whereas run R5a has very clear developed coherent structures. This corresponds to the known physics, that as compressibility increases the size and organization of the structures decreases. To calculate the convective Mach number from the measured convective velocity, eq. 2.3 is used, where the speed of sound for air and helium are used for the denominator. The convective Mach number for run R4 and R5a is 0.590 and 0.283, respectively. Clemens and Mungal reported that a convective Mach number of 0.50 is a rough transitional point for the rollers from an organized two-dimensionality to a more unorganized three-dimensional behavior. [27]

$$U_c = \frac{\Delta r}{\Delta t} \tag{5.1}$$

$$\Delta r = \sqrt{(x_2 - x_1)^2 + (y_2 - y_1)^2} \tag{5.2}$$

Figure 5.3c is an instantaneous BOS image pair of experimental run R5b, which occurred during a period of run R5. It is an interesting case because the air pressure and helium pressure were such that the initial normal shock, due to the backpressure, stabilized upstream of the injector with a secondary normal shock directly on the injector. Downstream of $X/D = 25$ the two-dimensional organization of the coherent structures

that was seen in fig. 5.3b is disrupted by the presence of the shocks on the injector. This unsteady behavior is being driven by the interaction of the helium jet and shock in the near field. The turbulent energy generated by this interaction propagates downstream causing the large-scale coherent structures of the mixing layer to disorganize relative to a mixing layer with the same convective Mach number without a shock wave present. It cannot be determined how long the shock stayed in this location because it had moved upstream in between capture periods of the BOS camera. Figure 5.4 is a sequence of images taken over 0.2 seconds, and the shock structure is stable in time relative to the residence time of the free-stream air in the flowpath, which is 0.8 ms.

The instantaneous BOS images have been used to visualize the coherent structures in the mixing layer under different backpressured flow conditions. The observed organization of the coherent structures in the mixing layer agrees with the documented literature on mixing layers. As the compressibility increases, the size of the large-scale coherent structures is reduced. In section 5.3 the effect of this behavior on the mixing will be discussed. While compressibility affects the coherent structures in the mixing layer, upstream turbulence entering the mixing layer can also break up the large scale coherent structures, such as was the case of run R5b. This will be further discussed in section 5.5.

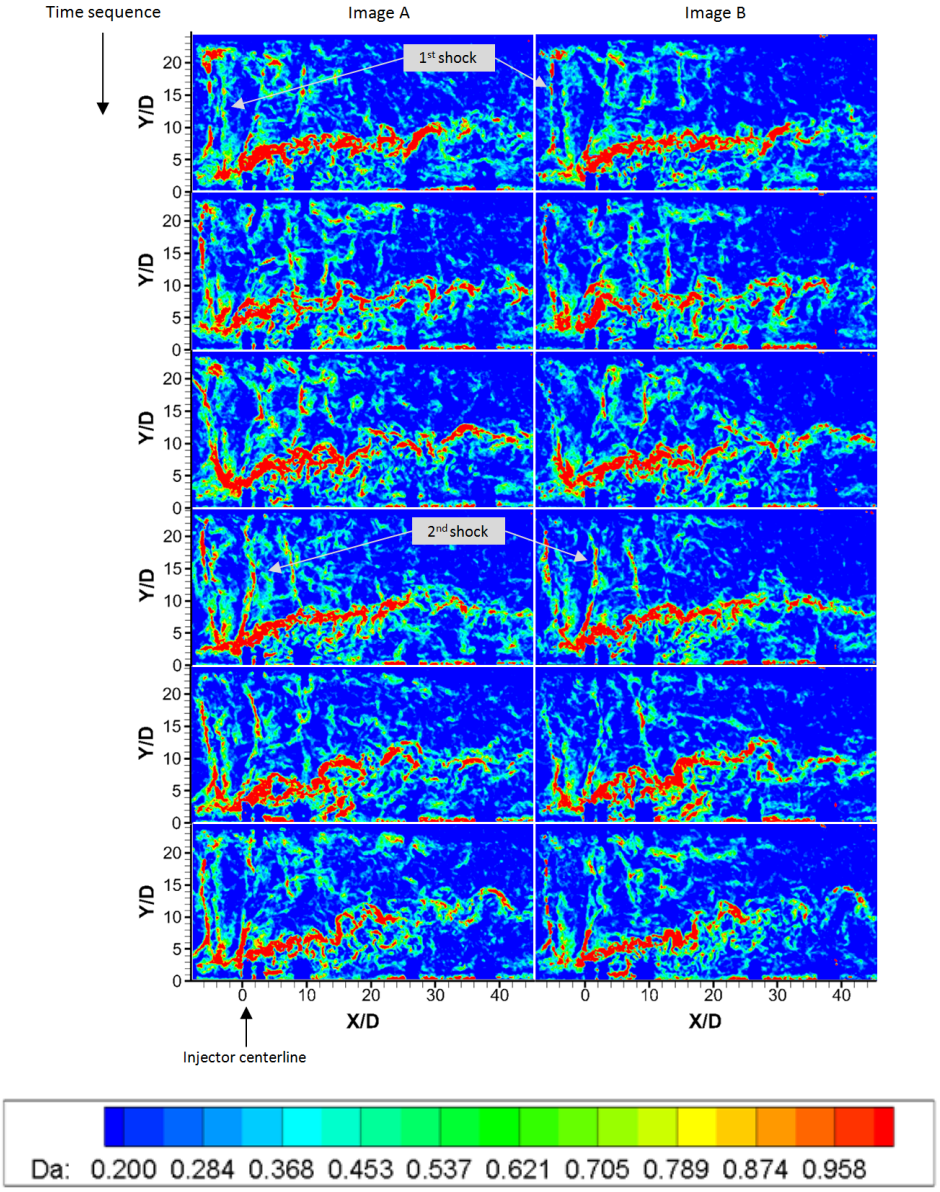

FIGURE 5.4: *Sequence of BOS instantaneous images showing the mixing layer structure of sonic transverse helium injection with a standing normal shock at the point of injection.*

5.3 One-Dimensional Mixing Characteristics

Now that a visualization of the structures in the mixing flowfield has been established, the quantified one-dimensional mixing characteristics will be discussed. The mixing efficiency and mass-averaged Mach number were calculated from the GSAS and Pitot pressure measurements for each experimental case. They are listed in tables 5.3 and

5.4, for the strut and flush wall injector, respectively. For this discussion the Mach number refers to the measured mass-averaged Mach number, measured over the helium jet region of the flow. Figure 5.5 shows the mixing efficiency vs. X/D, where the mean uncertainty for the mixing efficiency measurements is $+/-0.04$. The mixing rates between the strut injector and flush wall injector are approximately the same for each flow regime, meaning that the mixing in the far field is independent of how the fuel is injected. To reiterate, both measurement planes are in the far field relative to each injector. This result is consistent with the reported literature, discussed in section 2.4.

Looking at fig. 5.5 the mixing rate decreases as the flow transitions from supersonic to subsonic. These results were observed in the BOS images of section 5.2, where the large scale coherent structures for the subsonic flow were more organized into rolling waves. As the air flow increased in Mach number, and therefore the mixing layer increased in convective Mach number, these structures became more disorganized corresponding to an increase in the measured mixing rate. The general conclusions of existing literature on mixing layers agrees with these results.

Numerous studies have been reported in the literature to quantify the dependence of mixing rate within the mixing layer. [28, 35, 53, 62] In 1999, Wantanabe and Mungal found that the increased turbulent disorder due to either increased Reynolds number, compressibility, boundary layer trip, or other factors increases the mixing rate within the mixing layer. Therefore, a definite trend is difficult to develop because models, or measures, of the turbulence in these highly three-dimensional flows is necessary. [103]

It has been shown by both the BOS images and the mixing efficiency measurements that the turbulence of the mixing jet is a critical parameter driving the mixing. The mixing rates in the far field for both the strut injector and the flush wall injector are

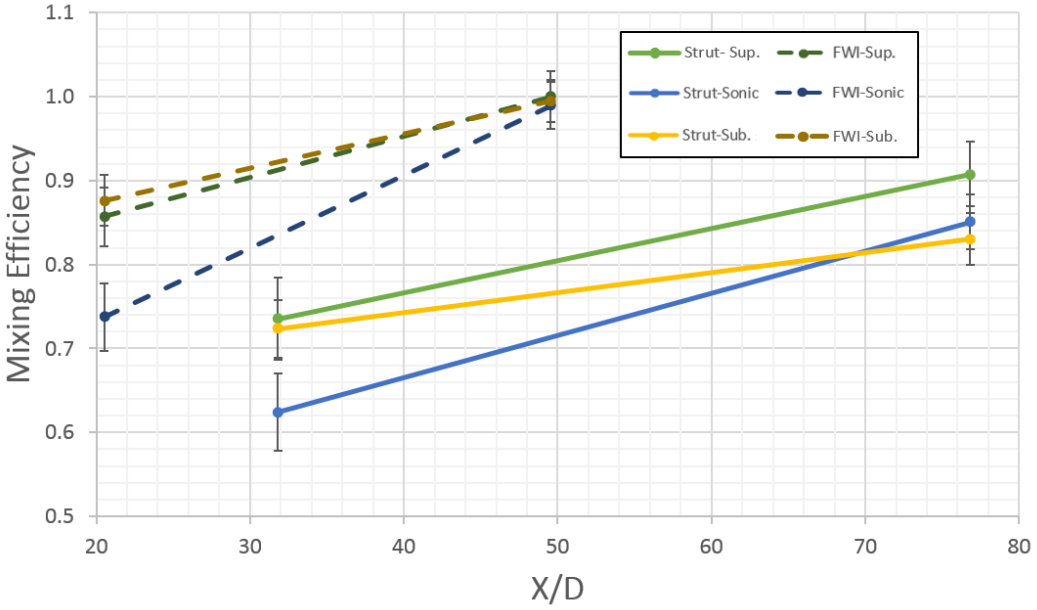

FIGURE 5.5: *Mixing efficiency vs. X/D for the strut and flush wall injector (FWI).*

TABLE 5.3: *One-dimensionalized mixing characteristics of the strut injector*

	Supersonic		Sonic		Subsonic	
M_{ave}	1.75		1.09		0.816	
$\frac{\partial \eta_m}{\partial X}$	0.038		0.050		0.024	
ϕ	0.176		0.366		0.575	
X/D	31.8	76.8	31.8	76.8	31.8	76.8
η_m	0.735	0.908	0.624	0.851	0.723	0.830

TABLE 5.4: *One-dimensionalized mixing characteristics of the flush wall injector*

	Supersonic		Sonic		Subsonic	
M_{ave}	1.74		1.06		0.709	
$\frac{\partial \eta_m}{\partial X}$	0.032		0.056		0.026	
ϕ	0.145		0.303		0.465	
X/D	20.5	49.5	20.5	49.5	20.5	49.5
η_m	0.857	1.000	0.737	0.939	0.876	0.995

similar. These observations in the data are consistent with the previously reported literature. The flush wall injector has a higher overall mixing efficiency than the strut injector.

5.4 Normalized Jet Penetration

Similar to the efficiency characteristics, the jet penetration is also affected by both the inviscid and viscous flow physics. In section 4.2, it was shown that the jet penetration, Y_p/D, was principally dependent on the dynamic pressure ratio, Q, and that the boundary layer thickness, δ/D, had a secondary effect. The proportionality of Y_p/D to Q is given by eq. 5.3, and is a result of the best normalization factor which collapsed the data from each experiment with differing dynamic pressure ratios. In order to adjust the pressure ratio across the flowpath, the nozzle plenum pressure was reduced, thereby using the ambient pressure as a backpressure. With the fuel pressure held constant for every experiment, the jet to freestream dynamic pressure ratio, Q, increases with the decreasing air plenum pressure, $P_{t,air}$. The penetration data was normalized by the dynamic pressure so that the differences due to compressibility, shock locations, and boundary layer can be identified.

$$\frac{Y_p}{D} \propto Q^{1/3} \tag{5.3}$$

Figure 5.6 shows the normalized jet penetration for the strut and flush wall injector, for supersonic flow where P/P_{ref} is unity, sonic flow where M_{ave} is approximately unity, and subsonic flow where the initial normal shock is upstream of the injector. The normalization factor, C_q, is given by eq. 5.4, where $Q_{nom} = 3.77$. The uncertainty in

Y/D is, $\mu Y/D = 0.05/D$. The figure shows that for the strut injector, the normalization factor, C_q, collapses Y_p/D for each flow condition up to roughly $30D$'s downstream from the point of injection. At that location the Y_p/D for the sonic flow flattens out and even decreases slightly. This happens to coincide with the reflected bow shock off of the top wall, which is causing the flow to turn downward through the oblique shock. For the supersonic case the jet is contacted by the reflected shock at $60D$. The correlation of these data shows that the jet penetration from the strut tip is strongly dependent on Q, and that the relationship of eq. 5.3 models this dependency. This relationship between Y_p/D and Q is different from the relationship in eq. 4.3 which was used to fit the jet penetration curve over the axial distance. That correlation equation was adapted from references in the literature, while the normalization equation was developed from the experimental data of this study.

$$C_q = \left(\frac{Q_{nom}}{Q} \right)^{1/3} \tag{5.4}$$

For the flush wall injector the normalization collapses the data for the supersonic and sonic cases, however, the subsonic case does not fall into alignment. There are two factors that could be causing the penetration to be high for the subsonic case; it could be the static pressure ratio of the helium jet to air, or it could be that the boundary layer is weakened and or inflated. The static pressure ratio, P_j/P_i, is known to enhance penetration as it approaches unity. [13] However, for each case, the jet is highly underexpanded, and P_j/P_i is further from unity than the supersonic flow. Therefore, the boundary layer must be thickened and weakened by the upstream shock waves As the ratio of boundary layer thickness to jet diameter, δ/D, increases, the jet is able to

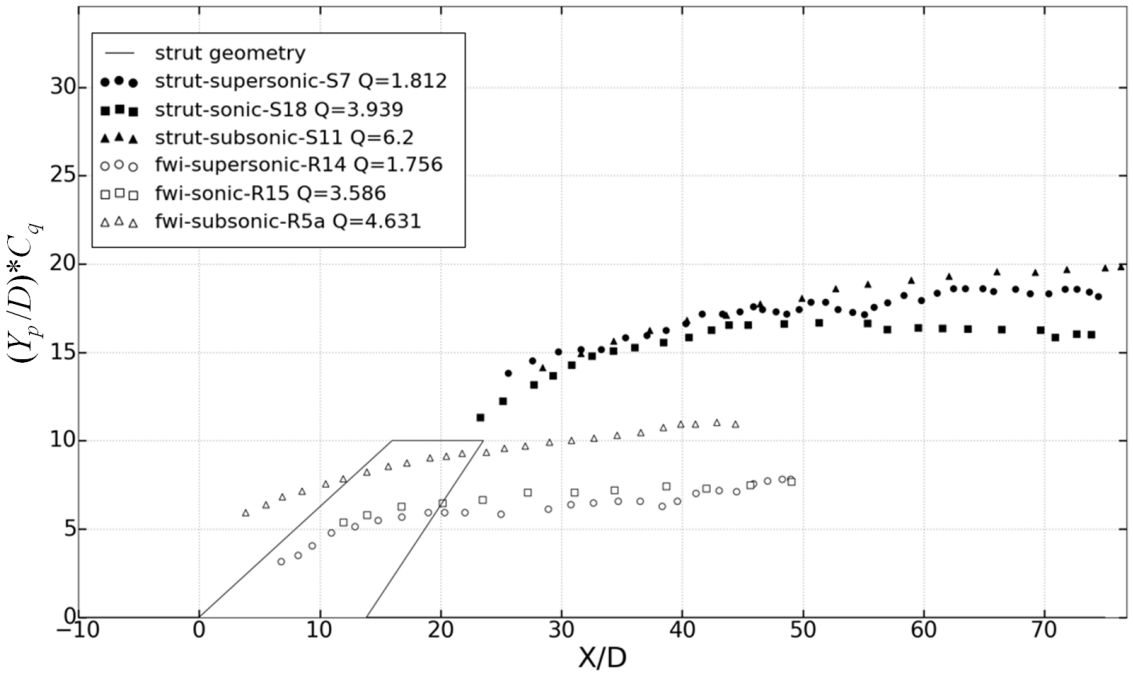

FIGURE 5.6: *Normalized jet penetration from the BOS images for the strut and flush wall injectors at supersonic, sonic, and subsonic mass-averaged Mach numbers.*

penetrate further for the same Q because the boundary layer protects the jet from the high momentum freestream flow. The relationship of Y_p/D and δ/D was discussed in section 4.2.

Figure 5.7 shows the wall static pressure measurements along the centerline of the top wall, opposite of the injector, for each of the runs shown in fig. 5.8. These data are normalized by the ambient pressure at the flowpath exit, P_{ref} and the mean uncertainty is $+/-0.13$. The triangular markers represent the experiments for subsonic flow; it can be seen that for the strut the incipient separation point of the boundary layer occurred between $-8.25D$ and $-4.5D$. For the FWI it is possible that the shock entered the nozzle because the incipient separation point is upstream of the first pressure tap, located $3.2D$ upstream of the nozzle exit. The nozzle exit pressure should be roughly $0.3P_{ref}$ as it is for the strut, however, it is roughly $0.6P_{ref}$.

For the supersonic and sonic flow cases of each injector a pressure spike occurs in

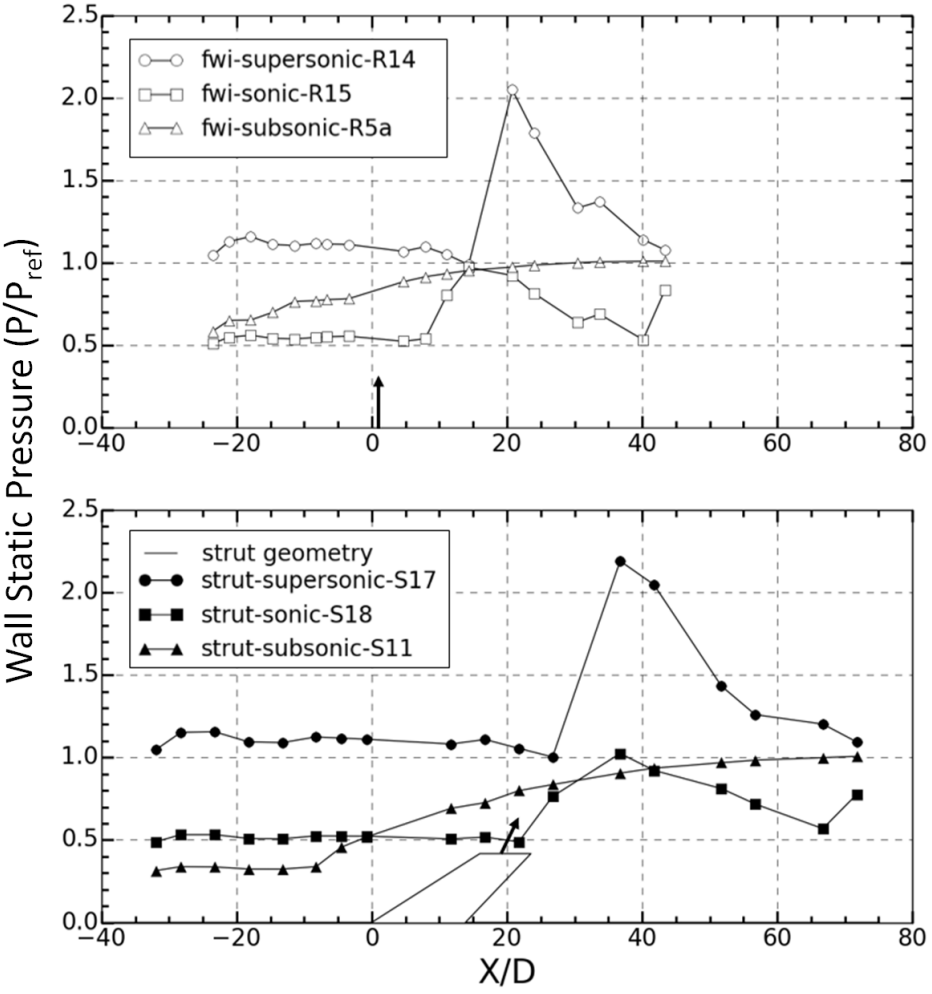

FIGURE 5.7: *Wall static pressure measurements along the top wall of the flowpath. The open and solid markers represent the FWI and strut, respectively.* P_{ref} *is the ambient pressure at the flowpath exit.*

the top wall pressure distribution downstream of the injector due to the bow shock from the injectors. The location where the shock strikes the wall can be seen in the BOS images of fig. 5.8 as well corresponding to the pressure spikes in fig. 5.7. The angles of the bow shocks for each case are similar (see table 5.1) and the physical locations where they strike the wall are the same.

The jet penetration from the strut tip injector has been shown to behave under the same physical principles as the flush wall injector. The results of this section shows that the jet penetration from a strut tip injector is not impacted by changes to the combustor inflow with the exception of the dynamic pressure ratio, Q. The normalization collapsed

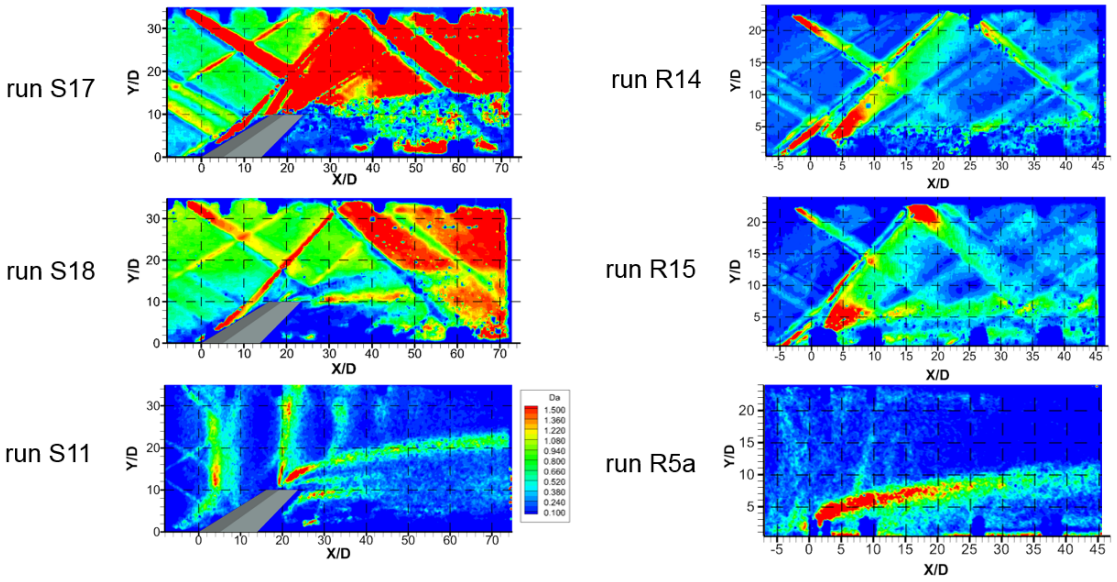

FIGURE 5.8: *BOS images corresponding to the data of fig. 5.6*

the jet penetration data to a uniform trend. This confirms that for this range in dynamic pressure ratio the jet penetration is proportional to Q to the 1/3 power.

5.5 Unique Case where Normal Shock due to Backpressure Locates at the Injector

In fig. 5.3c of section 5.2, it was shown that when a backpressure-induced shock separates the boundary layer on or near the flush wall injector port, it increases the turbulence intensity of the boundary layer. This propagates downstream through the mixing layer causing the the three-dimensionality and disorder of the large-scale coherent structures in the mixing layer to be greater. The increased turbulence increases the mixing by increasing the contact area between the helium and air. This section will discuss the impact to the jet penetration due to the presence of this shock, and the large pressure gradient which accompanies it, for both the strut injector and the flush wall injector.

Figure 5.9 shows the time-averaged BOS images for four select cases where a normal shock was located in the vicinity of the FWI and strut tip injector port. The top two images of the figure show the flowfields where the initial shock separates the boundary layer directly on the injector port. The lower two images show the flowfield where the shock train moves upstream of the injector and a secondary shock is located in the vicinity of the injector port. For the flush wall injector shown in fig. 5.9a, the backpressure-induced shock merges with the bow shock from the injector. The resultant shock is relatively strong for this flow, and there is not a well-formed shock train downstream from it. In fig. 5.9b, the normal shock merges with the oblique bow shock over the top of the strut, and a small bow shock appears to form in front of the injector jet.

For the flush wall injector shown in fig. 5.9c, the incipient separation of the boundary layer is upstream of the frame and a secondary shock is standing just upstream of the injector. Of these cases, fig. 5.9c is the only experiment where the signal to noise ratio of the instantaneous BOS images was qualitatively good enough to visualize the large-scale coherent structures. The effect of the shock on the mixing layer structure was discussed in section 5.2.

In fig. 5.9d, the initial normal shock slows the flow so that a bow shock is not able to form on the strut. To contrast this case with that of fig. 5.9b where there is an oblique bow shock on the leading edge of the strut. The flow was turned upwards through the oblique shock, directing the airflow upwards over the jet. In contrast to this, for the case of fig. 5.9d the air flow streamlines impact the helium jet perpendicularly and a normal bow shock forms merging with a backpressure induced normal shock. This normal shock is visible at 20 X/D.

The centerline wall pressure measurements for the top wall, which is opposite the

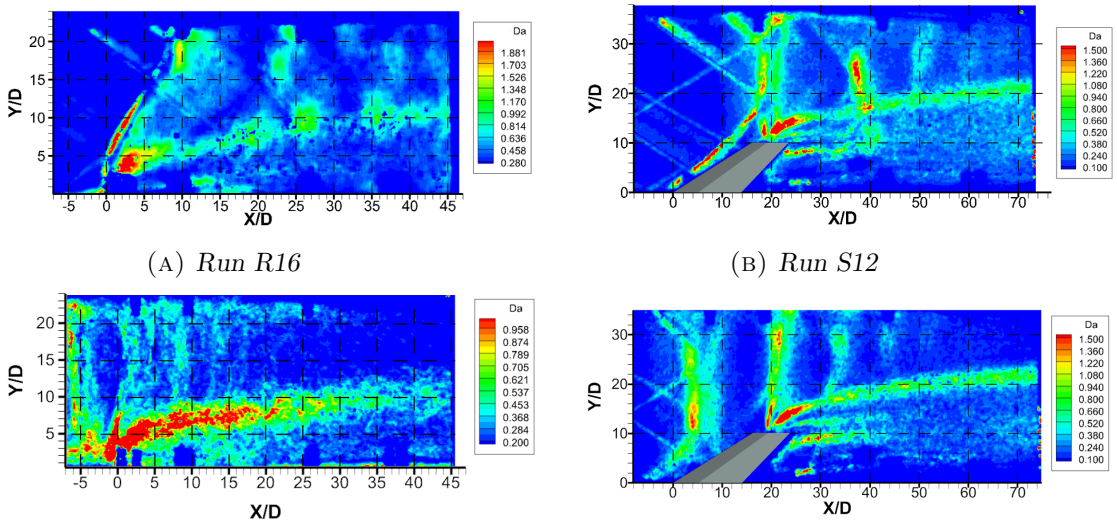

(A) *Run R16* (B) *Run S12*

(C) *Run R5b* (D) *Run S11*

FIGURE 5.9: *Time-average BOS images with standing shock on the injector port.*

injector, are shown in fig. 5.10a. The bottom two plots in this figure are for the strut injector. The pressure distribution shows that the incipient separation location occurs upstream of the normal shock due to the bifurcated oblique shocks near the wall at $X/D = 9$; this location is estimated from fig. 5.9b because it is between pressure taps. The pressure distribution shows that the flow is relatively undisturbed upstream of the injector, and smoothly rises to unity at the exit. Figure 5.10b shows the injector wall centerline pressure distribution. In this figure the incipient separation point for the flush wall injector, run R16, is seen to occur $8D$s upstream of the injector corresponding to the normal shock seen in the BOS image of fig. 5.9a. The pressure distributions for run R5a and R5b show that at the entrance of the flowpath the flow has already separated indicating that the initial backpressure induced shock is located upstream of the first pressure tap.

Figure 5.11 shows the normalized jet penetration for the previously discussed cases. In this figure, the presence of a normal shock on the injector port shows the same jet penetration as the case where the normal shock is upstream of the injector port. This is

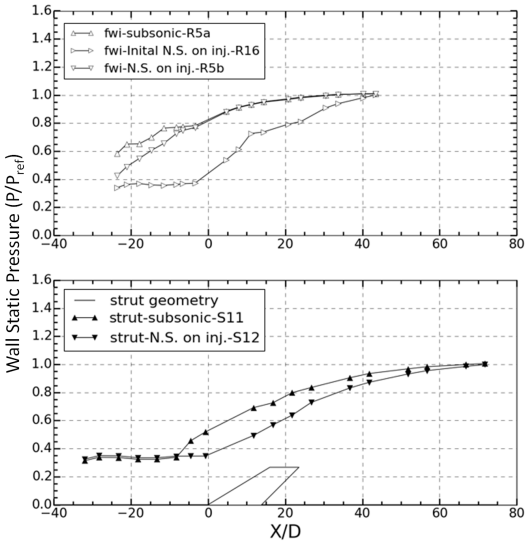

(A) *Wall pressure distribution along the centerline of the top wall for the subsonic cases where the normal shock is standing on the injector and in front of the injector.*

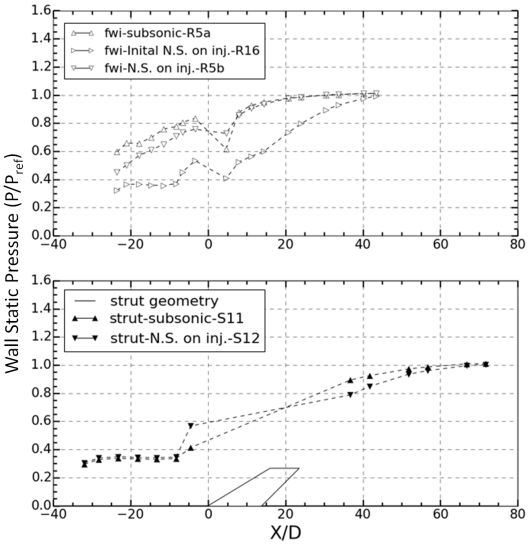

(B) *Wall pressure distribution along the centerline of the injector wall for the subsonic cases where the normal shock is standing on the injector and in front of the injector.*

FIGURE 5.10

true for both the strut injector and the flush wall injector. In section 5.4, it was shown that the jet penetration increases with increasing boundary layer thickness, δ/D. This does not happen for the strut tip injector since there is essentially no boundary layer to separate and no wall surface to support a separation region upstream of the injector port. This theory holds true for run S12, where the initial normal shock is incident on the injector port and the jet penetration normalizes with the subsonic flow case of run S11, as well as the supersonic and sonic flow cases.

There is an unpublished report from McDaniel which documented work done during the NASP program, where a similar flow scenario was studied. [75] The results of this study showed that for a constant Q, the jet penetration from a flush wall injector is constant while the backpressure-induced incipient separation point is located either upstream or downstream of the injector. However when the leading shock was incident on the injector port there was a roughly 50% increase in the jet penetration. This result

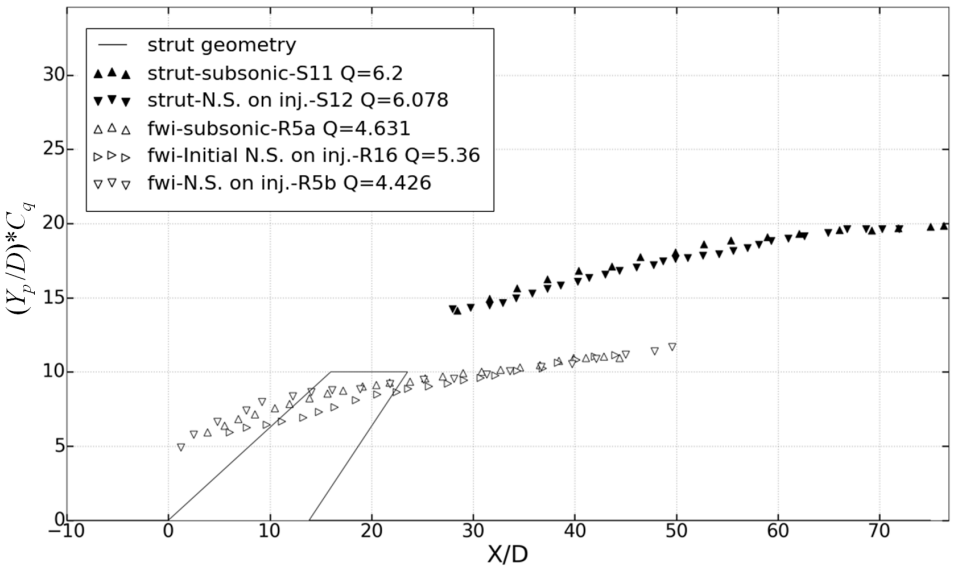

FIGURE 5.11: *Normalized jet penetration cases with shock on injector shows slightly increased penetration due to the shock.*

is seemingly contradictory to the results of this study, however the discrepancy may be attributed to differences in the boundary layer. In McDaniel's experiment, the injector was in a divergent flowpath, and the backpressure-induced shock system was oblique. These two factors could be an explanation for how the boundary layer is able to re-strengthen before it interacts with the injector. This is not the case for the experiments of this study, where the flowpath has a constant area, and the backpressure-induced shock system is normal; and when the boundary layer separates, it remains so. Therefore, when the incipient separation has any interaction with the injector, regardless of its proximity, the jet penetration will be enhanced due to a decrease in the momentum of the flow in boundary layer. For a strut tip injector, where $\delta/D \ll 1$, the jet penetration is independent of the cross-flow Mach number and the presence of backpressure-induced shock waves interacting with the jet.

5.6 Summary

In order to simulate the injection and mixing process within a dual-mode scramjet engine, the non-reacting mixing was evaluated in a backpressured flowpath. The interaction of shock waves with the helium jet, and effects of the shock-boundary layer interactions on the helium mixing and penetration were analyzed. The time-averaged BOS images with helium concentration contour slices were used to identify the effects of the shock waves and vorticity in the helium jet. The shocks generate baroclinic vorticity due to the streamwise pressure gradient and crossflow density gradient.

The mixing rate for the strut and flush wall injectors between the two measurement planes is roughly the same, for the same flow condition. The mixing rate is affected by the turbulence intensity within the mixing layer. [103] When a shock or other pressure gradient is present on the injector it increases the turbulence, and thereby increases the mixing rate. This was qualitatively captured using the instantaneous BOS images, where the 2-D coherent structures are clearly visible when the shocks are upstream of the injector. When a normal shock is present on the injector, the turbulence of the boundary layer increases, breaking up the organized structure of the mixing layer, while the convective Mach number is unchanged. Therefore, the presence of a shock on the injector enhances mixing.

For all of the flow regimes tested, from subsonic to supersonic, the jet penetration from the strut tip injector is independent of the flow conditions and shock structure. The relationship of the jet penetration is, therefore, only dependent on dynamic pressure to the 1/3 power. It makes sense that boundary layer separation on the wall will not affect the jet penetration for the strut. However, even when a shock impinges on the strut tip injector, there is no increase in jet penetration. This occurs because δ/D is very small,

and the boundary layer has no wall surface to separate from. The 1/3 power law is valid for the flush wall injector as well. However, when the boundary layer separates on or upstream of the injector, the increase in the boundary layer thickness, increases the jet penetration.

Chapter 6

Conclusions

Scramjet engines are being developed to meet the propulsion needs of hypersonic vehicles for military and civil application. Within the technology maturation roadmap for scramjets, there is a need to develop fuel injection and mixing devices which can efficiently support combustion in a large-scale combustor. Strut injectors are slender body, injection and mixing devices, which deliver fuel to the core flow of the combustor. These devices are intrusive to the flow, increasing the internal drag, and have high thermal loads to manage. Dual-mode scramjet combustors must be able to operate over a wide range of flow conditions, from subsonic to supersonic and with varying levels of mixed speed flow. There are shock waves, and numerous shock-boundary layer interactions which occur around the fuel injector and can have critical effects on the injection and mixing.

6.1 Summary

Experiments were performed in a Mach 2, unheated flow using helium to simulate hydrogen fuel. To simulate dual-mode combustion the flowpath was backpressured. With the exit pressure fixed at atmospheric pressure for all runs, three inflow pressures were tested that resulted in subsonic, sonic, and supersonic mass-averaged Mach numbers in the vicinity of the injector. Two injectors were tested: a swept strut having a sonic injector port on the tip surface and another port in the wall behind the strut, as well as a normal flush wall injector to serve as a baseline. A gas sampling system, was developed to measure the time-averaged helium concentration at points throughout the exit plane of the flowpath. The mean error of this measurement system across all of the runs was $2.2\%FS$. An in-stream rake held the gas sampling probe and a Pitot pressure probe, and was scanned over the exit plane of the flowpath. Two measurement planes were scanned by changing the length of the flowpath, from which crossflow contour plots of the helium concentration were created and mixing efficiency was calculated. Background Oriented Schlieren (BOS) was used to visualize the helium mixing jet, from which the jet penetration was measured, and a qualitative identification of flow structures in the helium jet were documented. The BOS images were also used for instantaneous visualization of the mixing layer structures for the flush wall injector, from which the convective Mach number was calculated.

For the non-backpressured, Mach 2 flow, the helium penetration at the far measurement plane, $X/D = 76.8$, reached 45% of the strut height, measured above the top of the strut. By comparing the strut injector to the flush wall injector, it was shown that for a minimal decrease in total pressure recovery there was a trade-off between mixing efficiency and helium penetration. The higher mixing efficiency for the flush wall injector

is primarily due to the increased strength of the counter-rotating vortices which entrain air into the helium jet in the near field. These vortices are generated by the pressure gradient between the horseshoe bow shock around the front and sides of the injector port, and the wake region behind the injector port. The strut tip injector is not able to generate the same strength vortices because the bow shock on the injector is much weaker and does not have a separation region upstream of the injector. Furthermore, there is no surface to the sides of the injector for the horseshoe bow shock to build pressure around the side of the injector port.

The range of the far field mixing was defined as the distance from the injector when the mixing becomes dominated by diffusion and convective processes. Regardless of the injection process, in the far field, the mixing rate will only be dependent on coherent structures of the mixing layer, which means that with an increase in compressibility or increase in turbulence, the mixing rate will increase. This was shown experimentally by the mixing efficiency data and jet penetration for both the strut and flush wall injectors. Instantaneous BOS images were used to observe the mixing layer structures and measure the convective Mach number for the FWI. It was observed that when the convective Mach number increased from 0.3 to 0.6, the coherent mixing layer structures went from organized 2-D rolling waves to much smaller, presumably 3-D waves. This observation is corroborated by the work of Clemens and Mungal, who observed this transition in the coherent structures at $M_c = 0.5$. [27] When a normal shock was present on the injector, for $M_c = 0.3$, the large-scale coherent structures of the mixing layer were broken up by the turbulence in the boundary layer upstream of the injector. The increased turbulence within the mixing jet means that the presence of a shock on the injector enhances mixing.

When the jet penetration from the strut tip injector is normalized by the dynamic

pressure raised to the 1/3 power, it becomes consistent with downstream distance for all flow conditions. Differences in the jet penetration far downstream from the injector correlate to reflected shock waves, which turn the flow downward, causing the jet penetration to flatten beyond $50D$'s. When the wall boundary layer is separated upstream of the strut injector the jet penetration is unaffected because the injector is always above the boundary layer. When this occurs for the flush wall injector, however, the jet penetration increases due to reduced momentum and increased thickness of the boundary layer. When a shock is located on the injector port of the strut tip, there is still no change in the jet penetration. The lack of boundary layer and surface area relative to the injector port diameter precludes the development of a separation region around the injector, and so the penetration cannot be affected by changes other than the dynamic pressure ratio. For the flush wall injector the penetration does not change whether there is a shock located on or upstream of the injector port. This is only true if the state of the boundary layer does not change once it is separated. Essentially for the flush wall injector the boundary layer properties at the point of injection must always be considered for analyzing the jet penetration.

6.2 Significance of the Research

The results of this research provides a general understanding of the fuel-air mixing behavior of a strut tip injector in a dual-mode scramjet combustor. The helium plume was quantified by the jet penetration and mixing efficiency. The flow properties and structures used to characterize the state of the airflow were; the mass-averaged and convective Mach numbers, dynamic pressure ratio, boundary layer thickness, and shock wave interactions. This research provides the first detailed investigation into the flowfield

surrounding a strut with a tip injector. This study utilizes both CFD and experimental data to identify the flow physics. The results led to the conclusion that the lack of boundary layer and wall surface relative to the strut tip injector port diameter inhibits production of counter-rotating vortices, and that the jet penetration from the strut is insensitive to the presence of shock waves near the injector port.

The strut designed for this study showed a jet penetration of 45% of the strut height, measured from strut tip into the coreflow. This constitutes a substantial improvement relative to the supporting research used to develop this strut, which did not show penetration appreciably above the height of the strut, even when tip injection was employed. [57, 99] The increased penetration with minimal pressure loss is attributable to the thinness of the strut and low fuel pressure loss through the internal passage to the injector port. The wall injector port located behind the strut improved the jet penetration, as was shown by the CFD cases in chapter 3. This strut was only practical to manufacture because of 3-D printing technology. Utilizing this technology provided a unique opportunity to build and test an injector design that has never been tried before.

The availability of data sets in the open literature for non-reacting mixing in backpressured flowfields, is limited. This research provides the following data in conditions from fully subsonic to Mach 2 crossflow: detailed flow visualizations of the mixing jet, in-stream helium concentration contours, and integrated one-dimensionalized mixing characteristics computed from the in-stream gas sampling and Pitot pressure measurements. The results show that the jet penetration is proportional to the dynamic pressure ratio raised to the 1/3 power. The specific case where a backpressure-induced shock wave interacted with the injector bow shock was examined, as well. It was found for the flush wall injector that the shock introduced turbulence to the mixing jet, breaking up the organized coherent structures that were present in the helium jet without the normal

shock. This implies that the presence of the shock increases the mixing rate. Future work will be proposed in a subsequent section to further investigate these results.

Schlieren imaging of supersonic mixing has a long history of use, and while examples of Background Oriented Schlieren (BOS) used for this purpose is not widely available, using BOS to qualitatively assess the mixing flowfield is not very different from any other schlieren. The advantage of BOS, however, is its simplistic setup, and that the images are built on quantitative data that is directly proportional to the line-of-sight integrated density gradient. The contribution of this research is the calibration of BOS data to mole fraction concentration of injectant through in-stream gas sampling measurements in a scramjet mixing environment. It was found that information about the cross-sectional shape, and the average mole fraction of the mixing jet can be determined from the BOS images.

6.3 Implications on Real World Systems

The innovations and technical contributions provided by this research can be applied towards the design of a scramjet fueling system, and an expectation for the combustion process can be inferred. However, it should be understood that this injector is not a complete device. In a real scramjet fueling system, it would be coupled with a flame-holder, and possibly a mixing device, and would be configured in an array, depending on the cross section of the combustor. For the purposes of designing large-scale combustors, the following design parameters could be derived from this research: the strut height and penetration, the combustor length, and expected mixing efficiency. For example, consider a round scramjet combustor cross section of diameter, D_c. Where the fuel total pressure is $P_{t,fuel}$, the height of the strut is h_{strut}, the injector diameter is D, and the

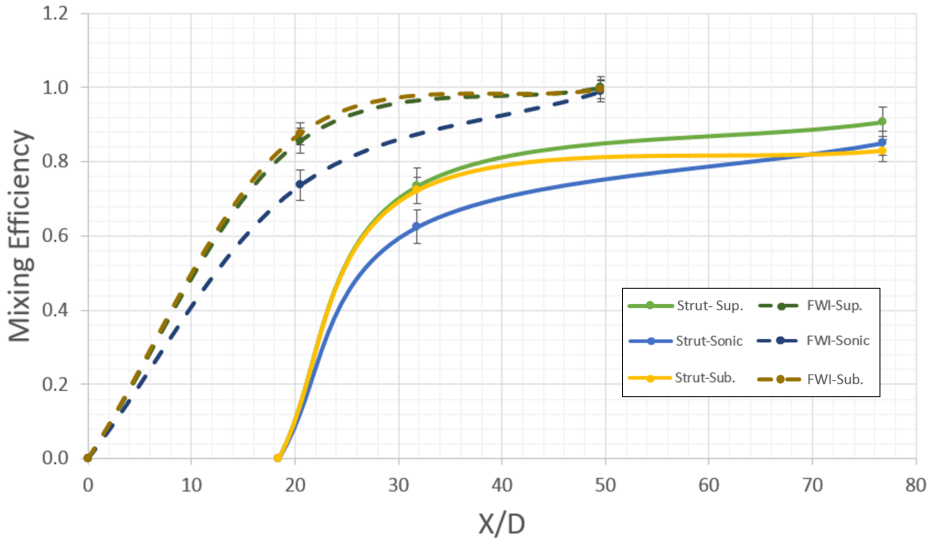

FIGURE 6.1: *Mixing efficiency vs. axial distance for the strut and flush wall injectors.*

maximum jet penetration is $Y_{p,max}$. Equation 6.1 outlines the scaling principles for the height of the strut. If the fuel pressure requirement is determined by the required $Y_{p,max}$, then the fuel equivalence ratio, ϕ, can only be modified by the injector throat diameter. This is assuming a fixed fuel temperature.

Figure 6.1 shows the mixing efficiency vs. combustor length; the data trend lines show an approximation based on the three available data points. This illustrates the response curve, for mixing efficiency with changing flow conditions, from which a designer could calculate estimations of mixing and combustor length. Considering the error on the individual measurements, this trend line would make a close approximation of the mixing at any axial station.

$$\left.\begin{aligned} h_{strut} &= \tfrac{D_c}{2} - Y_{p,max} \\ Q \propto P_{t,fuel} &\propto (Y_{p,max})^3 \\ \phi &\propto D \end{aligned}\right\} \tag{6.1}$$

These experiments used helium to simulate hydrogen fuel. The difference in molecular weight and ratio of specific heats, γ, must be taken into account when calculating the target equivalence ratio and dynamic pressure ratio between the non-reacting experiment and a combustion application. See table A.1 for a list of the gas properties. The response of the fuel injection and jet penetration to a change in gas properties, from helium to hydrogen, can be demonstrated analytically, assuming that for each gas, a sonic injector port, a constant $P_{t,fuel}$, and the molar fuel to air ratio f^o, of hydrogen in air, are used. See table 6.2 for a list of the assumptions. It follows from eq. 6.2, that the mass flow will scale by the ratio of molecular weights, and the scaling factor for the injector port diameter is 0.596. The dynamic pressure ratio, Q, from helium to hydrogen will then scale by eq. 6.3, which will impact the jet penetration according to eq. 6.4. Therefore, the jet penetration will scale 3% lower for hydrogen fuel when applying the conditions of a non-reacting helium experiment to a combustion application.

TABLE 6.1: *Gas properties*

Property	Helium	Hydrogen
Molecular weight	4.003	2.0158
γ	1.667	1.4
R	2.077	4.124

TABLE 6.2: *Assumptions for scaling analysis*

Property	Assumption
f^o	$f^o_{he} = f^o_{h_2}$
Mach number	$M_{he} = M_{h_2}$
$P_{t,fuel}$	$P_{t,he} = P_{t,h_2}$
$\dot{m}$	$\frac{\dot{m}_{he}}{\dot{m}_{h_2}} = \frac{MW_{he}}{MW_{h_2}}$
T	$T_{he} = T_{h_2}$

$$\left.\begin{array}{c} \frac{D_{h_2}}{D_{he}} = \frac{\left(P\sqrt{\frac{\gamma}{R}}\right)_{he}}{\left(P\sqrt{\frac{\gamma}{R}}\right)_{h_2}} \\ where,\ P_{he} = 0.487 P_{t,fuel}\ ,\ and\ P_{h_2} = 0.528 P_{t,fuel} \\ \frac{D_{h_2}}{D_{he}} = 0.596 \end{array}\right\} \tag{6.2}$$

$$\left.\begin{array}{c} Q = \frac{\gamma}{2} P M^2 \\ \frac{Q_{he}}{Q_{h_2}} = 0.910 \end{array}\right\} \tag{6.3}$$

$$\frac{(Y/D)_{h_2}}{(Y/D)_{he}} \propto \left(\frac{Q_{he}}{Q_{h_2}}\right)^{1/3} = 0.969 \tag{6.4}$$

This research constitutes a significant impact for the physical understanding of a strut tip injector in a dual-mode scramjet combustor, and provides the tools to apply this research to combustion applications. A designer could take this work and design a scramjet fueling system that includes a strut with tip injection. This research has shown many benefits to doing so, if fuel penetration is a key necessity. This work shows that for a strut injector in a dual-mode scramjet, the fuel penetration can be accurately predicted, because Q can be determined by measuring the flight conditions and fuel conditions.

6.4 Future Work

This research builds on the previous knowledge of strut fuel injector concepts, and the fuel injection and mixing in dual-mode scramjet flows. The next steps for this work include; further investigation of the mixing layer flow structure with backpressure-induced shock waves, further application of the BOS measurement for evaluating mixing, and computational and experimental analysis of the strut tip injectors for combustion applications.

The instantaneous BOS images of the flush wall injector, with the shock impinging on the injector port, showed an increase in the turbulence of the mixing layer. This increase is in comparison to a flow with the same compressibility, but where the shocks were upstream. The theory of mixing layers implies that the increased turbulence will translate into increased mixing. This flow scenario should be repeated so that gas sampling measurements can be made. The mixing efficiency can be calculated from these measurements and compared to the case where the shocks are upstream and downstream of the injector. If the mixing efficiency is higher, as expected, it would constitute a significant process for mixing enhancement.

The BOS measurement technique coupled with in-stream gas sampling measurements represents an interesting opportunity for measuring mixing characteristics in an experimental flow. The methodology involves calibrating a time-averaged BOS image with gas sampling data taken at the downstream limit of the image field of view. It was shown in section 3.9 that this methodology allows for the BOS image to be utilized for extracting mixing characteristics such as jet penetration, mean injectant concentration of the jet, and cross-sectional shape patterns of the mixing jet. The issues with the BOS data from this study were that most of the experiments, specifically for the high-pressure, supersonic cases, had good sensitivity on the upper boundary of the mixing jet and airflow, but not within the mixing jet. With improvements to the experimental setup, specifically the quality of the windows, and the intensity of background lighting, this measurement technique could be applied to all of the experimental conditions.

Finally, testing of this strut design has shown, through analysis of the jet penetration and mixing efficiency, that injection from the tip of the strut can provide an improvement over the available methods for penetration of fuel into a scramjet combustor. The next step for testing of this strut is to begin the design and analysis process

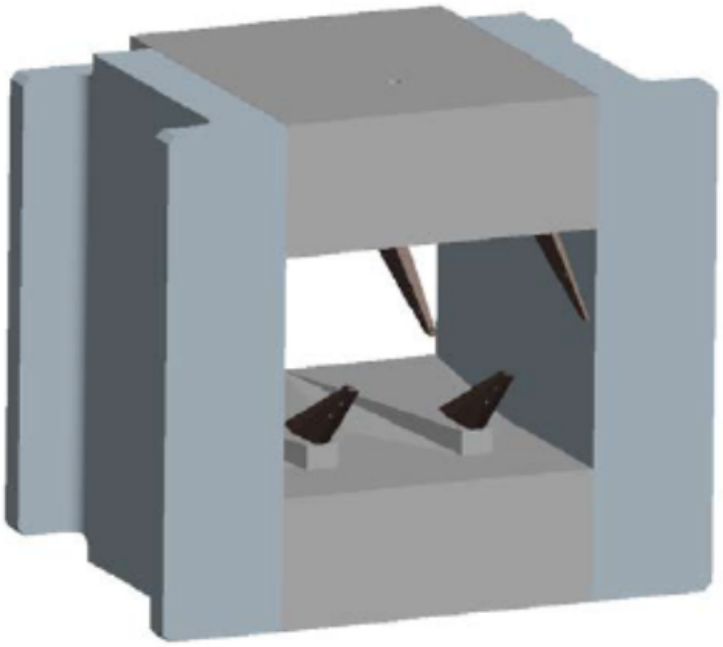

FIGURE 6.2: *Conceptual drawing of a strut injector configured into a complete scramjet piloting system.*

for applying this strut to a real scramjet combustion experiment. The first step in this process is to perform a thermal analysis of this strut to determine the temperature the strut material will reach when it thermally balances. If that temperature exceeds the mechanical limits, then the design must be reconfigured to satisfy this requirement. It is possible that a thermal protection coating such as zirconia oxide will be necessary. Following this process the strut has to be incorporated into a complete scramjet piloting system; an example of this concept is shown in fig. 6.2. Since the results of this study show that the mixing of the strut injector is initially low, this conceptual design is intended to initiate counter-rotating vortices upstream of the strut.

This work has raised many new questions about the possibilities of strut fuel injection for dual-mode scramjet combustors. Strut tip injectors show significant improvement for delivering fuel to the core flow, while limiting the exposure of mechanical surfaces to the flow. In addition, the lack of a boundary layer at the strut tip provides predictability for the jet penetration. This is a considerable advantage for designing

combustors, which must operate over a range of flow conditions. Overall this was a successful research effort, and it is expected that this work shall be applied in furthering the knowledge of scramjet propulsion.

Appendix A

Principles of Measuring the Concentration of a Binary Gas Mixture using a Hotwire

The hotwire system is an inexpensive and effective method for accurately measuring the time-averaged concentration of a binary mixture of gases. There are some limitations to this technique, however, the gases must contrast each other in heat transfer properties; they should be inert to avoid reactions with the hotwire or hotfilm filament; the pressure and temperature of the sample stream must be controlled or calibrated for. This section discusses the physics and equipment necessary to make an accurate gas sampling concentration measurement.

A.1 Physics of Constant Temperature Anemometry

A hotfilm or hotwire sensor, as it will be called from here on, is a filament or film-coated wire that is stretched across two supportive prongs. The material for the wire or film can be tungsten, platinum, nickel, or some alloy of these metals. When the temperature of these metals change the electrical resistance changes. For these experiments, a 55R01 Dantec hotfilm probe was used, which has a nickel film. An electrical device called a Constant Temperature Anemometer (CTA) is used to control the hotwire response such that the velocity and turbulence of a flow could be measured by the change in heat transfer from the wire. Equation A.1 shows the heat transfer equation, where the heat transfer coefficient, h, is modelled for a cylinder in cross-flow, and A_w is the surface area of the wire. The CTA is essentially a wheatstone bridge, where one of the resistive legs is the hotwire, and a servo amplifier maintains the wire resistance by adjusting the current through the hotwire. The response time of the CTA to changes in the hotwire resistance is up to 1000 times faster than the response from the wire itself. The bridge voltage, E, is related to the heat transfer by eq. A.1. A schematic showing the process of collecting and processing data from a hotwire and CTA system is shown in fig. A.1. [64]

$$heat\ transfer = hA_w\left(T_w - T_{gas}\right) = \frac{E^2}{R_w} \tag{A.1}$$

The heat transfer from the wire, represented by eq. A.1 is balanced by the electric power input to the wire to keep it at a constant temperature. Conduction of heat through the ends of the wire is neglected. Equation A.2 is an empirical model for the Nussult number for a cylinder in crossflow. This equation is used in eq. A.3 to determine the heat transfer coefficient, h. If the temperature, pressure and Mach number are held

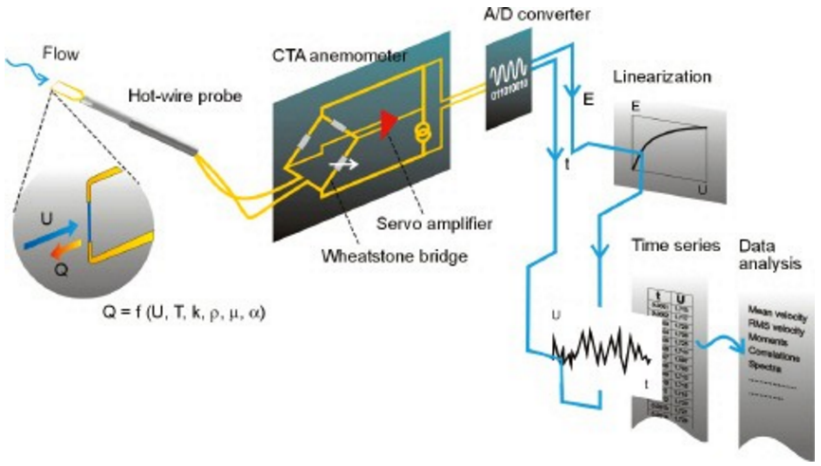

FIGURE A.1: *Schematic of a hotwire and CTA measurement.*

constant, then the heat transfer coefficient can only be a function of the gas composition. The change in γ and viscosity will effect the Reynolds number, Re, and the change in the coefficient of thermal conductivity, k, will have a direct affect on the heat transfer coefficient. Controlling temperature, is achieved by a heat exchanger coil, since the total temperature of the experimental gas is near room temperature, the laboratory air is used as a thermal reservoir. The temperature of the gas is monitored with a rapid response thermocouple to ensure that the sample temperature is constant. The pressure is maintained by venting the sample to the laboratory and picking off a small portion of this stream, a transducer monitors the pressure as well to ensure compliance. Lastly the Mach number is fixed by placing a choked orifice downstream of the hotwire probe, where there is vacuum downstream of the orifice. This fixes the A/A^* such that the Mach number is fixed.

$$Nu = 0.32 + 0.43Re^{0.52} \tag{A.2}$$

$$h = \frac{Nu\ k}{D_{hw}} \tag{A.3}$$

In order to measure the concentration of the binary mixture, the two gases must

TABLE A.1: *Sensitivity of CTA to binary mixtures of a gas species with air.*

Gas Species	k @ 300 K $[W/mK]$ 10^3	γ @ 300 K	CTA signal $[\Delta V/\Delta mf]$
air	26.2	1.4	-
helium	156.7	1.67	1.260
Carbon Dioxide	16.8	1.23	0.075
Argon	17.9	1.67	0.220
Hydrogen*	186.9	1.4	0.820

*CTA signal not stable over time

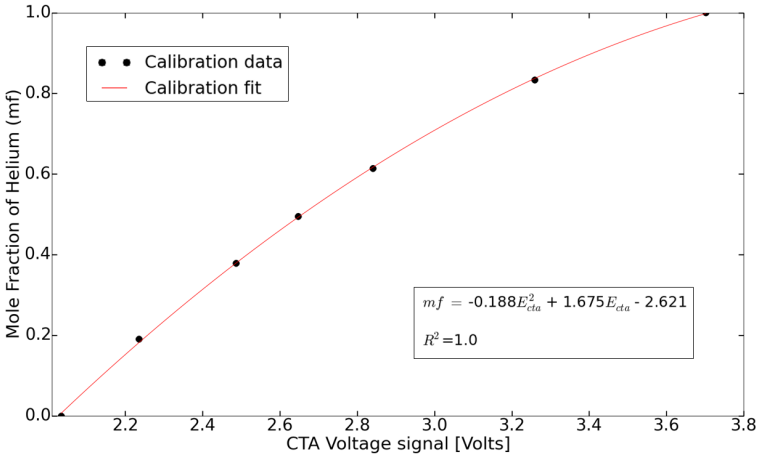

FIGURE A.2: *Calibration curve from run day 7-27-15*

have sufficiently different coefficients of thermal conductivity. A difference in γ alone is not enough to provide sufficient sensitivity of the CTA output signal to the mixture concentration. This is shown in table A.1, where the CTA signal output for different gas species mixed with air increases with increasing difference in coefficient of thermal conductivity. Hydrogen has good sensitivity, however, due to its reactivity, this test resulted in permanent degradation of the hotwire. The CTA signal is calibrated for mole fraction of the mixture by flowing known, volumetric quantities of the two gases, from 0% to 100% of the measurand gas and air. An example of the resulting calibration curve is shown in fig. A.2, the polynomial of eq. A.4 was used to fit the data.

$$mf = C_2E^2 + C_1E + C_0 \tag{A.4}$$

A.2 Data Reduction and Uncertainty Quantification

The calibration data is collected automatically from a Labview routine, two stepper motors control a throttling valve for the helium and air flows, and a solenoid on each gas line starts and stops the flow. The mole fraction of helium, mf, is equivalent to the fraction of volumetric flowrate, $\dot{q}$, by eq. A.5. Figure A.3 shows a flow chart, of the helium and air flow as the calibration routine steps through from 0 to 1 mole fraction of helium, mf. At each step in the flow chart the flowrates, and CTA signal are sampled at 100 Hz, for 5 seconds. The middle 250 samples are used to exclude data where the flowrates are changing in time. Each calibration point is therefore the mean of 250 samples. The calibration is performed at the start and end of every run day so that changes in room temperature and pressure do not affect the calibration. For each run day it was found that the difference in calibration coefficients between the pre-run calibration and post-run calibration was negligible. Day to day, the calibration coefficients drifted, and the errors were not always consistent; table C.1 shows the mean error and the maximum error of the calibration points for each run day. The maximum calibration error was applied to the experimental data.

$$mf = \frac{\dot{q}_{he}}{\dot{q}_{he} + \dot{q}_{air}} \tag{A.5}$$

The uncertainty in mf is calculated from the Root Sum Square (RSS) of the errors, and the uncertainties times their sensitivity. The general form of the uncertainty equation is:

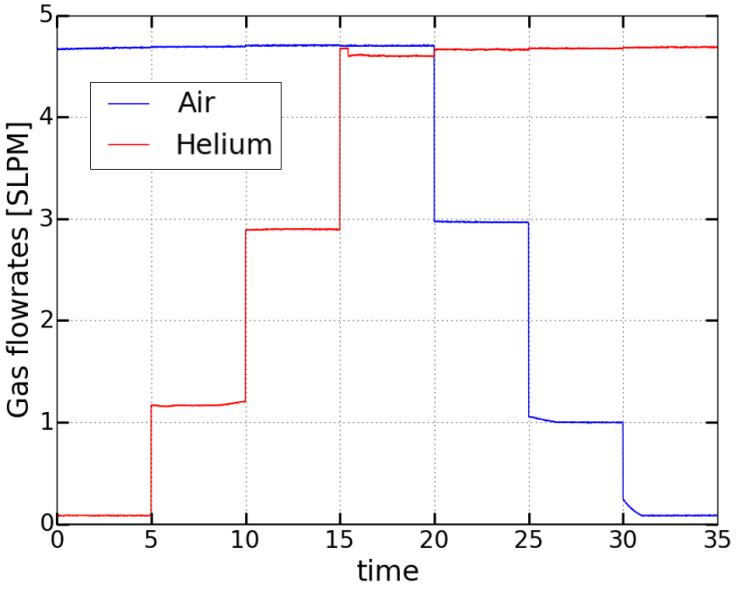

FIGURE A.3: *Calibration flow for helium and air for run day 7-27-15.*

TABLE A.2: *Mean calibration error from each run day*

Run day	Mean cal. error (+/-) mf	Maximum cal. error (+/-) mf
7-23-15	0.024	0.0410
7-27-15	0.011	0.0176
7-28-15	0.010	0.0162
7-29-15	0.015	0.0225
8-4-15	0.011	0.0167
8-5-15	0.009	0.0167
8-12-15	0.010	0.0172

$$\mu mf = \left[e_{mf}^2 + \left(\frac{\partial mf}{\partial E_{CTA}} \mu E_{CTA} \right)^2 \right]^{1/2} \tag{A.6}$$

Where μX is the applied uncertainty of X, and e_x is the measured error of x. The mf comes from the calibration equation of, shown in eq. A.7, where the sensitivity of mf to the CTA voltage, E_{CTA}, is given by eq. A.8.

$$mf = C_1 E_{CTA}^2 + C_2 E_{CTA} + C_3 \tag{A.7}$$

$$\frac{\partial mf}{\partial E_{CTA}} = 2C_1 E_{CTA} + C_2 \tag{A.8}$$

Equation A.9, shows the error in mf, e_{mf}, comes from the uncertainty due to the measured flowrates of helium, $\dot{q}_{he}$, and air, $\dot{q}_{air}$, multiplied by their respective sensitivities to the mf. Equation A.5 is used to calculate the sensitivities shown in equations A.10 and A.11. The last term, e_{cal} is the error due to the calibration coefficient of the least squares fit. It is calculated from eq. A.12, which is the difference between the calculated mf using eq. A.7, and the measured mf at the measured E_{CTA}.

$$e_{mf} = \left[\left(\frac{\partial mf}{\partial \dot{q}_{he}} \mu \dot{q}_{he} \right)^2 + \left(\frac{\partial mf}{\partial \dot{q}_{air}} \mu \dot{q}_{air} \right)^2 + e_{cal}^2 \right]^{1/2} \tag{A.9}$$

$$\frac{\partial mf}{\partial \dot{q}_{he}} = \frac{-mf}{\dot{q}_{he} + \dot{q}_{air}} \tag{A.10}$$

$$\frac{\partial mf}{\partial \dot{q}_{air}} = \frac{1 - mf}{\dot{q}_{he} + \dot{q}_{air}} \tag{A.11}$$

$$e_{cal} = mf_{cal} - mf_{meas} \tag{A.12}$$

The uncertainty in the flowrate measurements is given by eq. A.13, where x is the gas being measured, and μ_{instr} is the instrument uncertainty from the NIST calibration. The error in the flowrate measurement, $e_{\dot{q}_x}$, is given by eq. A.14, where V_x is the output voltage from the instrument and $t_{stat} = 2.054$ for the 98% confidence interval. The standard deviation of the measurement is denoted by σ.

$$\left.\begin{aligned} \mu \dot{q}_x &= \left[\mu_{meter}^2 + e_{\dot{q}_x}^2 \right]^{1/2} \\ \mu_{meter} &= 0.0094 \end{aligned}\right\} \tag{A.13}$$

$$e_{\dot{q}_x} = \left[\left(\frac{\partial \dot{q}_x}{\partial V_x} \right)^2 (t_{stat}\sigma_x)^2 \right]^{1/2} \tag{A.14}$$

$$\frac{\partial \dot{q}_{he}}{\partial V_{he}} = 1.00217 \quad \frac{\partial \dot{q}_{air}}{\partial V_{air}} = 1.00436 \tag{A.15}$$

The uncertainty in E_{CTA} is given by eq. A.16. The contributions in uncertainty due to the pressure and temperature fluctuations are negligible because the sensitivities to E_{CTA} are small, and fluctuations in pressure and temperature are small so this was not a significant source of error. The CTA instrument uncertainty is specified to be negligible by the manufacturer.

$$\mu E_{CTA} = \left[\mu_{CTA}^2 + (t_{stat}\sigma_{E_{CTA}})^2 + \left(\frac{\partial P}{\partial E_{CTA}} \mu P \right)^2 + \left(\frac{\partial T}{\partial E_{CTA}} \mu T \right)^2 \right]^{1/2} \tag{A.16}$$

$$\mu_{CTA} \approx 0 \quad \left(\tfrac{\partial P}{\partial E_{CTA}} \mu P \right) \approx 0 \quad \left(\tfrac{\partial T}{\partial E_{CTA}} \mu T \right) \approx 0 \tag{A.17}$$

This analysis quantifies the uncertainty in the Gas Sampling and Analysis System (GSAS) developed to make accurate mole fraction measurements for a supersonic non-reacting fuel-air mixing experiment. The results from the calibrations for each run day of this study, given in table C.1, shows that this system operates consistently. The target uncertainty, set as a requirement for the system design to meet, was $1\%FS$. This system was close to meeting that standard, with improvement in the devices such as higher accuracy flow meters and controllers, the error and consistency could be reduced to meet the requirement. For the purposes of these experiments however, this uncertainty was more than enough to make accurate assessments of the flow physics.

Appendix B

Facility and Experimental Supporting Documentation

This section contains the schematics of the facility and experimental equipment. The photos show the two flowpath configurations tested, with the strut injector installed, and a photo of the general experimental setup is given. Tables showing the complete test matrix with the experimental conditions, and a list of the instrumentation are given.

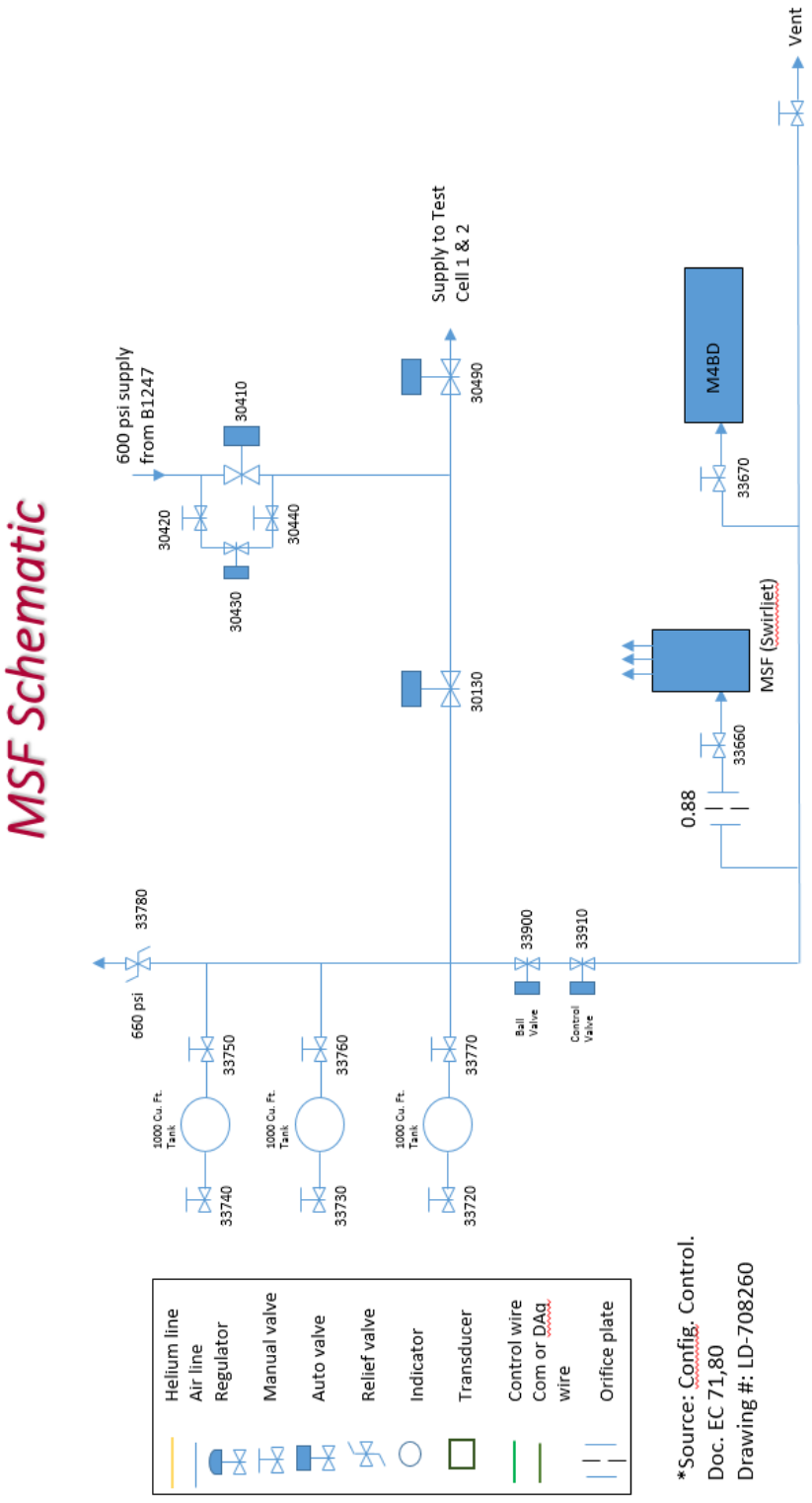

FIGURE B.1: Schematic of the Mixing Studies Facility at NASA Langley Research Center.

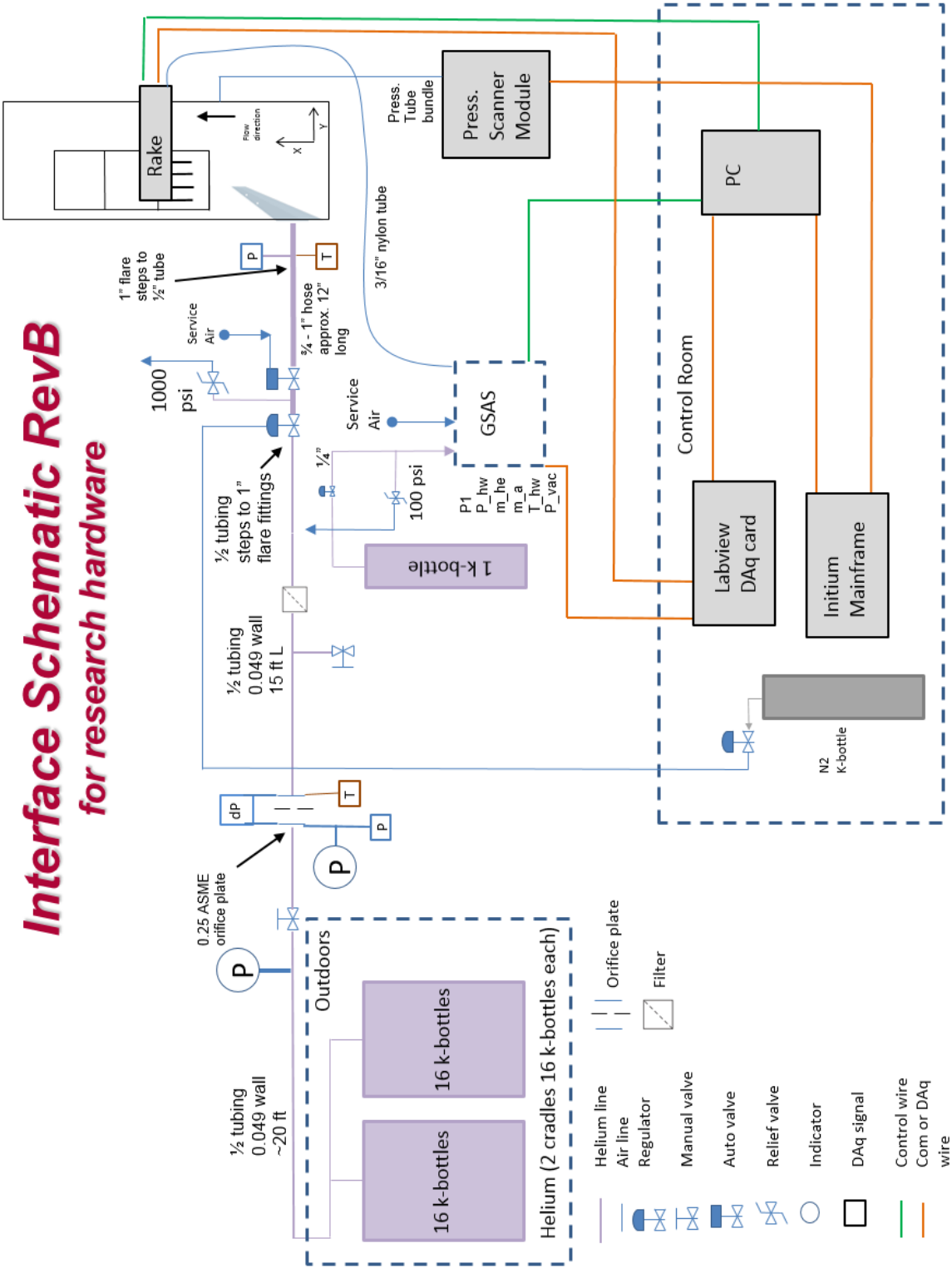

FIGURE B.2: Schematic of the experiment equipment.

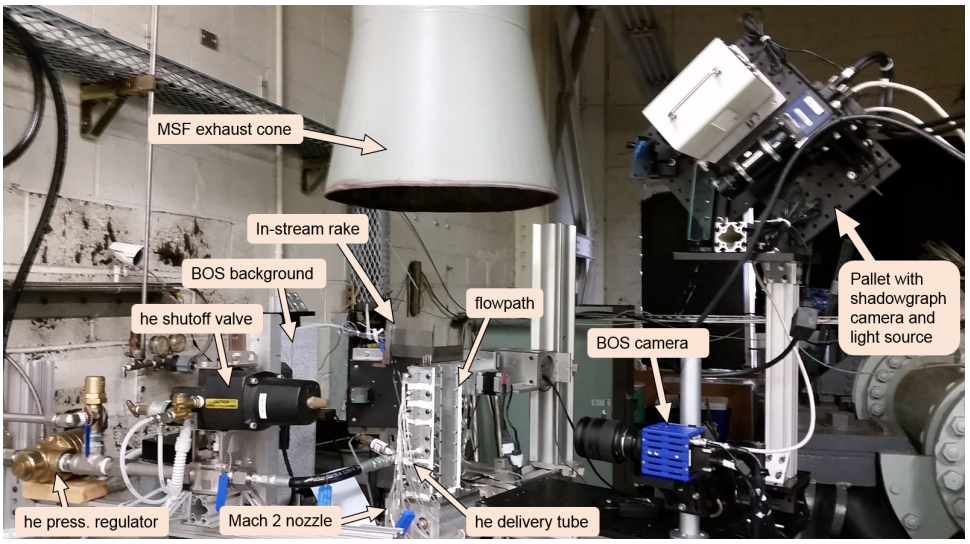

FIGURE B.3: *Photograph of the experimental setup.*

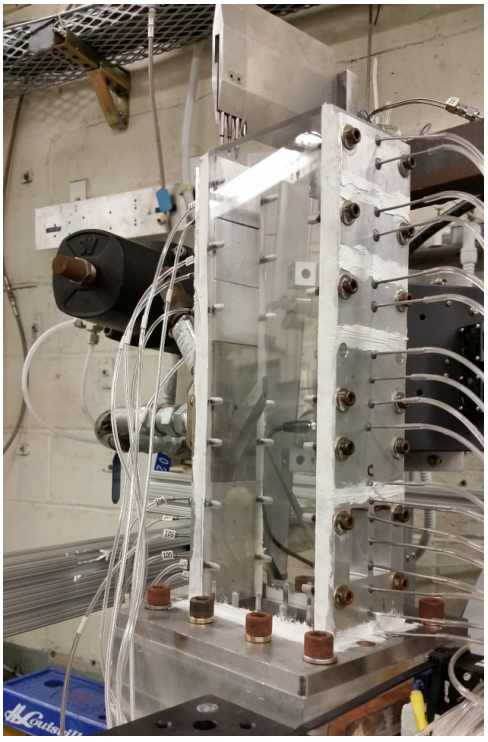

(A) *Long flowpath configuration, 11 inches total length.*

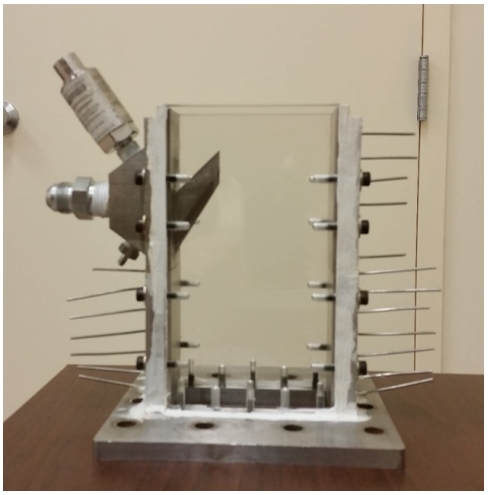

(B) *Short flowpath configuration, 6 inches total length.*

TABLE B.1: Test Matrix

Run	Date	Injector	Flow condition	Measurement Plane	Q	$P_{t,air}$ [psia]	$T_{t,air}$ [K]	$P_{t,he}$ [psia]	$T_{t,he}$ [K]
S7	7-23-15	strut	Supersonic	far plane	1.81	115.08	293.53	183.5	295.91
S8	7-23-15	strut	Sonic	far plane	3.79	54.82	292.52	182.66	296.46
S9	7-23-15	strut	Subsonic	far plane	5.70	36.31	292.40	181.82	296.13
S10	7-23-15	strut	Subsonic	far plane	5.78	35.48	292.39	180.17	296.49
S11	7-27-15	strut	Subsonic	far plane	6.20	33.92	289.70	183.69	298.45
S12	7-27-15	strut	Subsonic	far plane	6.08	34.59	288.00	183.02	299.32
S14	7-28-15	strut	Supersonic	far plane	1.70	121.40	293.30	181.61	297.67
S15	7-28-15	strut	Sonic	far plane	3.76	54.56	293.53	180.32	299.3
S16	7-28-15	strut	Subsonic	far plane	5.51	37.89	293.40	183.70	300.00
S17	7-29-15	strut	Supersonic	far plane	1.84	116.88	277.34	182.66	297.40
S18	7-29-15	strut	Sonic	far plane	3.94	53.90	278.30	180.8	297.37
S19	7-29-15	strut	Subsonic	far plane	5.57	37.80	277.56	179.32	297.53
S20	7-29-15	strut	Subsonic	far plane	5.32	39.22	277.50	177.6	297.85
S21	8-4-15	strut	Subsonic	near plane	1.72	115.15	293.70	174.45	296.72
S22	8-4-15	strut	Sonic	near plane	3.77	64.69	292.97	214.39	296.67
S23	8-4-15	strut	Supersonic	near plane	5.93	43.00	292.56	226.01	297.15
S24	8-4-15	strut	Supersonic	near plane	1.79	115.80	295.51	183.54	297.58
S25	8-4-15	strut	Sonic	near plane	3.79	65.31	294.23	218.04	298.51
S26	8-4-15	strut	Subsonic	near plane	5.86	44.63	295.00	230.64	300.01

Table B.1: Test Matrix - cont.

Run	Date	Injector	Flow condition	Measurement Plane	Q	$P_{t,air}$ [psia]	$T_{t,air}$ [K]	$P_{t,he}$ [psia]	$T_{t,he}$ [K]
R4	4-22-15	FWI	Subsonic	far plane	3.31	46.65	274.64	130.68	305.91
R5a	5-29-15	FWI	Subsonic	far plane	4.63	31.63	283.12	126.26	307.01
R5b	5-29-15	FWI	Subsonic	near plane	4.43	31.94	282.24	121.62	308.45
R10	8-5-15	FWI	Supersonic	near plane	1.92	113.14	292.80	190.88	296.07
R11	8-5-15	FWI	Sonic	near plane	3.76	65.50	293.32	216.42	297.19
R12	8-5-15	FWI	Subsonic	near plane	5.13	44.19	293.17	199.36	297.05
R14	8-12-15	FWI	Supersonic	far plane	1.76	117.13	292.62	180.64	295.64
R15	8-12-15	FWI	Sonic	far plane	3.59	56.72	291.3	178.21	295.50
R16	8-12-15	FWI	Subsonic	far plane	5.36	37.36	291.43	175.52	295.74

TABLE B.2: *Instrumentation Uncertainties*

Pressure transducers	Range (0- X) psia	Sensitivity $[psi/mV]$	μ_c $(\%FS)$
P_{hw}	15	0.1507	0.025
$P_{t,air}$	150	1.5025	0.031
P_{he}	500	4.9817	0.009
$P_{abs,he}$	2500	25.535	0.027
$P_{d,he}$	100	1.6891	0.321
Flowmeters	Range (0- X) SLPM	Sensitivity [psi/mV]	μ_c $(\%FS)$
Helium	5	1.00217	0.188
Air	5	1.00436	0.188
Initium scanner	Range (0- X) psia	Resolution $(\%FS)$	accuracy $(\%FS)$
P_{wall}	100	0.003	0.05
Thermocouple uncertainty:		$\mu_c = +/-1°C$	

Appendix C

Data Reduction Methods

This section gives an overview of the process of taking the raw data files and reducing them to the products: contour plots, dynamic pressure ratio, mixing efficiency, total pressure recovery, and mass-averaged Mach number. The uncertainty calculations for these quantities are discussed.

C.1 Data Reduction

The tools to reduce and process the data were created using Python, an open source, object-oriented programming language. Tecplot was used to generate the planar grids for the contour plots, and Tecplot interpolated the measurements using an 8-point interpolation. Boundary conditions were assumed at the wall, where velocity, U, and helium mole fraction, χ_{he}, are zero and the pressure is atmospheric pressure. For each injector and flow condition, two axial planes were scanned, the far plane and near plane, making up the 12 test points of the test matrix. For some of the test points multiple experiments

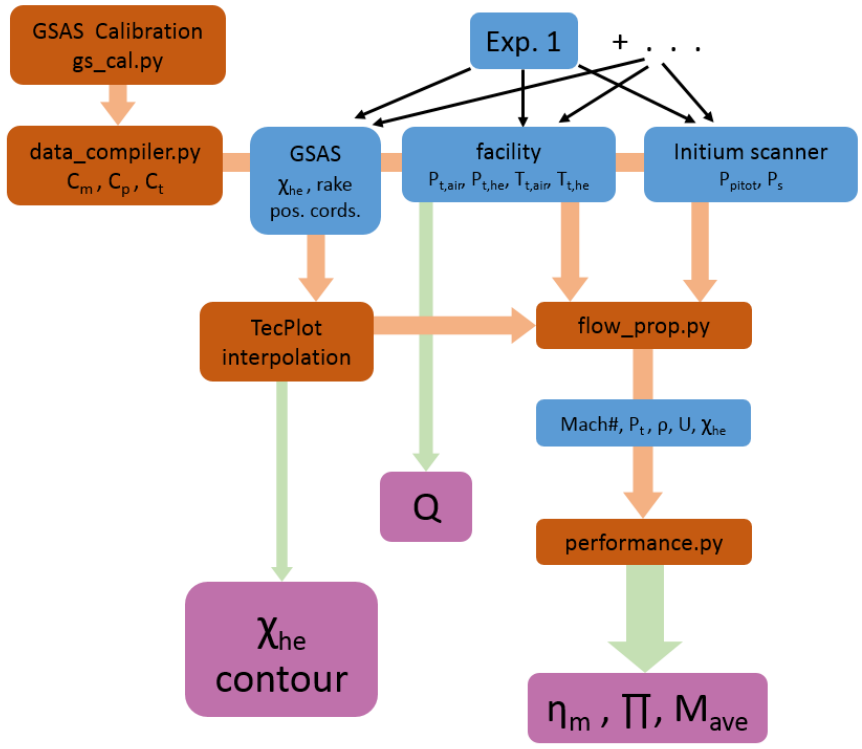

FIGURE C.1: *Flowchart of the data reduction process*

were compiled to build the output products. Figure C.1 shows a flowchart of the processing to take the raw data from each experiment and reduce it to a the usable product for examining the physics of the experiment. The python script, data_compiler.py, synchronizes the data from each source using absolute time stamps in the headers of each file, applies the GSAS calibration and calculates averages and statistics, then stacks the helium mole fraction, χ_{he}, from each experiment, and the boundary conditions, into a file for Tecplot. Tecplot interpolates this data onto a 100 x 50 point grid in y and z respectively. The interpolated data is saved to a file and read back into python by data_compiler.py. The Pitot pressure probe is 0.25 inches offset in the z-direction from the gas sampling probe, therefore, flow_prop.py first calculates the interpolated χ_{he} for each measurement point from the interpolated Tecplot data file, then the ratio of specific heats, γ, is calculated from eq. C.2, based on the gas mixture.

$$\chi_{he,cor} = \chi_{he} C_m \frac{MW_{he}}{MW_{air}} \tag{C.1}$$

$$\gamma = 0.0703\chi_{he}^3 + 0.0275\chi_{he}^2 + 0.1694\chi_{he} + 1.3994 \tag{C.2}$$

A subroutine, called bisection.py [41], then uses equations C.5 through C.9 and iterates over a specified range in Mach number, from 1.01 to 2.8. It first tries the upper and lower bound. If it finds that a solution exists within these bounds then it executes until the error is less than the iteration error, e_{it}, or the max iterations is reached. If the solution is found to be greater than the upper bound, the program stops and prints an error message.

$$\left.\begin{aligned} C_p &= \frac{P_{t,nom}}{P_t}\ |_{air} \\ C_T &= \frac{T_{tnom}}{T_t}\ |_{air} \\ C_{m,he} &= \frac{\frac{P_{t,nom}}{\sqrt{T_{t,nom}}}}{\frac{P_t}{\sqrt{T_t}}}\ |_{he} \\ C_{m,a} &= \frac{\frac{P_{t,nom}}{\sqrt{T_{t,nom}}}}{\frac{P_t}{\sqrt{T_t}}}\ |_{air} \\ C_m &= \frac{C_{m,a}}{C_{m,he}} \\ C_Q &= \left(\frac{Q_{nom}}{Q}\right)^{1/3} \end{aligned}\right\} \tag{C.3}$$

$$\left.\begin{aligned} P_{t,corr} &= C_p P_t \\ M_{corr} &= M\sqrt{C_T} \\ \chi_{corr} &= \frac{\chi_{he}}{\chi_{he} + (1-\chi_{he})C_m} \\ \frac{Y}{D}\ |_{corr} &= \frac{Y}{D} C_Q \end{aligned}\right. \tag{C.4}$$

$$\frac{P_t}{P_s} C_p = \left(1 + \frac{\gamma - 1}{2} M^2\right)^{\frac{\gamma-1}{\gamma}} \tag{C.5}$$

$$\frac{P_{pit,new}}{P_t} = \left[\frac{(\gamma+1)M^2}{(\gamma-1)M^2+2}\right]^{\frac{\gamma}{\gamma-1}} \left[\frac{\gamma+1}{2\gamma M^2-(\gamma-1)}\right]^{\frac{1}{\gamma-1}} \tag{C.6}$$

$$\frac{T_t}{T_s}C_p = 1 + \frac{\gamma-1}{2}M^2 \tag{C.7}$$

$$M_{cor} = M\sqrt{C_T} \tag{C.8}$$

$$e_{it} = \frac{P_{pit} - P_{pit,new}}{P_{pit}} \tag{C.9}$$

If the solution is less than the lower bound in Mach number, then the routine outputs that the flow is subsonic, and enacts a separate Python method called pt_subsonic. This subroutine says that if the Pitot pressure, P_{pit}, is less than or equal to the static pressure, P_s, then the Mach number equals zero, and a warning is printed that the flow could be reversed. These points are then discarded by flow_prop.py. If P_{pit} is greater than P, however, then eq. C.10 is used to calculate the properties.

$$\left.\begin{aligned} P_t &= P_{pit} \\ M &= \sqrt{C_t\left(\frac{P_t}{P_s}\right)^{\frac{\gamma}{\gamma-1}}\frac{2}{\gamma-1}} \end{aligned}\right\} \tag{C.10}$$

Lastly, flow_prop.py calculates the density and velocity by eqs. C.11 - C.14.

$$MW_{mix} = MW_{he}\chi_{he} + MW_{air}\chi_{air} \tag{C.11}$$

$$R_{mix} = \frac{R_u}{MW_{mix}} \tag{C.12}$$

$$U = M\sqrt{\gamma R_{mix}T_s} \tag{C.13}$$

$$\rho = \frac{P}{R_{mix}T_s} \tag{C.14}$$

Performance.py takes the Mach number, density, velocity, and gas concentration and

calculates the one-dimensionalized mixing characteristics: mixing efficiency, and total pressure recovery, and the mass-averaged Mach number. Equations C.15 - C.18 show the methods for calculating these values. Π is summed over a consistent number of values, N, so that it is consistent between test points, where the added points are in the free-stream where the flow is unaffected by the injection. This only works based on the assumption that the mixing plume, or affected flow area, is adequately sampled by the in-stream measurements. For each test point the mixing plume was sampled throughout the full distribution of the mixing plume, so this assumption is valid. Furthermore, the results showed agreement with theory and were consistent from test point to test point.

$$P_{ref} = P_{t,air}\rho_{air}T_{s,air} \tag{C.15}$$

$$\eta_m = \frac{\sum\left(\chi_{he,r}\ \rho U\right)_i}{\sum\left(\chi\ \rho U\right)_i} \tag{C.16}$$

$$\chi_{he,r} = \begin{cases} \chi_{he} & \chi_{he} \leq \chi_{st} \\ \chi_{st}\left(\frac{1-\chi_{he}}{1-\chi_{st}}\right) & \chi_{he} > \chi_{st} \end{cases} \tag{C.17}$$

$$\Pi = \frac{\sum\left(P_t\ \rho U\right)_i + \sum_{N-i} P_{ref}}{\sum_N\left(P_{ref}\ \rho U\right)} \tag{C.18}$$

$$M_{ave} = \frac{\sum\left(M\rho U\right)_i}{\sum\left(\rho U\right)} \tag{C.19}$$

C.2 Uncertainty Calculations

The uncertainty in the mixing characteristics is determined starting from the individual measurement uncertainty. The data reduction constitutes a complex system of equations that use many measurements to determine the final output values. In order to quantify the uncertainty on the final product from the measurement uncertainties, the

calculations were perturbed one variable at a time to determine the sensitivity of each input variable on the final outputs: η_m and Π. The uncertainty for the χ_{he} contour plots is quantified by the mean and max uncertainty.

$$\mu\eta_m = \sqrt{\left(\frac{\partial\eta_m}{\partial\rho}\mu\rho\right)^2 + \left(\frac{\partial\eta_m}{\partial\, U}\mu U\right)^2 + \left(\frac{\partial\eta_m}{\partial\chi_{he}}\mu\chi_{he}\right)^2} \tag{C.20}$$

$$\mu\Pi = \sqrt{\left(\frac{\partial\Pi}{\partial\rho}\mu\rho\right)^2 + \left(\frac{\partial\Pi}{\partial\, U}\mu U\right)^2 + \left(\frac{\partial\Pi}{\partial P_t}\mu P_t\right)^2} \tag{C.21}$$

TABLE C.1: *Sensitivity of Calculated Variables to the Output Variables*

X	$\frac{\partial\eta_m}{\partial X}$	$\frac{\partial\Pi}{\partial X}$
ρ	0.01623	0.04341
U	3E-6	0.00023
χ_{he}	1.0075	-
P_t	-	0.00034

To quantify the sensitivity of the calculated variables, M, P_t, U, ρ, and T, the sensitivity of these variables to the measured variables, P_{pit}, χ_{he}, $P_{t,air}$, $T_{t,air}$, P_s, must be made. To do this either the partial derivatives are calculated, where partial derivatives can't be calculated the inputs are perturbed to get the response in the calculated variables. From this a matrix of sensitivities, S, is built (X by x), where X are the calculated variables and x, are the measured variables. Squaring each term of S, and multiplying it by the vector of squared uncertainties for each measured variable, by eq. C.24 gives a vector, E, of the uncertainty for each calculated variable.

$$\left.\begin{aligned} S &= \left[\left(\tfrac{\partial X}{\partial x}\right)^2\right] \\ e &= \left\{\mu x^2\right\} \end{aligned}\right\} \tag{C.22}$$

The measurement uncertainty is quantified by the instrument uncertainty, μ_c, and the student-t distribution based on the degrees of freedom, $\nu = n - 1$, where n is the sample size. A 95% confidence interval was used, for P_{pit} $t_{stat,P_{pit}} = 2.365$ because the sample size was small; approximately eight samples per measurement point. The other measurements used $t_{stat} = 1.645 for \nu = \infty$.

$$\mu x = \sqrt{\mu_c^2 + (t_{stat,x}\sigma_x)^2} \tag{C.23}$$

$$E = Se = \begin{bmatrix} \mu M \\ \mu P_t \\ \mu U \\ \mu \rho \\ \mu T \end{bmatrix} \tag{C.24}$$

The uncertainty in mixing efficiency was roughly 4%. The uncertainty in total pressure recovery was very small, less than 1%; while the uncertainty in the pitot pressure measurements was higher, the sensitivity to the overall total pressure recovery was very small. The uncertainty of the mass average Mach number was not considered because this value was only used as a general indicator of the flow compressibility.

References

[1] Adler, D. A hot-wire technique for continuous measurement in unsteady concentration fields of binary gaseous mixtures. *J. Physics*, 5:163–169, 1972.

[2] Aguilera, C. and Yu, K. Effect of fin-guilded fuel injection on dual mode scramjet operation. In *50th AIAA/ASME/SAE/ASEE Joint Propulsion Conference and Exhibit*, number 2014-3945. AIAA, 2014.

[3] Ahmed, S. A. and So, R. M. Concentration distributions in a model combustor. *Experimental Fluids*, 4:107–113, 1986.

[4] Al-Ammar, K., Agrawal, A. K., Gollahalli, S. R., and Griffin, D. Application of rainbow schlieren deflectometry for concentration measurements in an axisymmetric helium jet. *Experiments in Fluids*, 1998.

[5] Ashley, J. M., Szmuk, M., Clemens, N. T., Akella, M. R., Gogineni, S., and Donbar, J. M. Closed-loop control of shock location in mach 1.8 direct connect wind tunnel. In *7th AIAA Flow Control Conference*, number 2014-2935. AIAA, 2014.

[6] Auslender, A. H. Predictions of x-51a isolator operability margins utilizing subscale pswt facility inlet-unstart data. *JANNAF CS/APS/EPSS/PSHS Joint Meeting*, 2012.

[7] Auslender, A. H. Private communications. NASA LaRC, June 2015.

[8] Bathel, B. F., Borg, S., Jones, S., Overmeyer, A., Walker, E., Goad, W., Clem, M., Schairer, E. T., and Mizukaki, T. Development of background oriented schlieren for nasa langley research center ground test facilities. In *53rd Aerospace Sciences Meeting*, number 2015-1691. AIAA, 2015.

[9] Baurle, R. A. and Gaffney, R. L. The art of extracting one-dimensional flow properties from multi-dimensional data sets. In *45th Aerospace Sciences Meeting*, number 2007-639, 2007.

[10] Baurle, R. A., Fuller, R. P., White, J. A., Chen, T. H., Gruber, M. R., and Nejad, A. S. An investigation of advanced fuel injection schemes for scramjet combustion. In *36th AIAA Aerospace Sciences Meeting*, number 1998-937, 1998.

[11] Beresh, S. J., Henfling, J. F., Erven, R. J., and Spillers, R. W. Crossplane velocimetry of a transverse supersonic jet in a transonic crossflow. In *44th AIAA Aerospace Sciences Meeting*, number 2006-906. AIAA, 2006.

[12] Billig, F. and Schetz, J. Analysis of penetration and mixing of gas jets in supersonic cross flow. In *4th International Aerospace Planes Conference*, number 92-5061. AIAA, 1992.

[13] Billig, F. S., Orth, R. C., and Lasky, M. A unified analysis of gaseous jet penetration. *AIAA J.*, 9(6):1048–1058, 1971.

[14] Blackshear, P. and Fingerson, L. Rapid-response heat flux probe for high temperature gases. *Amateur Rocket Society Journal*, 32:1709–1715, 1962.

[15] Blankson, I. M., Murthy, S. N., and Bruno, C. *Technologies for Propelled Hypersonic Flight*, chapter 9. Number TR-AVT-007-V2. RTO/NATO, 2006.

[16] Bogdanoff, D. W. Compressibility effects in turbulent shear layers. *AIAA J.*, 21 (6):926–927, 1983.

[17] Borghi, M. R., Engblom, W. A., and Georgiadis, N. J. Evaluation of mixing-limited quasi-global wind-us model for hifire 2 flowpath. In *52nd Aerospace Sciences Meeting*, number 2014-1160. AIAA, 2014.

[18] Breidenthal, R. E. Sonic eddy-a model for compressible turbulence. *AIAA J.*, 30 (1):101–104, 1992.

[19] Brown, G. and Rebollo, M. R. A small, fast-response probe to measure composition of a binary gas mixture. *AIAA J.*, 10(5):649–652, 1972.

[20] Brown, G. L. and Roshko, A. On density effects and large structure in turbulent mixing layers. *Journal of Fluid Mechanics*, 64(4):775–816, 1974.

[21] Burger, S. K., Schetz, J. A., and Ungewitter, R. Effects of injectant molecular weight on transverse injection mixing processes in supersonic flow. In *16th AIAA/CIRA International Space Planes and Hypersonic Systems and Technologies Conference*, number 2009-7315. AIAA, 2009.

[22] Bushnell, D. M. *Advanced Hypersonic Test Facilities*, chapter Hypersonic Ground Test Requirements, pages 1 – 15. AIAA, 2002.

[23] Center, N. D. F. R. X-43a hypersonic experimental vehicle - artist concept in flight. Technical Report ED99-45243-01, 1999. URL http://www.dfrc.nasa.gov/Gallery/Photo/X-43A/Medium/ED99-45243-01.jpg.

[24] Center, N. L. R. Scramjet engine.

[25] Chen, T. H., Creese, A., Dasgupta, S., Fuller, R. P., and Wu, P. K. Combustion and mixing studies in compressible flows. Technical Report WL-TR-96-2129, Aeropropulsion and Power Directorate Wright Laboratory, 1996.

[26] Clemens, N. T. and Mungal, M. G. Two and three-dimensional effects in the supersonic mixing layer. *AIAA J.*, 30(4):973–981, 1992.

[27] Clemens, N. T. and Mungal, M. G. Large-scale structure and entrainment in the supersonic mixing layer. *J. Fluid Mech.*, 1995.

[28] Clemens, N. T. and Paul, P. H. Scalar measurements in compressible axisymmetric mixing layers. In *31st Aerospace Sciences Meeting*, 1993.

[29] Cocks, P., Dawes, W. N., and Cant, R. S. The influence of turbulence-chemistry interaction modelling for supersonic combustion. In *49th AIAA Aerospace Sciences Meeting*, number 2011-306. AIAA, 2011.

[30] Crafton, J., Fonov, S., Hsu, K.-Y., Carter, C. D., and Gruber, M. R. Optical measurements of pressure and shear on a strut in supersonic flow. In *45th Joint Propulsion Conf.*, number 2009-5033. AIAA, 2009.

[31] Danehy, P. M., Palma, P. C., McIntyre, T. J., and Houwing, A. F. Comparison of theoretical laser-induced fluorescence images with measurements performed in a hypersonic shock tunnel. In *19th AIAA Advanced Measurement and Ground Testing Technology Conference*, number 96-2236, 1996.

[32] DeLoach, R. The modern design of experiments for configuration aerodynamics: A case study. In *44th Aerospace Sciences Meeting*, number 2006-923. AIAA, 2006.

[33] DePiro, M. J. and Quinlan, J. R. Supersonic core flow fuel penetration for strut tip fuel injectors.

[34] Devillers, J. F. and Diep, G. B. Hot-wire measurements of gas mixture concentrations in a supersonic flow. *DISA Info*, 14:29–26, 1973.

[35] Dimotakis, P. and Leonard, A. Chemical reactions in turbulent mixing flows. Afosr technical report, California Institute of Technology, 1994.

[36] Diskin, G. and Northam, G. Effects of scale on supersonic combustor performance. Number 87-2164. AIAA, 1987.

[37] Doerner, S. and Cutler, A. D. Effects of jet swirl on mixing of a light gas jet in a supersonic airstream. Technical Report CR-1999-209842, NASA Langley Research Center, 1999.

[38] Donohue, J. M. Dual-mode scramjet flameholding operability measurements. *J. Prop. and P.*, 30(3), 2014.

[39] Doster, J. C., King, P. I., Gruber, M. R., and Maple, R. C. Pylon fuel injector design for a scramjet combustor. In *43rd Joint Propulsion Conf.*, number 2007-5404. AIAA, 2007.

[40] Doster, J. C., King, P. I., Gruber, M. R., Carter, C. D., Ryan, M. D., and Hsu, K.-Y. In-stream hypermixer fuefuel pylons in supersonic flow. *J. Prop. and P.*, 25 (4), 2009.

[41] Drozda, T. Technical conversations. September 2015.

[42] Elliott, G. S. and Samimy, M. Compressibility effects in free shear layers. *Phys. Fluids A*, 2(7):1231–1240, 1990.

[43] Evans, J. S. and Schexnayder, C. J. Influence of chemical kinetics and unmixedness on burning in supersonic hydrogen flames. *AIAA*, 18(2), 1976.

[44] Fotia, M. L. Mechanics of combustion mode transition in a direct-connect ramjet-scramjet experiment. *J. of Prop. and P.*, 2013. doi: 10.2514/1.B35171.

[45] Fotia, M. L. and Driscoll, J. F. Isolator-combustor interactions in a direct-connect ramjet-scramjet experiment. *J. Prop. and P.*, 28(1), 2012.

[46] Freehorn, A. B., King, P. I., and R., G. M. Swept-leading-edge pylon effects on a scramjet pylon-cavity flameholder flowfield. *J. Prop. and P.*, 2009.

[47] Geerts, J. S. and Yu, K. Systematic application of background oriented schlieren for shock-boundary layer interaction study. In *52nd Aerospace Sciences Meeting*, number 2014-0987. AIAA, 2014.

[48] Gruber, M. R., Nejad, A. S., Chen, T. H., and Dutton, J. C. Mixing and penetration studies of sonic jets in a mach 2 freestream. *J. Prop. and P.*, 11(2), 1995.

[49] Gruber, M. R., Nejad, A. S., Chen, T. H., and Dutton, J. C. Large structure velocity measurements in compressible transverse injection flowfields. *Exp. in Fluids*, 1997.

[50] Gruber, M. R., Nejad, A. S., and Goss, L. P. Surface pressure measurements in supersonic transverse injection flowfields. *AIAAJournal*, 1997.

[51] Gruber, M. R., Donbar, J. M., Carter, C. D., and Hsu, K.-Y. Mixing and combustion studies using cavity-based flameholders in a supersonic flow. *J. Prop. and P.*, 20(5), 2004.

[52] Gruber, M. R., Carter, C. D., Haubelt, L. C., King, P. I., and Hsu, K.-Y. Experimental studies of pylon-aided fuel injection into a supersonic crossflow. *J. Prop. and P.*, 24(3), 2008.

[53] Hall, J. L. *An Experimental Investigation of Structure, Mixing, and Combustion in Compressible Turbulent Shear Layers.* PhD thesis, California Institute of Technology, 1991.

[54] Heiser, W. H. and Pratt, D. T. *Hypersonic Air Breathing Propulsion.* AIAA Education Series. AIAA, Washington, D.C., 1993.

[55] Hollo, S. D., Jr., H. R., and McDaniel, J. C. Injectant mole fraction measurements of transverse injection in constant area supersonic ducts. In *21st Fluid Dynamics Conf.*, number 90-1632. AIAA, June 1990.

[56] Hollo, S. D., McDaniel, J. C., and Jr., H. R. Characterization of supersonic mixing in a nonreacting mach 2 combustor. In *30th Aerospace Sciences Meeting*, number 92-0093. AIAA, 1992.

[57] Hsu, K.-Y., Carter, C. D., Gruber, M., and Tam, C. J. Mixing study of strut injectors in supersonic flows. In *45th Joint Propulsion Conf.*, pages 2–5. AIAA, 2009.

[58] Hsu, K.-Y., Carter, C. D., Gruber, M., and Barhorst, T. S. Experimental study of cavity-strut combustion in supersonic flow. *J. Prop. and P.*, 26(6), 2010.

[59] Hutchins, K. E., Akella, M. R., Clemens, N. T., Donbar, J. M., and Gogineni, S. Experimental identification of transient dynamcis for supersonic inlet unstart. *J. Prop. and P.*, 2014.

[60] Huwaldt, J. A. and Steinhorst, S. Plot digitizer, April 2014.

[61] Ikawa, H. and Kubota, T. Investigation of supersonic turbulent mixing layer with zero pressure gradient. *AIAA J.*, 13(5):566–572, 1975.

[62] Island, T. C. *Quantitative Scalar Measurements and Mixing Enhancemnet in Compressible Shear Layers.* PhD thesis, Stanford University, 1997.

[63] Jones, B. G. and Wilson, R. J. Gas concentration measurements with a temperature compensated aspirating probe. In *Proc. of the Fifth Biannual Symp. on Turbulence.* Princeton Science Press, 1979.

[64] Jorgensen, F. E. *How to Measure Tubulence with Hot-Wire Anemometers - A Practical Guide*. Dantec Dynamics, 2002. p. 46.

[65] Kundu, P. K. and Cohen, I. M. *Fluid Mechanics*, chapter 12. Instability, pages 515–516. Elsevier Inc., 2008.

[66] Le, D. B., Goyne, C. P., Krauss, R. H., and McDaniel, J. C. Experimental study of a dual-mode scramjet isolator. In *43rd Aerospace Sciences Meeting*, number 2005-23. AIAA, 2005.

[67] LiHong, C., Ran, L., HongBin, G., and Xinyu, C. Analyses of supersonic combustion by gas sampling. In *13th AIAA/CIRA International Space Planes and Hypersonic Systems and Technologies Conference*, number 2005-3317. AIAA, 2005.

[68] Mao, M., Riggins, D., and McClinton, C. R. Numerical simulation of transverse fuel injection. Technical Report NASA Contractor Report 1089, NASA, 1990.

[69] Mathur, T., Lin, K.-C., Kennedy, P., Gruber, M., Donbar, J., Jackson, T., and Billig, F. Liquid jp-7 combustion in a scramjet combustor. In *36th AIAA Joint Propulsion Conference*, number 2000-3581. AIAA, 2000.

[70] McClinton, C. R. The effect of injection angle on the interaction between sonic secondary jets and a supersonic free stream. Technical Report TN D-6669, NASA, 1972.

[71] McClinton, C. R. Effect of ratio of wall boundary layer thickness to jet diameter on mixing of a normal hydrogen jet in a supersonic stream. Technical Report TM X-3030, NASA, 1974.

[72] McClinton, C. R. Evaluation of scramjet combustor performance using cold non-reactive mixing tests. In *14th Aerospace Sciences Meeting*. AIAA, 1976.

[73] McClinton, C. R. X-43 scramjet power breaks the hypersonic barrier dryden lectureship in research for 2006. In *44th AIAA Aerospace Sciences Meeting and Exhibit*, number 2006-1. AIAA, 2006.

[74] McClinton, C. R., Ferlemann, S. M., Rock, K. E., and Ferlemann, P. G. The role of formal experiment design in hypersonic flight system technology development. In *40th AIAA Aerospace Sciences Meeting*, number 2002-0543. AIAA, 2002.

[75] McDaniel, J. C. Transverse jet mixing in presence of back-pressure induced shock train. Technical report, University of Virginia, 1992.

[76] McDaniel, J. C. and Graves, J. Laser-induced-flourescence visualization of transverse gaseous injection in a non-reacting supersonic combustor. *J. Prop. and P.*, 4(6):591–597, 1988.

[77] Metzler, A. J. and Mertz, T. W. Large scale supersonic combustor testing at conditions simulating mach 8 flight. Technical Report NASA TM X-52785, NASA Lewis Research Center, 1970.

[78] Metzler, A. J. and Mertz, T. W. Preliminary results of large supersonic burning combustor testing. *J. Aircraft*, 9(1):23–30, 1972.

[79] Miller, C. Aerothermodynamic flight simulation capabilities for aerospace vehicles. In *20th AIAA Advanced Measurement and Ground Testing Technology Conf.*, number 1998-2600. AIAA, 1998.

[80] Miyazato, Y., Irie, M., Yamamoto, H., and Matsuo, K. Quantitative flow visualization of correctly expanded supersonic jets by rainbow schlieren deflectometry. In *48th Aerospace Sciences Meeting*, number 2010-1218. AIAA, 2010.

[81] Mungal, M., Dimotakis, P., and Hermanson, J. C. Reynolds number effects on mixing and combustion in a reacting shearlayer. *AIAA J*, 23(9), 1985.

[82] Ng, W., Kwok, F., and Ninnemann, T. A concentration probe for the study of mixing in supersonic shear flows. Number 89-2459. AIAA, 1989.

[83] Northam, G. and Anderson, G. Survey of supersonic combustion ramjet research at langley. *AIAA*, (86-37079), 1986.

[84] Papamoschou, D. and Hubbard, D. G. Viual observations of supersonic transverse jets. *Experiments in Fluids*, 14:468–476, 1993.

[85] Papamoschou, D. and Roshko, A. The compressible turbulent shear layer: An experimental study. *Journal of Fluid Mechanics*, 197(1):453–477, 1988.

[86] Parker, P. Technical conversations. March 2015.

[87] Pitts, W. M. Species concentration measurements. In *Solid Propellant Gas Generator Workshop*, number NISTIR 5766. NIST, 1995.

[88] Pitts, W. M., Mulholland, G., Breuel, B. D., Johnsson, E., Chung, S., and H., H. D. *Fire Suppresion System Performance of Alternative Agents in Aircraft Engine and Dry Bay Laboratory Simulations*, chapter Real-time Suppressant Concentration Measurement, pages 324–341. NIST, 1995.

[89] Povinelli, L. A. An aerodynamic study of scramjet fuel injectors. Technical report, NASA Lewis Research Center, 1974.

[90] Rockwell, R. D., Goyne, C. P., Rice, B. E., Chelliah, H., McDaniel, J. C., Edwards, J. R., Cantu, L., Gallo, E., Cutler, A. D., and Danehy, P. M. Development of

a premixed combustion capability for dual-mode scramjet experiments. In *53rd Aerospace Sciences Meeting*, number 2015-0353. AIAA, 2015.

[91] Rogers, R. C. Mixing of hydrogen injected from multiple injectors normal to a supersonic airstream. Technical Report NASA TN D-6471, NASA Langley Research Center, 1971.

[92] Santiago, J. G. and Dutton, J. C. Crossflow vortices of a jet injected into a supersonic crossflow. *AIAA Journal*, 1997.

[93] Schetz, J. A. and Billig, F. S. Penetration of gaseous jets injected into a supersonic stream. *J. Spacecraft*, 3(11):1658–1665, 1966.

[94] Shirinzadeh, B., Balla, R. J., and Hillard, M. E. Rayleigh scattering measurements in supersonic facilities. *AIAA J.*, (2187), 1996.

[95] Sullins, G. A. Demonstration of mode transition in a scramjet combustor. *J. Prop. and P.*, 9(4), 1993.

[96] Sunami, T. and Wendt, M., M. Nishioka. Supersonic mixing and combustion control using streamwise vorticity. In *34thJoint Propulsion Conf.*, number 1998-3271. AIAA, 1998.

[97] Sunami, T., Murakami, A., Kudo, K., and Kodera, M., M.and Nishioka. Mixing and combustion control strategies for efficient scramjet operation in wide range of flight mach numebers. In *11th International Space Planes adn Hypersonic Systems and Technology*, number 2002-5116. AIAA, 2002.

[98] Tam, C. J., Hsu, K.-Y., Gruber, M. R., and Raffoul, C. N. Aerodynamic performance of an injector strut for a round scramjet combustor. In *43rd AIAA/ASME/SAE/ASEE Joint Propulsion Conference*, number 2007-5403. AIAA, 2007.

[99] Tam, C. J., Hsu, K.-Y., Gruber, M. R., and Raffoul, C. N. Fuel/air mixing characteristics of strut injectors for scramjet combustor applications. In *26th AIAA Applied Aero. Conf.*, number AIAA 2008-6925, 2008.

[100] Tomioka, S., Izumikawa, M., Sakuranaka, N., Shibata, H., Yamasaki, H., Kobayashi, T., , and Matsuo, A. Mixing control by wall flush-mount injectors in dual-mode combustor. In *46th AIAA/ASME/SAE/ASEE Joint Propulsion Conference and Exhibit*, number 2010-6959. AIAA, 2010.

[101] Torrence, M. Effect of injectant molecular weight on mixing of a normal jet in a mach 4 airstream. Technical Report NASA TN D-6061, NASA Langley Research Center, 1971.

[102] Waltrup, P. J. and Billig, F. S. Structure of shock waves in cylindrical ducts. *AIAA J.*, 11(10), 1973.

[103] Wantanabe, S. and Mungal, M. G. Velocity field measurements of mixing enhanced compressible shear layers. In *37th AIAA Aerospace Sciences Meeting*, number 99-0088, 1999.

[104] Way, J. and Libby, P. A. Hot-wire probes for measuring velocity and concentration in helium-air mxtures. *AIAA J.*, 8(5), 1970.